Doctoral Dissertations   Graduate School

8-2013

The study of nuclear structure of neutron-rich 81Ge and its contribution in the r-process via the neutron transfer reaction 80Ge(d,p)

Sunghoon Ahn
University of Tennessee - Knoxville, sahn1@utk.edu

To the Graduate Council:

I am submitting herewith a dissertation written by Sunghoon Ahn entitled "The study of nuclear structure of neutron-rich 81Ge and its contribution in the r-process via the neutron transfer reaction 80Ge(d,p)." I have examined the final electronic copy of this dissertation for form and content and recommend that it be accepted in partial fulfillment of the requirements for the degree of Doctor of Philosophy, with a major in Physics.

Kate L. Jones, Major Professor

We have read this dissertation and recommend its acceptance:

Daniel W. Bardayan, Jason P. Hayward, Robert Grzywacz, Thomas Papenbrock

Accepted for the Council:

Carolyn R. Hodges

Vice Provost and Dean of the Graduate School

(Original signatures are on file with official student records.)

The study of nuclear structure of neutron-rich 81Ge and its contribution in the r-process via the neutron transfer reaction 80Ge(d,p)

A Dissertation

Presented for the

Doctor of Philosophy

Degree

The University of Tennessee, Knoxville

Sunghoon Ahn

August 2013

Dedicated in memory of my brother, Yonghoon Ahn

Acknowledgments

When I left a company and came back to study Physics five years ago, I prayed that I could feel the joy of understanding the nature which I had learned in a undergraduate physics study club, $\hbar$-*action*. Although it was not easy to enjoy my study during the Ph.D. course, I was mostly happy with looking for answers to untangle my thesis experimental data. During the period, I owed many thanks to all of influences that gave me opportunities and lessons to enjoy the Ph.D. study.

First and foremost, I would like to give special appreciations to my two advisors, Kate Jones and Dan Bardayan, for excellent guidances, invaluable encouragements and endless supports. I am sure that I could not reach this professional level of the study without their strong insights and leadership.

I would also thank other committee members: Drs. Robert Grzywacz, Thomas Papenbrock and Jason Hayward. I will do my best in the future so you become happy that you have agreed me to get the Ph.D. degree.

Insik Hahn and Kyungyuk Chae also deserve my special thanks for leading me to this field with a great encouragement. I'd like to thank Michael Smith as well for giving me a chance to join the nuclear astrophysics group at the Oak Ridge National Laboratory.

I am sincerely thankful to all members in the group for teaching me how to work correctly and motivate me to break through many obstacles: Milan Matoš for mentoring the ASICs implementation project as well as for frequent visits to my office, Brett Manning for being my best friend and for sharing many secretes, Steve Pain

"Everything should be made as simple as possible, but not simpler."

- Albert Einstein

Abstract

The study of low-lying levels of nuclei near closed shells not only elucidates the evolution of nuclear shell structure far from stability, but also affects estimates of heavy element nucleosynthesis in supernova explosions. Especially, the properties of the low-lying levels in ^{81}Ge[Germanium 81] are important because the sensitivity study of the r-process pointed out that the properties of the nucleus can affect the final abundance pattern. Also, the spins and parities measurements of the states are essential to understand the shape coexistence in odd-mass $N = 49$ isotones.

This work describes the study of the odd-mass $N = 49$ nucleus, ^{81}Ge in the region of neutron magic number $N = 50$ using an inverse kinematics (d,p) transfer reaction. The $d(^{80}$Ge[Germanium 80]$,p)^{81}$Ge neutron transfer reaction was measured by bombarding a 174 μg[microgram]/cm^2[centimetersquared] (CD$_2$)$_n$[deuterated polyethylene] target with a 310 MeV beam of radioactive ^{80}Ge at the Holifield Radioactive Ion Beam Facility (HRIBF) at Oak Ridge National Laboratory (ORNL). The new ORNL DAQ ASICs system was commissioned for a first implementation of the development in the experiment.

The excitation energies of low-lying levels were measured. From analysis of the observed angular distributions, the spins and the parities were determined, and spectroscopic factors were extracted for the first time. Neutron capture cross sections on ^{80}Ge have been calculated in a direct-semidirect model using extracted spectroscopic factors. Furthermore, two intruder states were confirmed and their properties were compared with other odd-mass $N = 49$ isotones.

Table of Contents

List of Tables

List of Figures

Chapter 1

Introduction

1.1 Origin of Elements in the Universe

Nuclear Astrophysics is concerned with understanding the properties of nuclei that help explain both the formation of elements in the universe and the evolution of stellar bodies and cosmic explosions. One of the most important questions in nuclear astrophysics is "How and where were all of the elements created in the universe?" In order to answer the question, astronomers and astrophysicists have measured abundance distributions of the elements (Figure 1.1) using meteoritic, terrestrial, and astronomical sources of data.

While abundance peaks in the plot could be qualitatively explained, the fine details are still not known with certainty [21]. After Eddington's hypothesis for the energy production in a star in 1920 [22], it was generally thought that, with the exception of trace amounts of Li and other light nuclei, all of the elements heavier than helium in the Universe were created by nuclear reactions and the observed abundance pattern of elements offers one of the most powerful clues to the history of nucleosynthesis processes occurring in the interior of stars [23]. All stellar processes are related to the balance between the gravitational force tending to collapse the star and the thermal pressure produced by the various nuclear reaction processes. A mass of the star
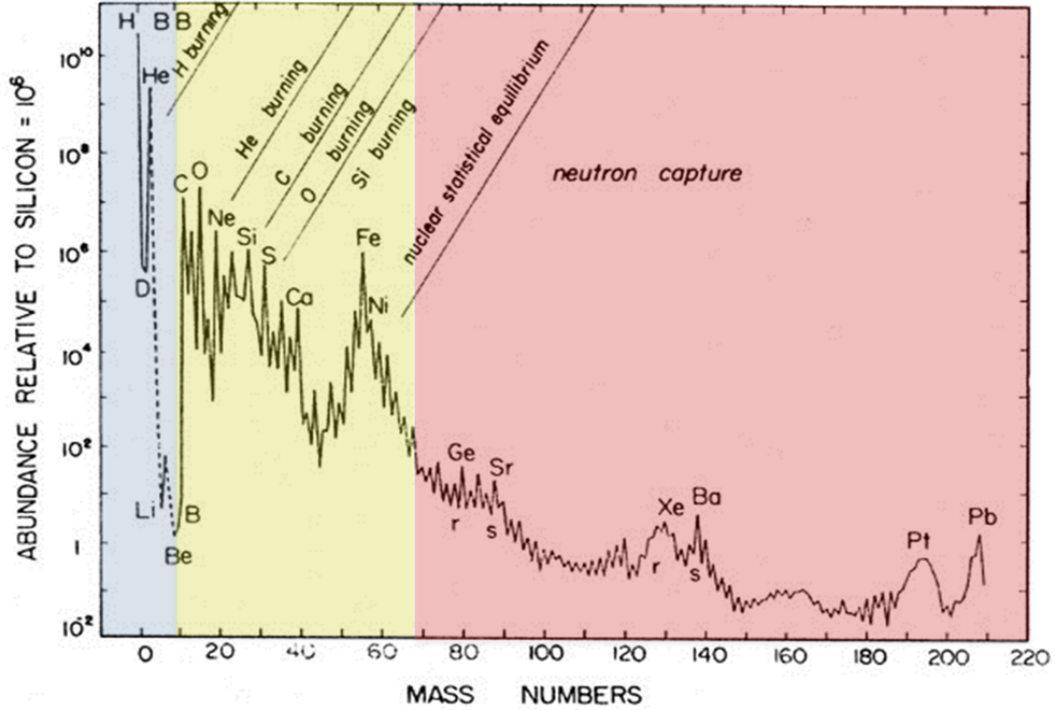
Figure 1.1: Solar system isotopic and elemental abundances, normalized to 10^6 ^{28}Si atoms, adapted from Reference [6].

mainly determines its evolution through all stages in its life; that is, the properties of the star such as temperature, luminosity, size and density can be predicted from knowing its mass.

The evolution of a massive star (M $\gtrsim$ 8M$_\odot$) has been studied for several decades but is still not well understood. The difficulties come, in part, from the incomplete nature of the observational sample. The current standard model includes collapse of the iron-core accompanied by hydrodynamic bounce at nuclear density and various magneto-hydrodynamic phenomena [21, 23]. This stellar explosion is called a core-collapse supernova, and brief description of the model follows.

It is believed that a new star is born when hydrogen burning begins in the core, including a set of proton induced reactions ultimately resulting in the fusion of 4 protons into a α. This is the primary energy source for first generation stars. Over the next $\lesssim 10^7$ years (depending on its mass) of burning, the star builds up the

ashes of the hydrogen burning processes: helium. As hydrogen burning exhausts its limited fuel, the fusion energy production rate gradually decreases, hence it can not prevent the gravitational contraction. Then, the star shrinks slowly and its density and temperature increase as the gravitational energy is converted into internal energy, resulting in hydrogen fusion resuming in the hydrogen shell surrounding the helium core. This shell gradually expands as the hydrogen in the shell burns and the core becomes more massive and dense due to the continuous gravitational contraction. The increasing temperature in the core causes an increase in thermal pressure, hence the outer regions of the star expand by a factor of 50 times its radius [21]. When the core temperature becomes high enough ($T_9 > 0.1$ where where $T_9 = 10^9$ K) to ignite the helium, the helium burning begins with reactions creating ^{12}C in what is commonly called the triple-α process occurring with three helium (^{4}He) particles involved. Immediately after the helium burning, the carbon-, neon-, and oxygen-burning phases come and they are followed by silicon burning. From the silicon burning, heavier elements such as iron or nickel are built up in the core of the star.

As more silicon nuclei are burned in the shell surrounding the iron core, both the mass of the iron core and its temperature increases until the mass slightly exceeds a limit that the star can exist in a stable state of balance between the gravitational pressure and relativistic electron pressure [21]. This limit is called the Chandrasekhar limit. As the core exceeds the limit, it can no longer support itself against gravity and it begins to collapse. Then, photodisintegration of iron nuclei and electron capture occur, removing electrons from the gas, creating neutrons and consuming energy. Both effects absorb energy from the core and speed up the collapse, and large amounts of energy are lost from the star by escaping neutrinos. The timescale of the collapse of the iron core is on the order of a second. It is interesting to note that such massive stars live $\sim 10^7$ years and then die very quickly (~ 1 second).

The collapse of the inner core continues until the density of the inner core reaches roughly the nuclear matter density. As this density is reached, since nuclear matter is nearly incompressible, the collapse is halted quickly and the inner core material
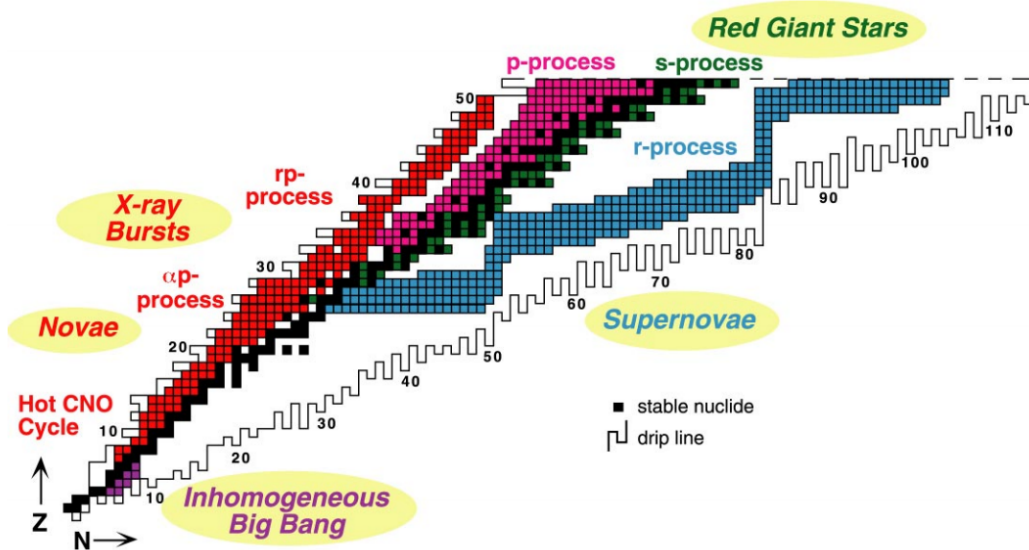
Figure 1.2: Nuclear chart including nucleosynthesis processes. Each color code represents nuclei produced by the process in the representative astrophysical environment. The direction of each process is from bottom-left to top-right. Figure taken from Reference [7].

"bounces" like a very stiff spring, reflecting a compression wave outwards through the in-falling matter of the outer core. The inner regions oscillate a few times after the bounce, but the oscillations rapidly damp out. As a final stage, the supernova evolves leaving a neutron star or a black hole depending on the mass of the star or the remnant of the explosion.

In order to explain the observed abundance curve of the elements heavier than iron, neutron capture nucleosynthesis was suggested by Burbidge, Burbidge, Fowler, and Hoyle (B^{2}FH) in 1957 [23] and independently by Cameron [24]. The synthesis proceeds in steps of 1 mass unit by (n,γ) reactions and occurs either at a slow rate (s-process) or at a rapid rate (r-process):

$$(Z, A) + n \rightarrow (Z, A + 1) + \gamma.$$
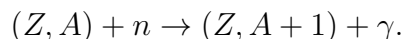
The r-process is believed to occur in an explosive environment, such as supernovae or neutron star mergers, because of the rapid time scale ($\sim 10^{-3}$ s) required for the (n,γ) reactions. Because the neutron-capture rates are fast, they can produce nuclei further away from stable nuclei. Figure 1.2 shows nucleosynthesis processes on the nuclear chart along with stable nuclides and the particle driplines.

As the neutron number increases during the process, the neutron binding energy approaches zero and (n,γ) reactions are balanced by the rate of the photodisintegration process (γ,n). At this point, the flow must wait for the nucleus to β-decay and if the lifetime is long it is called a "waiting point". The β-decay occurs to increase the nuclear charge by one unit. Subsequent neutron captures and β-decays produce heavier and heavier nuclei with increasing charge as shown in Figure 1.2. The r-process is thought to be the source of roughly half of the elements heavier than iron.

As explained above, the reaction rates of the neutron capture for each steps plays an important role to reproduce a correct r-process abundance pattern. In most nuclei near stability, neutron capture proceeds through a number of closely spaced states (more than 10 states per MeV) just above the neutron threshold energy of the compound nucleus, that is by resonant capture. For such nuclei, statistical models such as Hauser-Feshbach [25] can be used to estimate the neutron capture cross sections averaged over the resonances. The capture can also take place in a direct process to a discrete bound state with a small contribution compared to the resonant capture. However, for neutron-rich nuclei around closed-shells, the level density becomes too low to apply statistical models and contributions from the direct or semidirect process may dominate the cross sections [2, 26]. The semidirect contribution includes the effect of the giant dipole resonance (GDR). The direct radiative capture rates on these nuclei depend sensitively on the properties of low-lying states such as excitation energies, spins, parities, electromagnetic transition probabilities, and spectroscopic factors [27]. The spectroscopic factor is one of
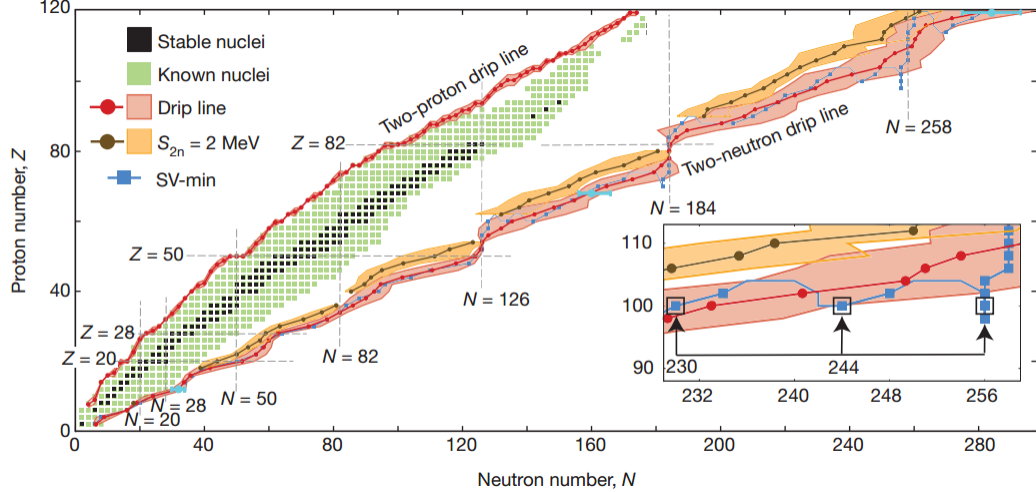
Figure 1.3: Nuclear even-even landscape with neutron number on x-axis and proton number on y-axis. Nuclei between the two-neutron drip line and two-proton drip line are expected to be bound. There are still many unknown nuclei to study. Figure taken from Reference [8].

parameters representing single particle strength and will be explained in Section 2.3.2. The direct-semidirect (DSD) capture cross sections will be discussed in Section 2.4.

The shell structure of nuclei far from stability is directly imprinted on the final r-process abundance pattern [28], and modifications in the shell structure for exotic nuclei, outside which laboratory experiments can currently reach, have been shown to have profound effects on nucleosynthesis simulations [29]. For instance, simulations using mass models for exotic nuclei with a quenched nuclear shell structure do not show large dips in the abundance pattern produced by simulations assuming a pronounced shell structure [30]. Since it will never be possible to study all nuclei involved in the r-process, it is critical to benchmark nuclear structure models, especially in the vicinity of neutron closed shells where the abundance pattern peaks and extreme sensitivity exists.

1.2 Level Structure of Neutron-rich Nuclei

An important aim of nuclear physics is to understand the properties of atomic nuclei and their interactions. From studies over the last century, it is known that nuclei consist of positively charged protons and uncharged neutrons and are bound together by the strong force [16]. Many nuclear experiments and theoretical approaches about the nature of nuclei have been performed to understand the strong force. Although almost 3000 nuclei near the stable nuclei have been studied for decades, there is still an open problem to find a general model that is detailed enough to encompass all aspects of the atomic nucleus. Furthermore, properties of more than 4000 nuclei far away from stability remain unmeasured as shown in Figure 1.3 [8, 31].

Investigations on short-lived isotopes recently became possible because of advances in producing beams of very rare ions in sufficient intensities. The availability of radioactive ion beams has allowed physicists to probe nuclei ever closer to the extremes of nuclear existence. But to use these new beams effectively, novel approaches for measurements have to be introduced, and traditional techniques, developed for light-mass beams on heavy targets, must be adapted to accommodate the unique challenges of measuring with heavy radioactive beams on light-mass targets. For example, measurements in inverse kinematics of (d,p) neutron transfer reaction is more challenging than the one in normal kinematics due to the large variance of the proton energy in the laboratory angle.

Studies of the energy level structure of exotic nuclei have been especially important in clarifying complicated properties of the nucleus. While the spherical nuclear shell model, developed by Mayer, Haxel, Jensen, and Suess [32, 33] produced the correct spins and parities of the ground states of nearly all stable nuclei, many observed low-lying excited states such as the $\frac{5}{2}^-$ state of ^{17}O, could not be reproduced by the model [16]. For single-hole (N_{magic}-1 or Z_{magic}-1) nucleon systems, shell gaps have been observed to be reduced resulting in the excitation of levels across the closed-shell,

called intruder states, to come lower in excitation energy and intrude into the low-lying levels of the single-hole spherical symmetric structure [34]. In such cases, local microscopic considerations, such as a pairing energy between two identical nucleons, the proton-neutron interaction or a non-spherical shape of nucleus, must be included as residual interactions into the simple Hamiltonian. Details of the nuclear shell model and the residual interactions will be discussed in Section 2.1.

Observations of the intruder states for odd-mass nuclei and even-even nuclei from the nuclear shell model could be explained as coming from properties of deformed excited states with the spherical ground state. (i.e. the shape coexistence [34, 35, 36].) The doubly closed shell nucleus ^{16}O, for example, has a $J^\pi = 0^+$ first excited state. By including the deformation of the excited state with two particle-two hole (2p-2h) and 4p-4h configurations in the ^{16}O observation can successfully be explained [37]. This theoretical approach starts from the Nilsson model with pairing correlations as the residual interactions.

The observation of low-lying intruder states, coexisting with other low-lying spherical states, has been also studied by many different theoretical models [34, 35, 36, 38, 39, 40]. Among the different approaches, the unified model calculation by Heyde *et al.* [34] (for odd-mass In isotopes) and Meyer *et al.* [40] (for ^{83}Se), considering residual interactions between the 1p-2h configurations as well as between 1p-2h and 1h configurations, can reproduce measured energies of the excited states. These calculations showed that the pairing correlation energy creating this 1p-2h configuration across the closed shell effectively reduced the excitation energies of the intruder states. While Heyde *et al.* [34] discussed the unified model in detail, a brief description of the unified model is written in Section 2.1.

Observables of shape coexistence such as excitation energies, spins, parities and lifetimes can be measured by experiments and compared with calculations from theory. This comparison with theory, however, is very difficult due to the paucity of experimental data for the thousands of nuclei away from stability, particularly on the neutron-rich side. Hence, the low-lying intruder states of exotic nuclei, particularly

near traditional closed shells, serve as benchmarks for shape coexistence studies. An investigation of the low-lying states of the odd-mass $N = 49$ nucleus ^{81}Ge is one of these benchmarks in determining what modifications are necessary to describe exotic nuclei far from stability.

1.3 Motivation of the ^{81}Ge Study

The only previous studies of the low-lying levels in ^{81}Ge inferred level properties from the observations of γ rays following the β decay of ^{81}Ga and the β-delayed neutron decay of ^{82}Ga [9]. Precise level energies for low-lying ^{81}Ge levels were obtained, but spins could only be estimated based on secondary arguments. A surprise was that the evidence pointed to a low-lying isomeric state with $J^\pi = \frac{1}{2}^+$ which was in contradiction to the $\frac{1}{2}^-$ spin found for the isomer in the other odd-mass $N = 49$ isotones [3, 19, 20, 41]. Clearly, determining the spins of these low-lying ^{81}Ge levels is important to understanding shell structure near $N = 50$.

This nucleus is also important for the study of the final r-process abundances. At late-times of the r-process, the temperature drops and $(n, \gamma) - (\gamma, n)$ equilibrium is broken. In this environment, the individual neutron capture rates can affect the final r-process abundances. This is mostly seen near neutron closed shells where the abundances are large, and increased capture rates act as a sink of free neutrons. Increasing certain neutron capture rates in nucleosynthesis calculations can result in altering the final estimated abundances of hundreds of nuclei throughout the entire mass range [42, 43]. In sensitivity studies, it was found that there were only certain candidates of nuclei (all around neutron closed shells), for which neutron capture could produce such an effect [10]. Fig. 1.5 shows the nuclear chart around $A \sim 80$ region colored by strength of influence in the final abundance pattern. As seen in this figure, ^{80}Ge was found to be one of these important nuclei. Because of the uncertain spin assignments of these low-lying ^{81}Ge levels and the lack of spectroscopic factor
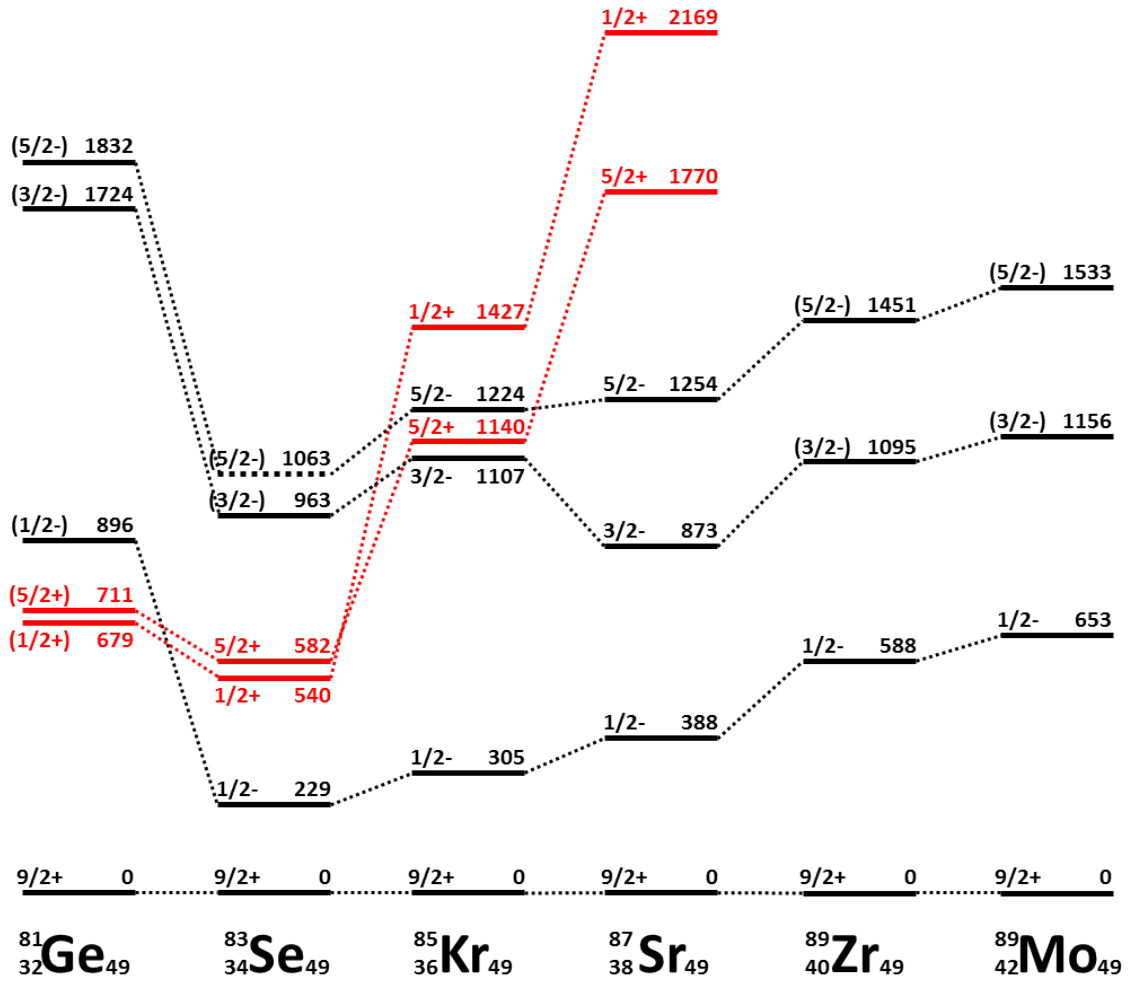
Figure 1.4: Odd-mass $N = 49$ level systematics, adopted from Reference [9]. The spins shown for ^{81}Ge are based on systematics and have not been directly measured. The red-colored levels are $\frac{1}{2}^+$ and $\frac{5}{2}^+$ intruder states.
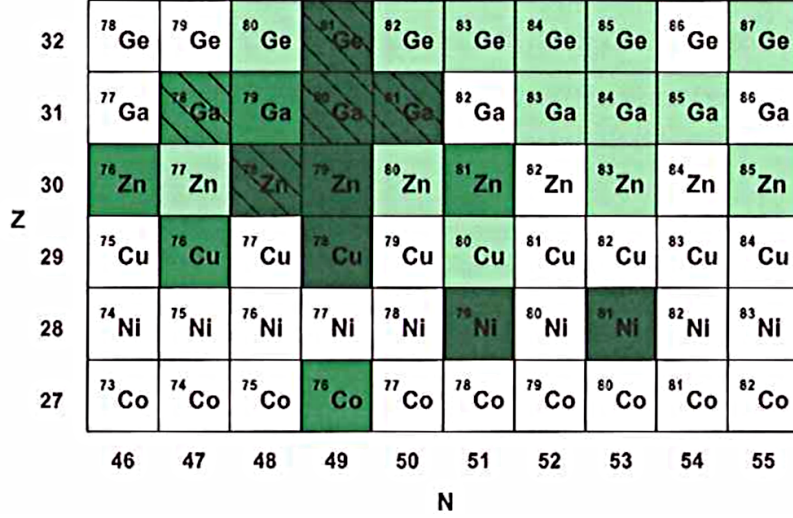
Figure 1.5: A nuclear chart of A ~ 80 region taken from Figure 1 of Reference [10]. Color codes represent how much the increase by a factor of 100 over a baseline simulation in the capture rate affects the overall r-process abundance pattern, grouped by 5-10% (lightest shading), 10-15%, and larger than 15% (darkest shading).

information, however, it was not possible to estimate the neutron-capture rate on ^{80}Ge with any level of confidence.

In addition, from the perspective of nuclear structure, the spins and parities of the low-lying intruder states on ^{81}Ge need to be confirmed or refuted in order to understand the shape coexistence in odd-mass $N = 49$ isotones. Meyer *et al.* [40] explained the low-lying intruder states in ^{83}Se using the unified-model calculations which included an interaction with single-hole states coupled to the collective excitations of the underlying core. Because it had been known that the collective behavior of the core reduced excited state energies, the paper noted that the excitation energy of intruder states in a series of isotopes was the lowest where the core neutrons are at mid-shell, where the core nucleus has the highest degree of collectivity. While the paper suggested that the lowest excitation energy of the $\frac{5}{2}^+$ state in odd-mass $N = 49$ isotones was expected to occur at the nucleus ^{83}Se ($Z = 34$) instead of the mid-shell ($Z = 39$) due to the $Z = 40$ subshell closure, there were

no measurements about the spin and spectroscopic factor of the $\frac{5}{2}^+$ state of the even $Z < 34$, $N = 49$ isotones, such as ^{81}Ge, supporting this suggestion.

Such information can be extracted from measurements of (d,p) reactions on neutron-rich nuclei, such as ^{80}Ge. The transfer reaction method allows the determination of both the Q-value and the angular distributions of populated levels, confirming the spins and parities of states in ^{81}Ge. Also, the spectroscopic factors can be extracted by comparing theoretical calculations with the measured angular distributions.

1.4 Structure of the Dissertation

The structure of the remainder of the dissertation is as follows:

Chapter 2 introduces a basic formalism of the structure and reaction theories, which is related to the spectroscopic analysis of the data. This chapter also presents a similar formalism for direct neutron capture calculations.

Chapter 3 includes an overview of the radioactive ion beam production and delivery, and descriptions of targets, detectors, and experimental techniques used in the ^{80}Ge$(d,p)^{81}$Ge transfer reaction in inverse kinematics measurements.

Chapter 4 describes the calibrations and data analysis of the measurements.

In the final chapter, the implications and conclusions of the measurements are discussed, particularly with regard to spectroscopic strengths of measured excited states in the nucleus ^{81}Ge and their application in astrophysics. At the end of the chapter, some future directions for this research are outlined.

There is also an ORNL DAQ ASICs manual added as an appendix in order to help users begin with the ORNL DAQ ASICs system.

Chapter 2

Theoretical Considerations

Spectroscopic information on nuclei can be extracted from nuclear reaction experiments. This includes masses, excited state energies, spins and parities of states and spectroscopic factors. In order to interpret the measurements correctly one has to understand basic theories of nuclear structure and nuclear reactions. This chapter will briefly describe the concept of the nuclear shell model and current standard theories of direct nuclear reactions. In addition, this chapter will also discuss how the experimental observables are related to the reaction theory at the end of the chapter.

2.1 Nuclear Structure Theory

2.1.1 Spherical nuclear shell model

An atomic nucleus is the core of every atom, consisting of nucleons (protons and neutrons). A nucleus can be identified by the total amount of positive charge, Z, and the total number of nucleons, A, in the nucleus. Since a proton is the only positively charged particle in the nucleus, Z is the number of protons as well. Then, the number of neutrons, N, in the nucleus can be $N = A$ - Z.

In order to describe how a nucleus is constructed from protons and neutrons, one has to understand how nucleons interact via the strong force [16]. While the electric

force includes attraction or repulsion between two point charges, the strong force results in interactions between nucleons. The strong force is attractive over a short distance (~ 2 fm) and repulsive at even shorter distances (~ 0.25 fm) [44]. There is evidence to suggest that nucleons interact not only through mutual two-body forces, but through three-body (or four-body) forces as well.

One way to describe the system is through the spherical nuclear shell model which describes a nucleus as a collection of single nucleons moving in a mean field potential generated by all other nucleons, analogous to the atomic shell model. The potential is considered as spherically symmetric, only depending on the radial coordinate "r". This nuclear shell model was developed by Mayer [32] with a strong spin-orbit interaction introduced by Haxel, Jensen, and Suess [33], and explained the observed closed shells in stable isotopes.

In the nuclear shell model, one can describe a nucleon in the nucleus in a simple mathematical way using the Schrödinger equation which can be expressed by

$$\left[-\frac{\hbar^2}{2m}\nabla + V(r) \right] \psi(r) = E\psi(r) \tag{2.1}$$

where $\hbar$ is the reduced Planck constant ($=h/2\pi$ where h is Planck constant), m is the mass of the nucleon, V is the mean field potential, E is the energy and r is the distance of the nucleon from the center of the potential. The mean field potential, $V(r)$, is generated by all other nucleons in the nucleus and this term mainly determines the energy levels of the nucleus. The most commonly used form for the mean field potential is the Woods-Saxon potential [45], which can be written as

$$V(r) = V_{ws}(r) = \frac{-V_0}{1 + \exp\left[(r-R)/a\right]} \tag{2.2}$$

where V_0 is the potential depth, R is the mean nuclear radius which has the form $R = r_0 A^{1/3}$ fm and a is the diffuseness, which defines the smoothness of the edge. The depth V_0 is adjusted to give the proper separation energies. The shape of the

potential describes the charge and matter distribution measured over a wide range of nuclei, falling smoothly to zero beyond the mean radius R [45].

The mean field potential with the Woods-Saxon form alone reproduces only the first few magic numbers. This problem can be solved by including a spin-orbit potential, $V_{so}(r)l \cdot s$, which takes into account the intrinsic spin of the nucleon relative to its orbital angular momentum [46]. The magnitude of the intrinsic spin of a single nucleon is $\frac{1}{2}$, and thus the possible values for the total angular momentum j for a given energy level are $j = l + \frac{1}{2}$ or $j = l - \frac{1}{2}$. Since the Hamiltonian commutes with j^2, l^2 and s^2, the product $l \cdot s$ can be written as

$$l \cdot s = \frac{1}{2} \left(j^2 - l^2 - s^2 \right). \tag{2.3}$$

Thus, the expectation value of $l \cdot s$ becomes

$$\langle l \cdot s \rangle = \frac{1}{2} \left[j(j+1) - l(l+1) - s(s+1) \right] \hbar^2 \tag{2.4}$$

$$= \begin{cases} \frac{1}{2} l \hbar^2 & \text{where } j = l + \frac{1}{2} \\ -\frac{1}{2}(l+1)\hbar^2 & \text{where } j = l - \frac{1}{2} \end{cases}. \tag{2.5}$$

Therefore, by choosing $V_{so}(r)$ to be negative, the larger j is pushed downward while the smaller j is lifted up resulting in the production of large shell gap for a certain number of nucleons, called a closed shell or magic number. It is known that $V_{so}(r)$ is mainly a surface effect and is connected to the average potential. Hence, the total mean field potential can be written as

$$\begin{aligned} V(r) &= V_{ws}(r) + V_{so}(r)l \cdot s \\ &= \frac{-V_0}{1 + \exp\left[(r-R)/a\right]} + \frac{V_{ls}}{r_0^2} \frac{1}{r} \frac{1}{1 + \exp\left[(r-R)/a\right]} l \cdot s \end{aligned} \tag{2.6}$$

where V_{ls} is the spin-orbit potential depth [47]. This spin-orbit potential, together with the Woods-Saxon potential, predicts all the shell closures consistent with
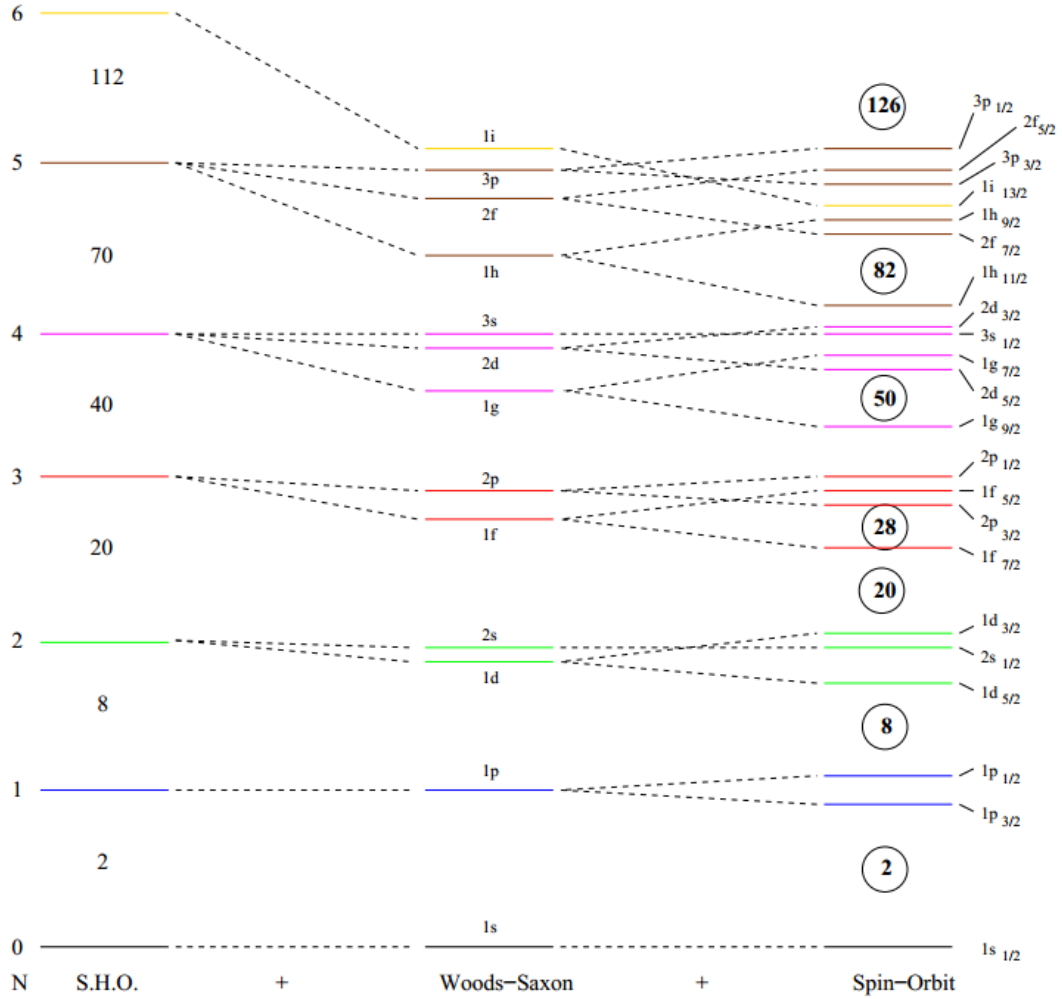
Figure 2.1: The energy levels calculated using various potentials. On the left plot, the simple harmonic oscillator form was used. The middle one shows the energy levels for the Woods-Saxon form without the spin-orbit coupling. The right one shows the levels using a Woods-Saxon form with a spin-orbit component. Numbers in black circles are the magic numbers indicating shell closures. Figure taken from Reference [11]

experimental observation. Figure 2.1 shows the calculated energy levels depending on various potentials applied to the Schrödinger equation.

The spherical shell model describes well the properties of nuclei having one valence nucleon from a closed shell, called a single-particle nucleus. The closed shell is filled with $(2j+1)$ particles for each angular momentum j, hence any state of total angular momentum J possesses $(2j+1)$ degenerate sub-states. From the Pauli exclusion principle, spins of each two particles will be antisymmetric and thus, the J will be zero and its parity is also even when all the $(2j+1)$ particles occupy the closed shell. Therefore, for a configuration of a single particle, one expects a number of low-lying states having angular momentum and parity determined by the quantum numbers of the orbits available to the single particle. Additional properties, such as the moments involved in electromagnetic transitions and β decay, provide further information regarding the adequacy of the single-particle description for the nucleus. For nuclei having one less nucleon than the closed shell, configurations obtained by removing a particle from closed shells, single-hole configurations, are expected to have properties related in a simple manner to those of single-particle configurations.

Since this shell model is mainly designed to describe nuclei close to shell closures, this does not agree with experimental values when applied to nuclei in which there are many valence nucleons outside the closed shell. The following section will show that the model is used as a starting basis for the study of complicated nuclei, together with the residual interactions considered.

2.1.2 Residual interactions

For a mid-shell nucleus, one that is far from shell closures, the spherical nuclear shell model fails its fundamental assumption that nucleons mainly move independently from each other in an average field with a large mean-free path. Thus, local microscopic considerations, such as a paring energy between two identical nucleons, proton-neutron interactions, collective motion, non-spherical shape of the nucleus

and so on, must be included as perturbations into the Hamiltonian of the nuclear shell model. These residual interactions result in physical eigenstates which consist of multiple single-particle configurations in a phenomenon, known as configuration mixing. According to the shell model, for a simple example, a nucleus ^{18}O can be described by two valence neutrons outside a ^{16}O core. The $1d_{5/2}$ and $2s_{1/2}$ orbits are low-lying states above the closed shell. Thus, the configuration of particles for a particular J^π state, assuming the ^{16}O core has 0^+, will be

$$
\begin{aligned}
J^\pi &\rightarrow \quad | \, nl_j; J^\pi_{core} \rangle \\
0^+ &\rightarrow \quad | \, (1d_{5/2})^2; 0^+ \rangle, \quad | \, (2s_{1/2})^2; 0^+ \rangle \\
2^+ &\rightarrow \quad | \, (1d_{5/2})^2; 0^+ \rangle, \quad | \, (1d_{5/2})(2s_{1/2}); 0^+ \rangle \\
3^+ &\rightarrow \quad | \, (1d_{5/2})(2s_{1/2}); 0^+ \rangle \\
4^+ &\rightarrow \quad | \, (1d_{5/2})^2; 0^+ \rangle
\end{aligned}
$$

where J^π_{core} is the total angular momentum and parity of the closed shell. Due to configuration mixing, the single-particle strength is spread across various states which all have the same J^π. Furthermore, the configuration mixing becomes much more complicated when both the number of protons and neutrons of a nucleus are away from the closed shell, because the number of valence nucleons in the nucleus determines the number of possible combinations of the configuration mixing.

Practically, the matrix elements for the residual interactions are optimized to reproduce experimental observables in the relevant mass region; the optimized interaction is called an effective interaction. Then, the interaction can be considered as a perturbation expansion and combined with the model space to study the nuclear structure at low excitation energy for any related nucleus.

As introduced in Section 1.2, shape coexistence is the quantum mechanical mixing of eigenstates groups characterized by different intrinsic shapes such as spherical, oblate and prolate shapes [36]. These different shapes can occur at similar energies in

one nucleus and this coexistence is known to occur in odd-mass nuclei [34] and even-even nuclei [35]. Various arrangements of nucleons involve sets of energy eigenstates with different electric quadrupole properties such as moments and transition rates, and different distributions of proton pairs and neutron pairs with respect to their Fermi energies. Sometimes two such structures are inverted as a function of the nucleon number, resulting in intruder states or a sudden and dramatic change in ground-state properties in neighboring isotopes and isotones [40].

In the case of single-hole (N_{magic}-1 or Z_{magic}-1) nucleon systems, properties of the intruder states related to the shape coexistence can be explained by a model taking into account 1h-core coupled configuration and (1p-2h)-core coupled configurations simultaneously based on a spherical particle-core coupling model, called the unified model [34].

The Hamiltonian for nuclei with single-particle (hole) configurations coupled to the collective excitations of the underlying core nucleus can be written as

$$H = H_{\mathrm{core}} + H_{\mathrm{s.p.}} + H_{\mathrm{s.h.}} + H_{\mathrm{p\text{-}core}} + H_{\mathrm{h\text{-}core}} + H_{\mathrm{ph\text{-}core}} + V_{\mathrm{hh}} + V_{\mathrm{pp}} + V_{\mathrm{ph}} \qquad (2.7)$$

where H_{core} describes the low-lying collective excitations of the even-even core nucleus; $H_{\mathrm{s.p.}}$ and $H_{\mathrm{s.h.}}$ describe the single-particle and the single-hole motion; $H_{\mathrm{p\text{-}core}}$, $H_{\mathrm{h\text{-}core}}$ and $H_{\mathrm{ph\text{-}core}}$ describe the interaction of the single-particle, single-hole and single-particle-hole motion with the collective excitations of the core nucleus; and V_{hh}, V_{pp} and V_{ph} describe the residual hole-hole, particle-particle and particle-hole interactions. For the 1p-2h configuration system, the Hamiltonian can be diagonalized to the 2h-core configuration space and then coupled to single-particle (1p) excitations across the closed shell. When the coupling between the h-core configuration and the p-core configuration is introduced, the excitation energy generated by the 1p excitations change. This coupling depends on the the strength of the collective Eλ transition

probability in the even-even nucleus, β_λ, which expressed as

$$\beta_\lambda \equiv \frac{B(E\lambda; 0\rightarrow\lambda)^{1/2}}{(3/4\pi)ZeR_0^\lambda} \tag{2.8}$$

where $B(E\lambda; 0\rightarrow\lambda)$ represent a transition strength, Ze is the charge of nucleus, R_0 represents the constant ($= 1.25$ fm). Thus, the coupling strength, ξ_λ, can be defined as

$$\xi_\lambda \equiv \left\langle \frac{r\partial V_{\text{ph}}}{\partial r} \right\rangle \beta_\lambda \frac{1}{\sqrt{\pi}\hbar\omega_\lambda} \tag{2.9}$$

where $\hbar\omega_\lambda$ denotes the phonon energy. If the ξ_λ is stronger, it lowers the excitation energy more and causes the intruder states [34].

In the calculations described above, the excitation energy will be determined by three parameters: single-particle energies, coupling strengths ξ_λ and the residual interaction matrix element. The first two factors are obtained from experiments, and the third one can be a fine tuning parameter.

For nuclei near the $N = 50$ neutron closed shell, general properties of intruder states in the shape coexistence are found as following [40]:

(1) a set of "*extra*" low-lying ($E_x \lesssim 1$ MeV) levels in the energy region of the $| (1g_{\frac{9}{2}})_{gs}; 2^+_{core} \rangle$ multiplet.

(2) large spectroscopic factors for lp-2h configurations through the $N = 50$ neutron closed shell.

(3) strongly-enhanced intraband $E2$ transitions in the particle-core coupled system.

(4) highly retarded $E1$ transitions to the hole and hole-core states.

(5) rather strong $M1$ transitions from levels in the vicinity of the $| (1g_{\frac{9}{2}})_{gs}; 2^+_{core} \rangle$ multiplet energy to the $J^\pi = \frac{9}{2}^+$ ground state.

This work presents extraction of the spectroscopic factors of intruder states in ^{81}Ge odd-mass nucleus. Shape coexistence exhibited by the nucleus will be discussed in Section 5.1.

2.2 Nuclear Reaction Theory

When an incoming particle reacts with a target nucleus, the various outcomes are determined by a combination of three factors: the reaction mechanism, the interaction between the projectile and the target, and the internal structure of the nuclei involved. In order to understand the nuclear structure of ^{81}Ge, an inverse kinematics ^{80}Ge$(d,p)^{81}$Ge direct reaction has been measured in the present work. Therefore, an understanding of the basic theory of direct nuclear reactions including the distorted-wave approach is necessary and described in the following sections.

2.2.1 Nuclear reaction terminology

When two nuclei collide, the type of reaction that occurs can be defined by the outcomes. Sometimes more than two final massive products are emitted, or there may be just one, as in a capture reaction. Also, the final products can be identical to the initial ones. In a particular example of a stripping reaction, a deuteron hits the target and transfers its neutron to the target hence the proton comes out as an ejectile. The nuclear reaction ^{80}Ge$(d,p)^{81}$Ge(or $d + {}^{80}$Ge $\rightarrow p + {}^{81}$Ge in another notation) is a stripping reaction.

Another way of categorizing the nuclear reactions is by the energy difference between before and after the collision. When the kinetic energy of the system is conserved with the same products during the reaction, it is elastic scattering. If the kinetic energy of the system is changed but the same products, then it is inelastic scattering. Each outcome of the reaction which can occur, with well-defined quantum states of the participants, is referred to as a channel. In the reaction of "$d + {}^{80}$Ge $\rightarrow p + {}^{81}$Ge", for example, "$d + {}^{80}$Ge" is called the entrance (or incident) channel and "$p + {}^{81}$Ge" is called the exit channel.

In elastic scattering theory of a two non-relativistic particle collision, the basic assumption is that the elastic scattering has been caused by a potential $V(r)$ in a short range compared to the distance of the measurement, assumed for simplicity to

21

be spherically symmetric. Thus, the initial (ψ_i) and final (ψ_f) wave functions far from the center can be written as

$$\psi_i \sim e^{ikz} \sim e^{ikr\cos\theta} \tag{2.10}$$

and

$$\psi_f \sim e^{ikr\cos\theta} + f(\theta)\frac{e^{ikr}}{r} \tag{2.11}$$

where k is the wave number (the momentum divided by $\hbar$) and the function $f(\theta)$ is defined as the amplitude of the outgoing spherical wave relative to the incoming plane wave in the stationary-state scattering process, called the scattering amplitude.

The differential cross section is the ratio between the probability current density of the incoming particle (j_i) and the outgoing particle (j_r). The current density can be defined as

$$j_i = \frac{\hbar}{m} Im \left\{ e^{-ikz} \frac{d}{dz} e^{ikz} \right\} = \frac{\hbar k}{m}, \tag{2.12}$$

$$j_r \sim \frac{\hbar}{m} Im \left\{ f^*(\theta) \frac{e^{ikr}}{r} \frac{\partial}{\partial r} \left[f(\theta) \frac{e^{ikr}}{r} \right] \right\} = \frac{\hbar k}{mr^2} \mid f(\theta) \mid^2 . \tag{2.13}$$

Therefore, the differential cross section can be written as,

$$\sigma(\theta) \quad \equiv \quad \frac{d\sigma}{d\Omega} \equiv \frac{j_r r^2}{j_i} \quad = \quad \mid f(\theta) \mid^2 . \tag{2.14}$$

The total cross section is then obtained by integrating Eq. 2.14, i.e.,

$$\sigma = \int \frac{d\sigma}{d\Omega} d\Omega = 2\pi \int_{-1}^{+1} \mid f(\theta) \mid^2 d(\cos\theta). \tag{2.15}$$

Since the interaction between nuclei exhibits both a short-range attractive nuclear potential and a long-range Coulomb repulsion, an additional finite-range correction has to be added. Thus, the scattering potential may be written as $V_{nc}(r) = V_c(r) + V_n(r)$ for some finite-range potential $V_n(r)$ and point-Coulomb potential

$V_c(r)$ [48]. The differential cross section derived from the point-Coulomb potential, $\sigma_{Ruth}(\theta)$, is called the Rutherford cross section, because the result is the same as in the Rutherford scattering theory. Then, the elastic cross section regarding the potential $V_{nc}(r)$, $\sigma_{nc}(\theta)$, can be presented in terms of the ratio to Rutherford cross section, since it diverges to infinity at small angles, written as

$$\sigma_{el}/\sigma_{Ruth} \quad \equiv \quad \sigma_{nc}(\theta)/\sigma_{Ruth}(\theta) \tag{2.16}$$

which becomes unity at small angles.

For multi-channel reactions, where the incoming particles are different from outgoing particles, the simple calculation described above can not be applied. The wave functions of all particles must be taken account in the calculation [48, 49, 50].The next section will show one example of approaches to describe the reaction more accurately.

2.2.2   Distorted wave Born approximation

For a two channel reaction, $A(a, b)B$, the wave function of the entrance channel i and exit channel f, ψ_i and ψ_f, can be written as

$$\psi_i(\mathbf{r}_i) \equiv \psi_a(\mathbf{r}_a)\psi_A(\mathbf{r}_A), \tag{2.17}$$

$$\psi_f(\mathbf{r}_f) \equiv \psi_B(\mathbf{r}_B)\psi_b(\mathbf{r}_b), \tag{2.18}$$

where $\mathbf{r}_x$ represents the internal coordinates of a system x. The eigenfunctions, ψ_x, are solutions to the Schrödinger equations governed by the internal Hamiltonians H_x,

with eigenvalues, ϵ_x:

$$H_i\psi_i \equiv (H_a + H_A)\psi_i = \epsilon_i\psi_i, \tag{2.19}$$

$$H_a\psi_a = \epsilon_a\psi_a, \quad H_A\psi_A = \epsilon_A\psi_A, \tag{2.20}$$

$$H_f\psi_f \equiv (H_b + H_B)\psi_f = \epsilon_f\psi_f, \tag{2.21}$$

$$H_b\psi_b = \epsilon_b\psi_b, \quad H_B\psi_B = \epsilon_B\psi_B, \tag{2.22}$$

The total wave function for the system, Ψ_i, can be expanded in terms of a complete set of eigenfunctions of the internal states of a partition:

$$\Psi_i = \sum_f \xi_f(\mathbf{r}_f)\psi_f(\mathbf{r}'_f) \tag{2.23}$$

where the ξ_f are projections of Ψ_i onto the f channel, and $\mathbf{r}'_f$ is the internal coordinates of f channel.

If a channel potential can be composed of two parts $V(r) = V_1(r) + V_2(r)$, where V_1 is the interaction of interest with a relatively small effect and V_2 is the distorting potential, then it is possible to treat V_1 as a perturbation to the original solution of V_2. Thus, the distorted wave solution of the Schrödinger equation including only V_2, $\chi_f^{(-)}$, can be found and has the form of the iterated Born series. When the series is truncated after the first term for approximation, it is called the distorted-wave Born approximation (DWBA) [48, 49, 50]. Therefore, the transition amplitude, $T_{fi}(\mathbf{k}_f, \mathbf{k}_i)$, can be written as

$$T_{fi}(\mathbf{k}_f, \mathbf{k}_i) = T_{fi}(\mathbf{k}_f, \mathbf{k}_i)^{(0)}\delta_{if} + \left\langle \chi_f^{(-)*}(\mathbf{k}_f)\psi_f \mid W_f \mid \Psi_i^{(+)}(\mathbf{k}_i) \right\rangle \tag{2.24}$$

where $T_{fi}(\mathbf{k}_f, \mathbf{k}_i)^{(0)}$ is the elastic transition amplitude and $W_f \ (= V_1 - V_2)$ is the residual interaction.

Because the elastic scattering is the dominant part of the total wave function, $\Psi_i^{(+)}$, it is reasonable to approximate the function by the distorted elastic scattering

wave function of the entrance channel, $\chi_i^{(+)}$, i.e.

$$\Psi_i^{(+)} \approx \chi_i^{(+)}(\mathbf{r}_i)\psi_i(\mathbf{r}'_i). \tag{2.25}$$

By substituting the approximated $\Psi_i^{(+)}$ into the Eq. 2.24, the transition amplitude, $T_{fi}(\mathbf{k}_f, \mathbf{k}_i)$, becomes

$$T_{fi}(\mathbf{k}_f, \mathbf{k}_i) = T_{fi}(\mathbf{k}_f, \mathbf{k}_i)^{(0)}\delta_{if} + \left\langle \chi_f^{(-)*}(\mathbf{k}_f)\psi_f \mid W_f \mid \chi_i^{(+)}(\mathbf{k}_i)\psi_i \right\rangle. \tag{2.26}$$

The second part of the Eq. 2.26 shows, explicitly, the nuclear reaction contribution ($\chi_f^{(-)*}$ and $\chi_i^{(+)}$) and the nuclear structure contribution (ψ_f and ψ_i) to the transition $i \to f$.

The choice of potentials V_2 is crucial, because the differential cross section, $d\sigma/d\Omega$, is proportional to the square of transition amplitude, which was described in Eq. 2.26, that is,

$$\left(\frac{d\sigma}{d\Omega}\right)_{DWBA} \propto \mid T_{fi}(\mathbf{k}_f, \mathbf{k}_i) \mid^2 . \tag{2.27}$$

The potential V_2 is arbitrary, but is chosen so as to account for the elastic scattering in the f channel.

2.2.3   Optical model potential

The potential V_2 is related to scattering states, just as effective interactions are related to bound states, and is usually chosen as an optical model (OM) potential. The OM potential is complex, and takes, in general, the form of a Coulomb potential, a volume Woods-Saxon potential, a surface potential formed by the derivative of a

Woods-Saxon, and a spin-orbit term [51], that is,

$$V_{OM}(r) = V_2(r)$$

$$= V_c - V_{vol}f(x_{Vvol}) + \left(\frac{\hbar}{m_\pi c}\right)^2 V_{so}(l \cdot s)\frac{1}{r}\frac{d}{dr}f(x_{so})$$

$$- i\left[W_{vol}f(x_{Wvol}) - 4W_{surf}\frac{d}{dx_{surf}}f(x_{surf})\right], \quad (2.28)$$

$$V_c = \begin{cases} ZZ'e^2/r & r \geq R_c \\ (ZZ'e^2/2R_c)(3 - r^2/R_c^2) & r < R_c \end{cases},$$

$$R_c = r_c A^{1/3},$$

$$f(x_i) = (1 + e^{x_i})^{-1},$$

$$x_i = (r - r_i A^{1/3})/a_i,$$

where

V_c : a Coulomb potential,

V_{vol} and W_{vol} : a real and imaginary depth of the nuclear volume potential,

r_{Vvol} (a_{Vvol}) and r_{Wvol} (a_{Wvol}) : a real and imaginary radius (diffuseness) of the nuclear volume potential,

V_{so} and r_{so} (a_{so}) : a depth and radius (diffuseness) of spin-orbit potential,

W_{surf} and r_{surf} (a_{surf}) : a depth and radius (diffuseness) of the nuclear surface potential.

Some constraints such as ignoring the spin-orbit term are applied to the general form depending on the OM parameterizations. The real part of the potential describes the elastic scattering channel. And, the imaginary terms of the potential are used to model the effects of reaction channels other than elastic scattering. Absorption is often accounted for by the surface term, with W_{vol} set to zero.

In practice, since the OM potentials describe the measured elastic scattering in both the entrance and exit channels, one can use parameters for specific nucleus-nucleus reactions obtained from fitting elastic scattering data for the relevant entrance

and exit channels. However, such approaches become difficult when radioactive beams are involved where elastic scattering data is often not available especially for a large range of beam energies and nuclei. In addition, the OM potential parameters cannot be accurately determined from the data at a single incident energy. To be more accurate in this case and to apply the analysis to a wide range of target-nucleus and bombarding energies, it is desirable to use global OM potentials which are determined by fitting a large amount of data over a broad range of nuclei and energies, or a microscopic global optical potential which is derived from the relevant nuclear densities using effective Skyrme interactions.

In the present work, global OM potential parametrizations such as Lohr-Haeberli (LH) [52], Bechetti-Greenlees (BG) [4] and Chapel-Hill 89 (CH89) [5], were used. The entrance channel parameters were obtained by the LH parametrization. LH analyzed (d,d) elastic scattering data of nuclei with masses, A, greater than 40 and deuteron beam energies, E, between 8 MeV and 13 MeV.

For OM potential parameters of the exit channel, BG was used here for the DWBA calculation of the ^{80}Se$(d,p)^{81}$Se reaction in order to compare the result with Reference [3], and CH89 was applied to rest of the calculations. The BG parametrization is suitable for in the mass range $A > 40$ and the nucleon laboratory energy range $20 < E < 50$ MeV. These parameters were determined by fitting simultaneously a large sample of the available proton-nucleus data, and independently, a large sample of the available neutron-nucleus data [4]. The CH89 parametrization is suitable for nuclei in the mass range $40 \leq A \leq 209$ and the nucleon laboratory energy range $10 \leq E \leq 65$ MeV [5]. It was obtained by fitting simultaneously a large database of nearly 300 proton-nucleus and neutron-nucleus differential cross sections and analyzing powers.

2.2.4 Adiabatic wave approximation

In DWBA calculations for deuteron-induced transfer reactions, the effects of deuteron break up are neglected except for their influence on the absorptive imaginary term of the optical potential. This introduces a significant source of uncertainty for beam energies above the Coulomb barrier, since elastic scattering is largely peripheral while transfer and break-up processes occur at the nuclear surface or interior. Since the binding energy of deuteron is only 2.2 MeV, the treatment of deuteron break up becomes important. In the ADiabatic Wave Approximation (ADWA) of Johnson and Soper [53], break up is taken into account in an explicit way. Instead of the deuteron OM potential of entrance channel, V_2^d, the adiabatic potentials of the proton and neutron OM potentials, $V_2^p + V_2^n$, are chosen. The OM potentials V_2^p and V_2^n are determined by fitting to neutron and proton elastic-scattering data at half of the incident deuteron energy, or the global OM potentials can be used to get those parameters. In the present work, CH89 was applied to find OM potentials V_2^p and V_2^n. Thus, adiabatic potentials for break up are constructed by the summation of these two potentials evaluated at the same point. A finite-range ADWA method, which generates an averaged adiabatic potential by folding with a weight factor, $V_2^{pn}(r)|u_{l0}(r)|^2$, was also introduced by Johnson and Tandy [54]. These methods have been shown to be significantly more precise than the DWBA method, and maintain similar ease of implementation [55].

2.3 Connections between Theory and Experiment

2.3.1 Kinematics of nuclear reactions

As seen in Figure 2.2, the conservation of total energy and linear momentum in the laboratory frame gives

$$E_a + E_A + Q = E_b + E_B, \tag{2.29}$$
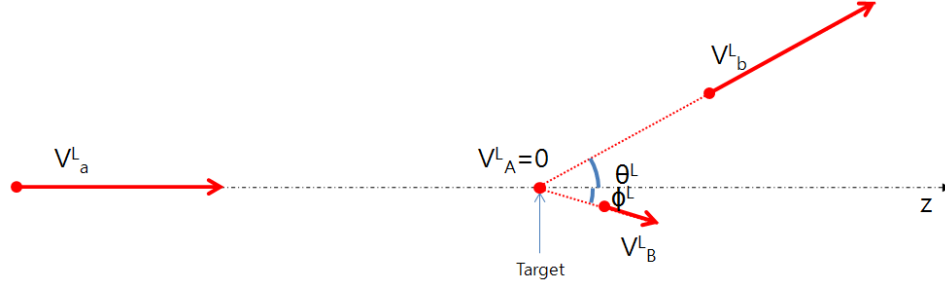
Figure 2.2: Vector diagram of a nuclear reaction $a + A \rightarrow b + B$ in the laboratory frame.

$$\sqrt{2m_a E_a} = \sqrt{2m_b E_b}\cos\theta^L + \sqrt{2m_B E_B}\cos\phi^L, \tag{2.30}$$

$$\sqrt{2m_b E_b}\sin\theta^L = \sqrt{2m_B E_B}\sin\phi^L \tag{2.31}$$

where $E_A = 0$ with a fixed target and Q is the Q-value of the reaction that is the energy gained or lost due to the difference between the initial and final masses:

$$Q = (m_a + m_A - m_b - m_B)c^2. \tag{2.32}$$

By eliminating E_B and ϕ from Eq. 2.29, the Q-value can be found as depending on E_b, which is the measurement parameter in an experiment:

$$Q = E_b(1 + \frac{m_b}{m_B}) - E_a(1 - \frac{m_a}{m_B}) - \frac{2}{m_B}\sqrt{m_a m_b E_a E_b}\cos\theta^L. \tag{2.33}$$

Although it would be desirable to use energetic deuterons or protons as beams and the neutron-rich nuclei as targets, it is impossible to make those targets because their lifetime is too short to exist as targets before they would decay. The only possible way to achieve the desired reaction measurement is to use inverse kinematics, that is, to make and accelerate the radioactive nuclei to bombard in this case, the deuteron target and to measure the energy and angle of ejectiles of protons. Figure 2.3 shows an example of normal kinematics and inverse kinematics of the transfer reaction $^{80}\text{Ge}(d,p)^{81}\text{Ge}$.
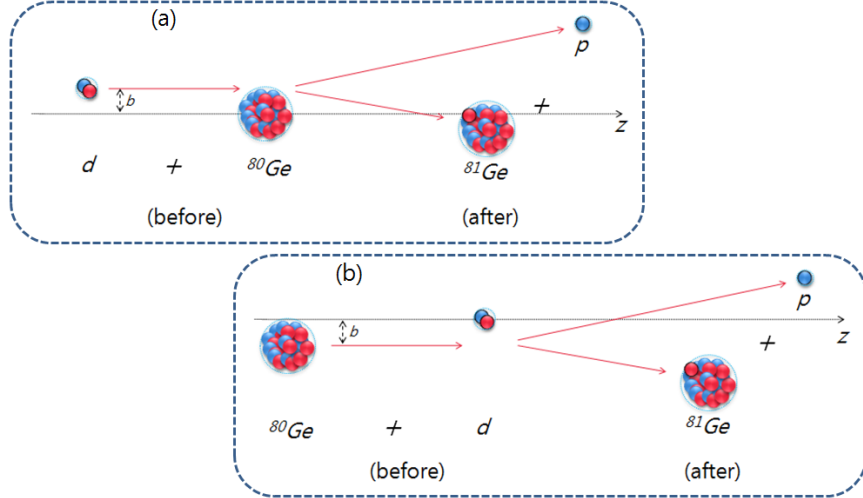
Figure 2.3: Vector diagrams of a nuclear reaction $d + {}^{80}\text{Ge} \rightarrow p + {}^{81}\text{Ge}$ in normal (a) and inverse (b) kinematics in the laboratory frame

In inverse kinematics, in order to reproduce the same center-of-mass energy in the reaction as in normal kinematics measurement, the heavy beam must be accelerated to a speed greater than 0.1c, where c is the speed of light. The center-of-mass frame is, therefore, also moving at a similar speed with respect to the laboratory frame where the measurement is performed. This can be understood by the velocity diagram displayed in Figure 2.4, where $V_{C.M.}$ is the velocity of the center-of-mass in the laboratory frame; V_b^L and V_b^C are the velocity of the ejectile in the laboratory and center-of-mass frames. The corresponding laboratory and center-of-mass angles are θ^L and θ^C, respectively. There are two circles, which represent constraints on the velocities of the ejectile and recoil dependent on a fixed Q-value. Because the energy of the ejectile determines Q-value as seen in Eq. 2.33, three cases can be considered as $Q > 0$, $Q = 0$ and $Q < 0$.

The major effect of this inversion is to focus all of the heavy reaction products to forward angles in the laboratory frame, such that both beam and beam-like recoils follow close to the initial direction of the beam. In addition, the protons of interest are detected at backward laboratory angles (forward center-of mass-angles in normal

30
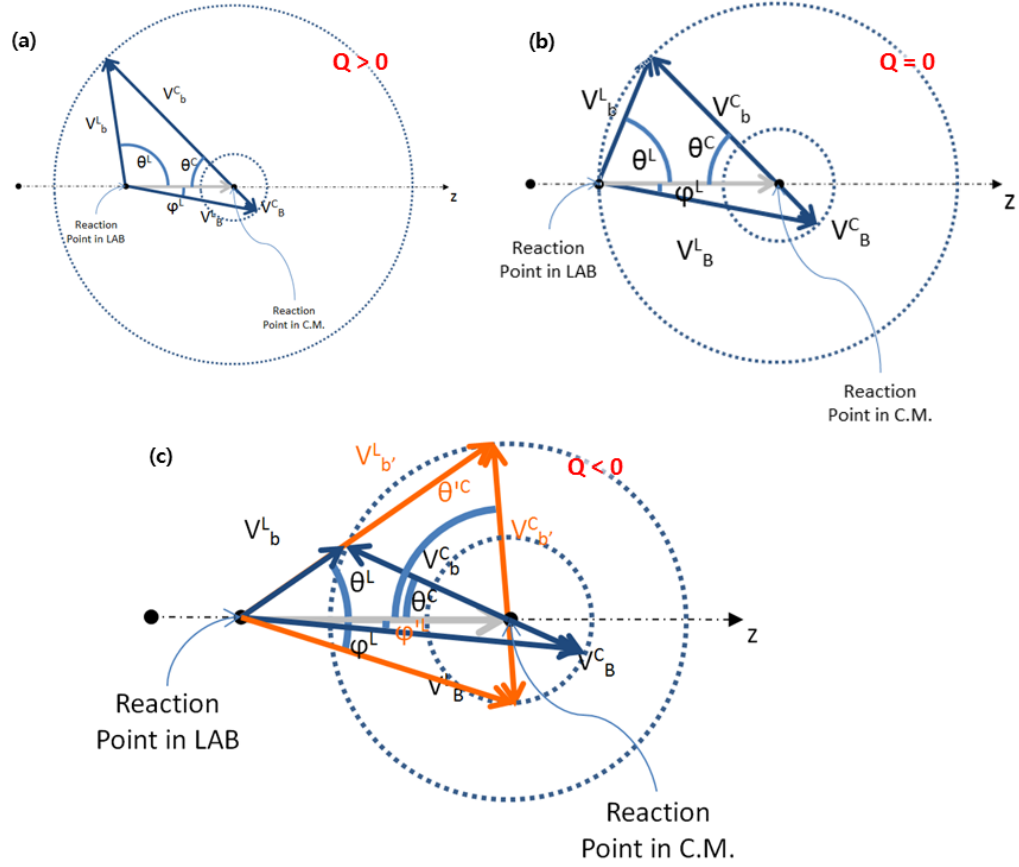
Figure 2.4: Velocity vector diagram for exit channel of the nuclear reaction $a + A \rightarrow b + B$ in case of $Q > 0$ (a), $Q = 0$ (b, elastic case) and $Q < 0$ (c) in the laboratory frame and the center-of-mass frame.

kinematics), but over a larger energy range than the range in normal kinematics. The detection of the protons must, therefore, involve good energy and angle resolution, and a large angular coverage.

In inverse kinematics nuclear reactions such as used in this experiment, a positive Q-value results in the ejectiles of most interest being emitted at backward angles in the laboratory frame. As seen in Figure 2.4 and from References [56, 57, 58], the velocity of the center-of-mass frame, $V_{C.M.}$ can be written as

$$V_{C.M.} = V_a^L \frac{m_a}{m_a + m_A}. \tag{2.34}$$

Therefore, the center-of-mass angle, θ^C, can be calculated by

$$\theta^C = \sin^{-1}\left(\frac{V_b^L \sin\theta^L}{\sqrt{(V_{C.M.})^2 + (V_b^L)^2 - 2V_{C.M.}V_b^L \cos\theta^L}}\right). \qquad (2.35)$$

Thus, by measuring V_b^L at the certain lab angle θ^L, one can find the corresponding Q-value and θ^C.

When the beam energy is very high and relativistic effects have to be considered, the conversion equation becomes more complicated as described in Reference [57]. In order to find the accuracy of the non-relativistic calculation, one can check Q-value difference [57, 58], that is,

$$\Delta Q = |Q_{nonrel}| - |Q_{rel}| \cong \frac{|Q_{nonrel}|^2}{2(m_A + m_a)} \qquad (2.36)$$

where Q_{nonrel} is the Q-value in non-relativistic calculation, Q_{rel} is from a relativistic calculation. In the present work, when we expect Q-values lower than 10 MeV, the ΔQ becomes ~ 0.6 eV, i.e. ,

$$\Delta Q \cong \frac{10^2}{2(80 \times 10^3 + 2 \times 10^3)} \cong 0.6 \text{ eV}. \qquad (2.37)$$

This small difference shows that consideration of the relativistic kinematics does not affect our measurement and the non-relativistic approach is safe to use.

2.3.2 Cross section and spectroscopic factors in transfer reaction

As discussed in Section 2.1.2 and 2.2.2, the single-particle strength of most states in a nucleus away from magic numbers is fragmented by the configuration mixing of levels of a nucleus. The strength is contained in the transition amplitude of the reaction, and is therefore directly related to the differential cross section, as shown in Eq. 2.26 and 2.27. The nuclear matrix element $\langle \psi_f \mid W_f \mid \psi_i \rangle$ in Eq. 2.26, with integration

performed over all coordinates independent of $\mathbf{r}_i$ and $\mathbf{r}_f$, can be expanded into the nuclear overlap integral, which carries single-particle state information (defined by the quantum numbers n,l,j and m), and the overlap function between the projectile and the ejectile. That is,

$$(\psi_f \mid W_f \mid \psi_i) \equiv \int \psi_f^* W_f \psi_i d\mathbf{r}'_f \tag{2.38}$$

$$= \int \psi_b^* \psi_B^* W_f \psi_a \psi_A d\mathbf{r}'_f \tag{2.39}$$

$$= \int \psi_b^* \psi_a W_f \psi_B^* \psi_A d\mathbf{r}'_f \tag{2.40}$$

$$= (\psi_b \psi_a) W (\psi_B \psi_A), \tag{2.41}$$

$$= \phi_a^b W \phi_A^B, \tag{2.42}$$

where $\mathbf{r}'_f$ represents all internal coordinates, W is an integrated form of the potential W_f over $\mathbf{r}'_f$ and ϕ_x^y is the overlap function between a nucleus y and a nucleus x. As we can write ψ_B as the projection of ψ_A similar to the Eq. 2.23, the overlap function, ϕ_A^B, can be rewritten as

$$\phi_A^B = \sum_{lj} \phi_{Alj}^B \langle J_A j M_A m \mid J_B M_B \rangle, \tag{2.43}$$

$$= \sum_{lj} \langle J_A j M_A m \mid J_B M_B \rangle \phi_{Alj}^B, \tag{2.44}$$

where $\langle J_A j M_A m \mid J_B M_B \rangle$ is a Clebsch-Gordon coefficient and ϕ_{Alj}^B is the overlap function for the single-particle basis-state having l and j. The partial wave components of ϕ_{Alj}^B can be written as the sum of spectroscopic amplitudes times normalized overlap functions:

$$\phi_{Alj}^B = \sum_{lj} A_{lj} \varphi_{Alj}^B, \tag{2.45}$$

where φ^B_{Alj} is a single-particle wave function normalized to unity as $||\varphi^B_{Alj}|| = 1$ and A_{lj} is a spectroscopic amplitude. The theoretical spectroscopic factor is then defined as the square of the spectroscopic amplitude,

$$S^B_A(lj) \quad \equiv \quad \mid A_{lj} \mid^2 \tag{2.46}$$

and gives the probability that when the nucleus B is in the state ψ_B, it will be found to be with orbital angular momentum l and total j relative to the nucleus A in state ψ_A. For a neutron transfer reaction with the even-even nucleus A described by the ground state ($J^\pi = 0^+$), the theoretical spectroscopic factor can represent the single particle strength of the state where the neutron populates.

The theoretical spectroscopic factor, however, is not observable and it is necessary to define another parameter representing the single particle strength, which can be extracted from an experimental observable. The calculated differential cross sections using the OM potentials are often calculated with the spectroscopic factor equal to one, $S^B_A(lj) = 1$. Thus, the experimental spectroscopic factor $S^B_A(lj)$ can be extracted as the ratio between the measured cross section for the formation of a state of the product nucleus and the calculated one using a scalable reaction theory such as DWBA or ADWA:

$$\left(\frac{d\sigma}{d\Omega}\right)_{exp} = S^B_A(lj) \left(\frac{d\sigma}{d\Omega}\right)_{theory}. \tag{2.47}$$

The experimental differential scattering cross section can be calculated by the equation

$$\left(\frac{d\sigma}{d\Omega}\right)_{exp} = \frac{dN/d\Omega \times \eta}{n\Phi} = \frac{N_{out}/d\Omega \times \eta}{nN_{in}} \tag{2.48}$$

where dN is the number of observed events in $d\Omega$ per unit time, η is the efficiency of the detector, n is the number of target particles by the beam, Φ is the incident flux (number of incident particles per unit area and per unit time), N_{in} is the total number of incoming particle in the beam for entire beam time, and N_{out} is the total

number of observed particle in $d\Omega$ for entire beam time. Therefore, by normalizing the calculated differential cross sections from the Eq. 2.27 by the measured one from the Eq. 2.48, the experimental spectroscopic factor $S_A^B(lj)$ can be extracted.

2.4 Direct Neutron Capture Theory

Direct capture (DC) reactions at thermonuclear neutron energies can be described by a similar nuclear reaction theory as that mentioned in previous sections with optical potentials in the entrance and exit channels [59]. Using the DWBA method, theoretical cross sections of A(n,γ)B can be calculated by [60, 61]:

$$\sigma_i^{th} = \int d\Omega \frac{d\sigma_i^{th}}{d\Omega_\gamma} \tag{2.49}$$

$$= \int d\Omega \ 2\left(\frac{e^2}{\hbar c}\right)\left(\frac{\mu c^2}{\hbar c}\right)\left(\frac{k_\gamma}{k_n}\right)^3 \frac{1}{2I_A+1}\frac{1}{2S_n+1}\times$$

$$\sum_{M_A M_n M_B,\sigma} |\ T_{M_A M_n M_B,\sigma}\ |^2 \tag{2.50}$$

where i is the state of the nucleus B, S_n and I_A (M_n, M_A, and M_B) are the spins (projections) of the corresponding nuclei, μ is the reduced mass in the entrance channel, σ is the polarization of the electromagnetic radiation (± 1), k_γ is the momentum of the emitted radiation, k_n is the entrance channel relative momentum, and T is the multipole expansion of the electromagnetic transition amplitude. The transition amplitude T usually includes electric dipole ($E1$) and quadrupole ($E2$) transitions as well as magnetic dipole ($M1$) transitions. The strongest direct transitions usually involve s-wave ($l = 0$) capture of the neutron, accompanied by an $E1$ (electric dipole) electromagnetic transition. Higher relative angular momentum captures are hindered by the centrifugal barrier at low neutron energies [16].

The direct neutron capture cross sections σ^{DC} can be obtained from the sum of all products of spectroscopic factors S_{lj}^i and the theoretical cross sections σ_i^{th} found

in the Eq. 2.49, that is,

$$\sigma^{DC} = \sum S_{lj}^{i} \sigma_{i}^{th}. \tag{2.51}$$

The spectroscopic factors S_{lj}^{i} are often extracted from a (d,p) transfer reaction A(d,p)B, and applied in the calculation.

Chapter 3

Experimental Setup

A study of the ^{80}Ge$(d,p)^{81}$Ge reaction in inverse kinematics using a radioactive ^{80}Ge beam was performed at the Holifield Radioactive Ion Beam Facility (HRIBF) at Oak Ridge National Laboratory (ORNL) in April, 2011. A 310 MeV (3.875 MeV per nucleon) ^{80}Ge beam bombarded a 174 μg/cm^2 CD$_2$ target for 5 days. The average beam rate was 120,000 particles per second (pps) and was composed of approximately 97% ^{80}Ge and 3% ^{80}Se. Various silicon detectors were used to detect protons from the reaction. Protons from the (d,p) reaction were detected at backward laboratory angles by two detectors of the Array for Nuclear Astrophysics Studies with Exotic Nuclei (ANASEN) [62], one detector of the Super Oak Ridge Rutgers University Barrel Array (SuperORRUBA) [63], one flat annular array of the Silicon Detector Array (SIDAR) [1] and one smaller annular detector of Micron style S1 (MINI) [64]. In order to detect forward-going reaction protons and elastically-scattered target deuterons, two detectors of ANASEN, one detector of SuperORRUBA and one detector of Oak Ridge Rutgers University Barrel Array (ORRUBA) [65] were installed at forward laboratory angles. A new fast ionization counter was placed downstream of the target to detect unreacted beam ions and recoil ions. The experimental configuration is shown in Figure 3.1. In this chapter, beam production, target fabrication, detector characteristics, and electronics will be described in detail.
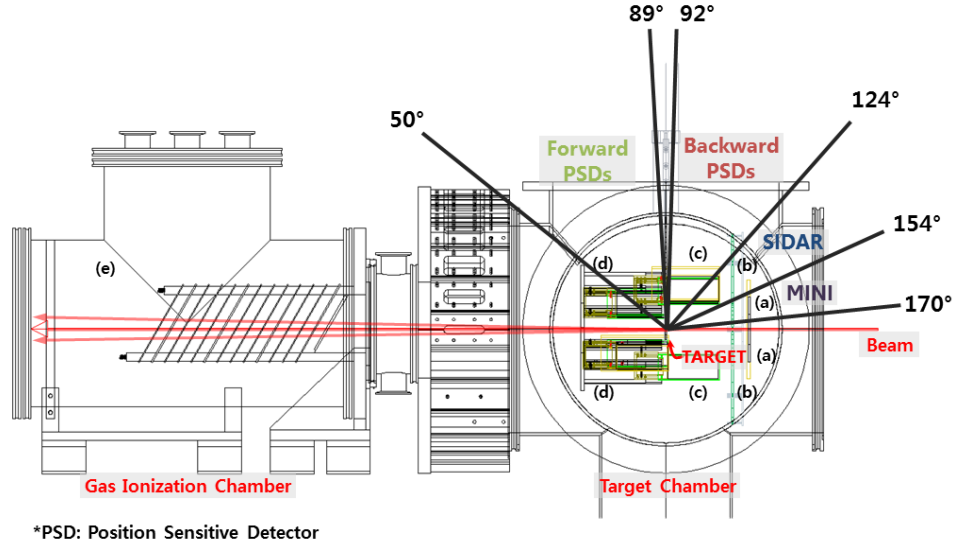
Figure 3.1: A schematic diagram of the detector setup for the ^{80}Ge$(d,p)^{81}$Ge reaction in inverse kinematics; (a) one MINI, (b) one SIDAR, (c) a barrel shape layout of two detectors of ANASEN, one detector of SuperORRUBA and one detector of ORRUBA, (d) a barrel shape layout of two detectors of ANASEN and one detector of SuperORRUBA and (e) Ionization Counter. [12]

3.1 ^{80}Ge Beam Production

The ^{80}Ge beam was produced at HRIBF, ORNL with the isotope separation on-line (ISOL) method [66]. A primary proton beam from the Oak Ridge Isochronous Cyclotron (ORIC) bombarded a uranium carbide (UC$_2$) target, inducing fission of the uranium. The fission fragments were transported to an electron-beam-plasma ion source (EBPIS) and were ionized [67]. The selected mass beam was filtered by the mass analyzing magnet ($\Delta M/M \approx 1/2500$). After traversing the charge-exchanger to make the beam of singly-charged negative ions and the isobar separation magnet ($\Delta M/M \approx 1/10000$ to $1/20000$), the beam was injected into the 25 MV tandem electrostatic accelerator where it was accelerated to 310 MeV. Finally, the ^{80}Ge beam was sent to the experimental station for the reaction study. Figure 3.2 shows a schematic of the beam production/delivery technique.
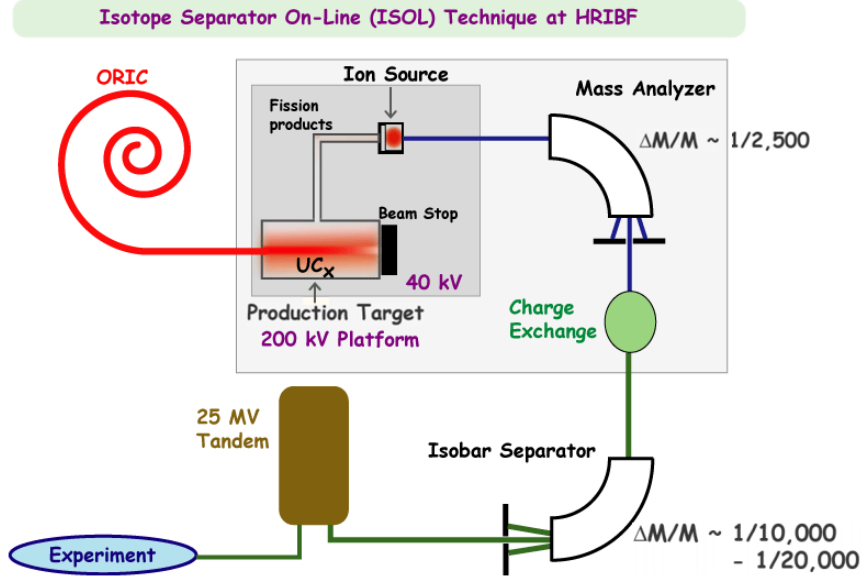
Figure 3.2: Beam production and delivery at HRIBF [13]

The UC_2 target was bombarded by the proton beam ($I_p = 16\ \mu A$ and $E_p = 50$ MeV) from ORIC. The target is chemically deposited on RVC fiber matrices to withstand high temperatures (2000°C). Scanning Electron Microscope (SEM) images of the UC_2 are shown in Figure 3.3.

In order to enhance the beam purity of ^{80}Ge, hydrogen sulfide (H_2S) gas was injected into the ion source transfer line. It has been shown that for some group IVA elements of the periodic table (e.g. Sn, Ge) transport of the isotope of interest as a sulfide molecule through the ion source enhances the relative isobaric purity of the beam [14]. ^{80}GeS$^+$ forms more readily than sulfide compounds of neighboring chemical groups, hence the purity of ^{80}Ge was enhanced from the mixture after they were filtered by the mass analyzing magnet being tuned to mass $A = 112$ (^{80}Ge and ^{32}S). The result of the beam purification will be described in Section 4.4. The ^{80}GeS$^+$ ions were then dissociated in the Cs-vapor charge-exchange cell to make singly-charged negative ions, ^{80}Ge$^-$.
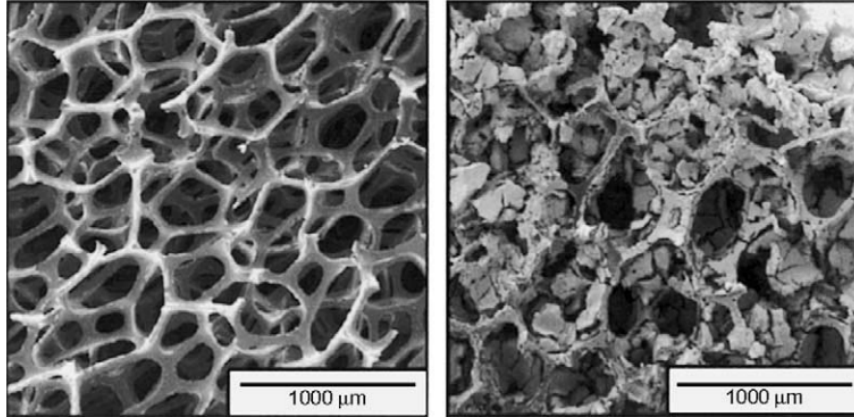
Figure 3.3: SEM photographs of a uranium carbide target. The left panel shows the uncoated carbon matrix and the right panel shows the target with the uranium carbide coating. [14]

The 25 MV tandem electrostatic accelerator is a folded-geometry device with excellent beam quality ($\Delta E/E = 1 \times 10^4$). The high-voltage generator, located inside a 100-ft-high, 33-ft-diameter pressure vessel has been built with both low- and high-energy acceleration tubes contained within the same column structure. The high terminal voltage is produced by mechanically transporting positive charge from ground. The accelerator is schematically drawn in Figure 3.4. The negative ions were accelerated through the low-energy tube and reached the positively-charged terminal. The ion beam passed through a carbon stripper foil at the terminal, which removes a number of electrons and leaves positively-charged ions. Finally, the beam was sent around a 180° bending magnet, re-accelerated down the high energy side of the tandem, and went through an energy-analyzing magnet and slits before delivery to the experimental room.

3.2   CD$_2$ Target Fabrication

The target used for this (d,p) reaction experiment was a thin foil of deuterated polyethylene (CD$_2$). The fabrication of CD$_2$ targets is outlined in Reference [68].

40
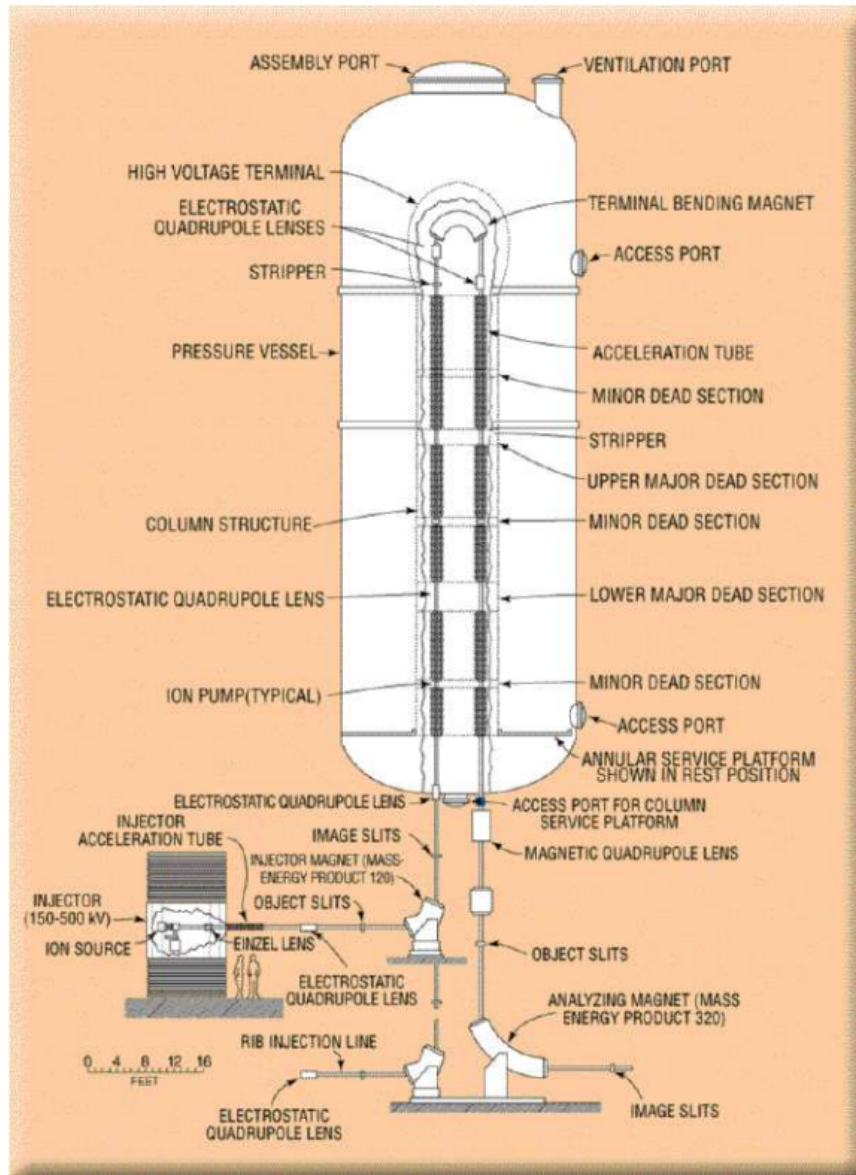
Figure 3.4: Side view of the 25 MV tandem electrostatic accelerator taken from Reference [15]. The beam enters from the rib injection line (left bottom) and exits the image slits (right bottom).
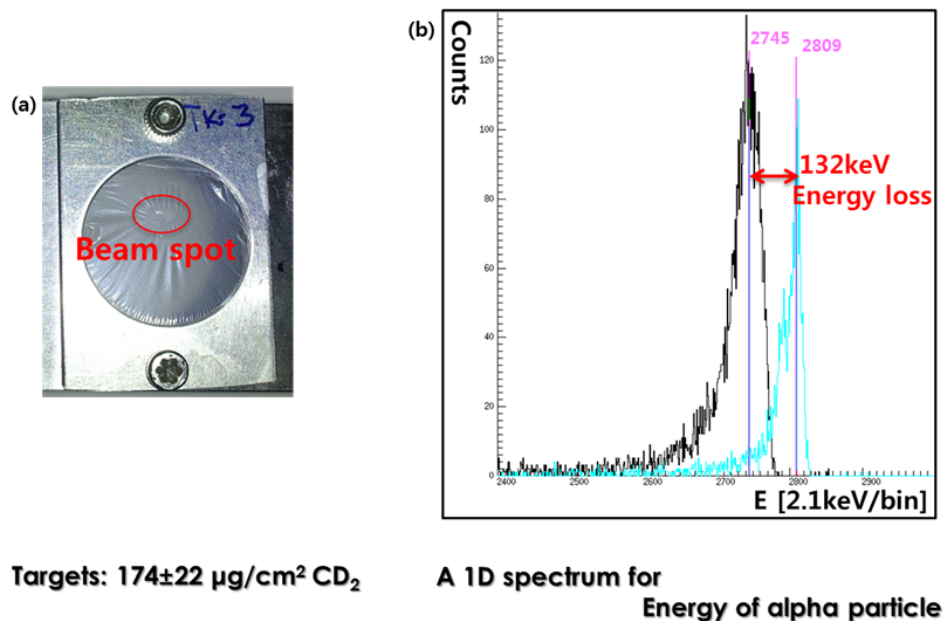
Figure 3.5: (a) A photograph of the CD_2 target used in this experiment. (b) A 1D spectrum for energy of α particles passing through with the target (left peak) and without the target (right peak). The thickness of the target can be calculated by the energy difference of these two peaks.

An advantage of the described method is that one can fabricate any desired thickness of the CD_2 target up to 2 mg/cm^2. A brief description of the target fabrication follows.

$(C_2D_4)_n$ powder, sold by Cambridge Isotope Laboratories, Inc., is dissolved in a solvent of p-xylene. The thickness of the foil is determined by the concentration of the powder in the solvent. The well mixed solution is boiled for $\sim$ 30 minutes at the boiling point temperature ($\sim$ 145°C) under a hood. After the powder is completely dissolved and the solution has cooled to about 125°C, the liquid is slowly poured on an empty glass slide. After the solvent has evaporated, the slide is slowly immersed in water until the foil floats free. A target frame is brought under the floating foil, lifted out of the water with the foil in place, and allowed to dry.

The thickness of the target can be verified by measuring the energy loss of energetic ions after passing through the target. For thin films, the energy loss is the product

of the specific energy loss, or stopping power, of the incident charged particle in the target and the target thickness:

$$\Delta E = -\frac{dE}{dx} \cdot \Delta x. \tag{3.1}$$

One can use a silicon detector to detect the known energy of α particles from a source and determine the energy loss which the particles experience while passing through the target. The stopping power, dE/dx of α particles in polyethylene is well known [69], leading to a simple determination of the target thickness, Δx. In this experiment, the thickness of the target was measured to be 174±22 μg/cm^2. A photograph of the target and a histogram of energy loss of α particle are shown in Figure 3.5.

3.3 Detectors

3.3.1 Silicon strip detectors

As explained in Section 2.3.1, the protons from the (d,p) reactions should be measured at backward laboratory angles since these correspond to forward center-of-mass angles where reaction calculations are most accurate. In order to achieve good energy and angular resolution along with large solid angle coverage, it is required that an array of position-sensitive or pixilated detectors are implemented at backward angles in the laboratory frame. In this experiment, several types of silicon semiconductor detectors were used; annular type, single/double sided non-resistive strips type and single/double sided resistive position sensitive strips type.

A silicon strip detector is a semiconductor and works as a n-type/p-type junction; a n-type semiconductor having a surplus of electron sites (called donors) and a p-type having a surplus of hole sites (called acceptors) [16]. When they are brought into contact, the donors can diffuse across the junction into the p-type material and combine with the acceptors. This results in creating the depletion region which is
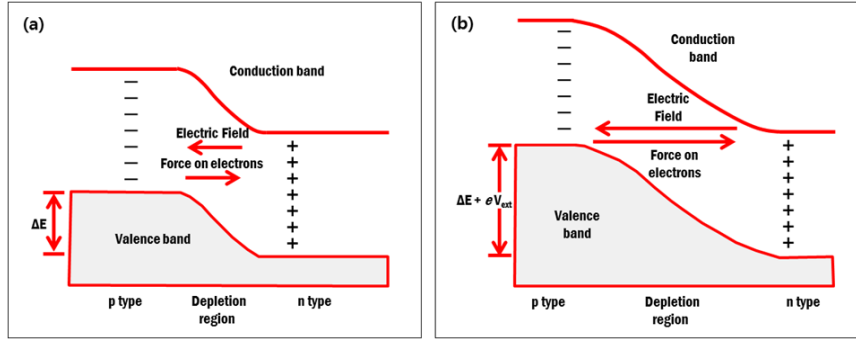
Figure 3.6: (a) p-n junction diode without bias. When n-type and p-type materials are brought into contact, the depletion region is created to allow charge particles ionize electrons, creating holes with their kinetic energy in the process. (b) p-n junction with reverse bias (a cathode connected to the n-type side). The depleted region becomes larger and the magnitude of the electric field increases with the reverse bias [16].
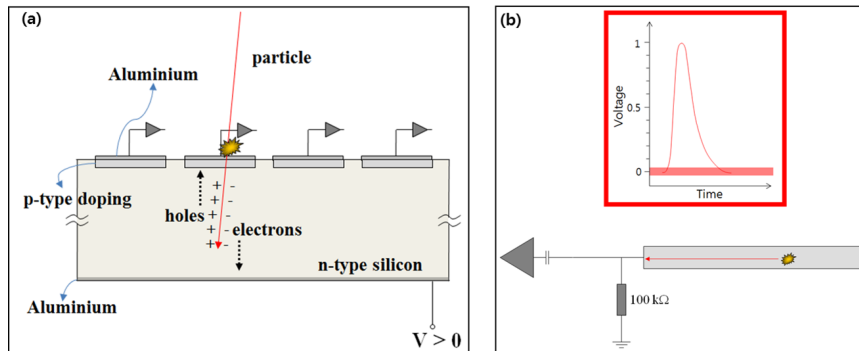
Figure 3.7: A diagram of non-resistive silicon strip detector (a) and a flow diagram of a signal coming out from the detector (b). The band in (b) represents the noise level. Figure (b) is taken from Reference [17].

an area where the charge carriers are neutralized, as shown in Figure 3.6. The space charge from the fixed sites creates an electric field which eventually halts further migration. By biasing with a positive voltage in n-type silicon, the magnitude of the electric field increases and the region becomes larger, resulting in more efficient charge collection and a larger sensitive volume of the detector. This depletion region is important, because as charged particles enter the region, they create electron-hole pairs and the total number of electrons/holes collected forms a charge pulse

44
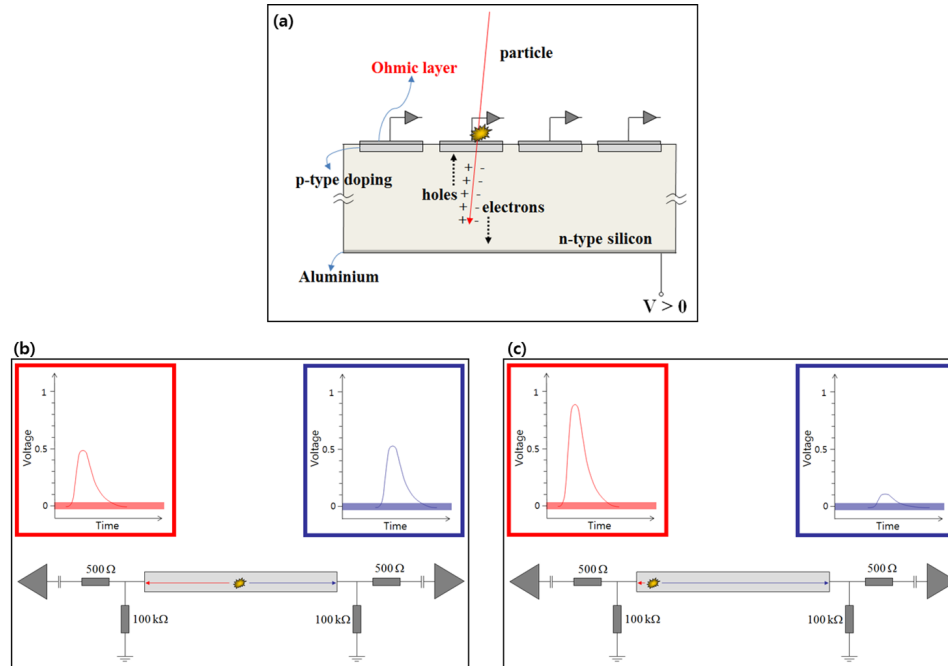
Figure 3.8: A diagram of resistive silicon strip detector (a). (b) and (c) show a flow diagram of signal coming out from the detector depending on the position where the particle hits. The bands represent the noise level. Figure (b) and (c) are taken from Reference [17].

which can be collected through a bond wire connected to one of the edges of the strips (Figure 3.7). The integrated charge of the pulse is proportional to the energy deposited by the particle. By recording the amount of charge collected and which electronics channel the current was observed in, it is possible to determine the energy of the charged particle and the position where it passed through the detector. An advantage of a silicon semiconductor detector lies in the small ionization energy of the electron-hole pair. Only 3.6 eV is required to create the electron-hole pair compared to, for instance, gas-filled detectors where 30 eV is typically needed. Thus, the statistical fluctuations are reduced and the signal to noise ratio improves considerably resulting in the resolution of the detector being better.

A resistive strip silicon detector consists of n-type silicon and a thin resistive p-type silicon junction layer implanted on top of the n-type silicon. The electrons liberated
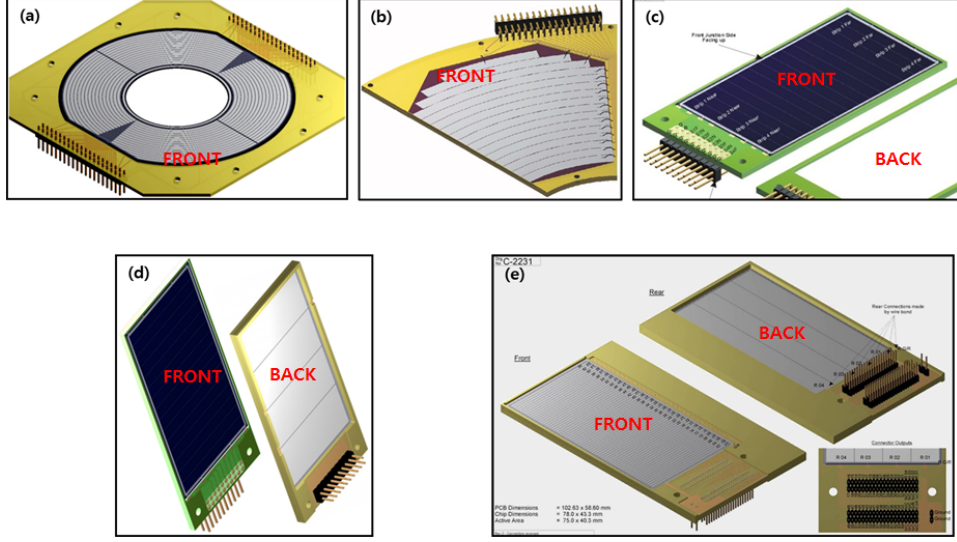
Figure 3.9: Design of S1 detector (a), YY1 detector (b), X3 detector (c), Super X3 detector (d) and BB15 detector (e)

by electron-hole pairs in the depletion region arrive at the resistive strips to induce a signal in the readout strips by capacitive coupling (Figure 3.8 (a)). Figure 3.8 (b) shows that a particle hitting the center of a strip has its charge divided into two signals and equal signals are read from either end. When the particle hits the position closer to the left end, the signal on the left end has to be larger than the one from the right end as the amount of charge collected is inversely proportional to the resistance from the creation position to the readout end (Figure 3.8 (c)). As two charge collections (Q_L and Q_R) for one strip are measured, the total charge Q_t and position x can be determined as

$$Q_t = Q_L + Q_R, \tag{3.2}$$

$$x = \frac{Q_L}{Q_t}. \tag{3.3}$$

The position x is related to the fractional position of the strip, where the particle hits. When x is zero, it means the particle hits the right end of the strip. And, $x = 1$ means the particle hits the left end of the strip.

Table 3.1: Geometric and operating parameters for the MSL-type YY1 wedge silicon detector [1].

No. of junction elements:	16 p-type in front side
No. of ohmic elements:	1 n-type in back side
Strip width:	5.0 mm
Active inner radius:	50 mm
Active outer radius:	130 mm
Active area:	29 cm^2
Thickness:	$100 \approx 500~\mu$m
PCB ϕ range:	45 deg
Depletion voltage:	30 V typ, 50 V max

MINI is a small annular detector array which is a 300 μm thick non-resistive S1 detector with 4 quadrants of 16 rings subtending radii from 2.4 to 4.8 cm with 1.5 mm strip pitch (Figure 3.9 (a)). The MINI detector was placed upstream of the target and behind the SIDAR array, covering $\theta_{lab} \sim 150°$ - $170°$ ($\theta_{C.M.} \sim 11°$ - $4°$).

SIDAR consists of 8 wedges with 300 μm thick non-resistive YY1 style detectors having 16 annular strips per wedge of 8 cm radial length ($r_{inner} = 5$ cm and $r_{outer} = 13$ cm). Figure 3.9 (b) and Figure 3.10 (a) show the design of the YY1 detector and the array, respectively. It offers high granularity, excellent energy resolution, and good resolution in position, angle, and timing. In this experiment, SIDAR covered $\theta_{lab} \sim 128°$ - $154°$ ($\theta_{C.M.} \sim 24°$ - $11°$) with the flat annular configuration. Table 3.1 summarizes geometrical and operational characteristics for an individual wedge.

The ORRUBA array consists of two rings of X3 style position sensitive silicon-strip detectors, as shown in Figure 3.10 (b), designed to operate typically with one ring forward and one backward of $\theta_{LAB} = 90°$ [65]. The X3 style detectors have an active area of 7.5 × 4 cm and are divided into 4 resistive strips of 7.5 × 1 cm, with readout from both ends of each strip, for position and energy determination (Figure 3.9 (c)). In this experiment, one X3 style detector was placed at the laboratory forward angle.

The X3 style detector provides a large solid angle coverage with a small number of electronics channels (only 8 channels per detector) thanks the position
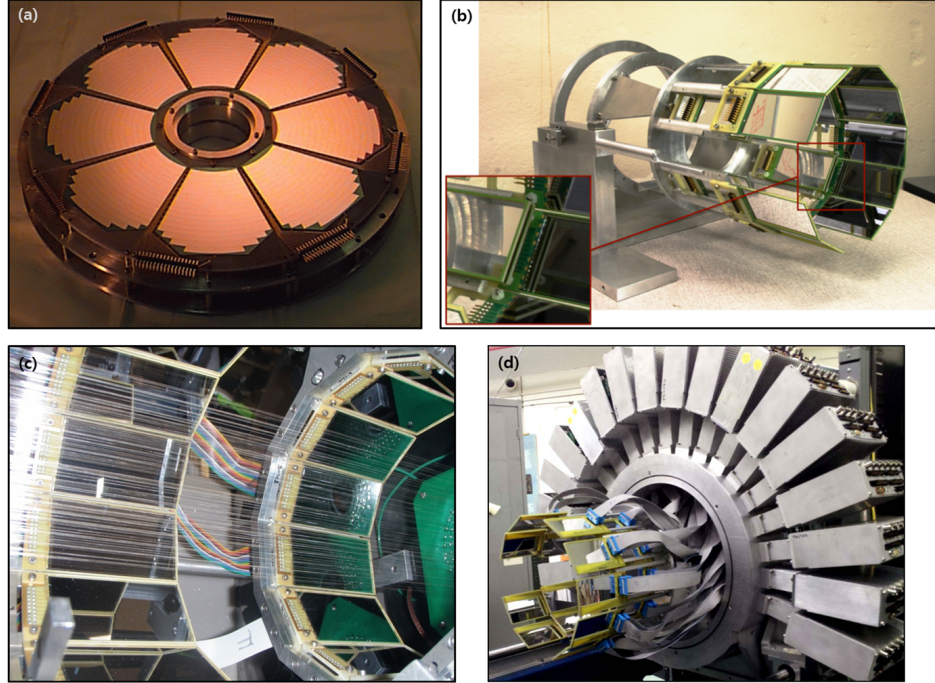
Figure 3.10: Picture of detector arrays. (a) A flat annular configuration of SIDAR, (b) ORRUBA, (c) ANASEN and (d) SuperORRUBA

determination via resistive charge division. This resistive property, however, results in different rise-times of the signal pulses for different positions at which the particle hits. This results in an apparent reduction in gain towards the center of the strip for amplifiers with fixed shaping times ($\sim 1~\mu$s). Thus, a position-dependent gain correction has to be made during the data analysis. Details of the correction are described in Section 4.1.2. Another complication of the resistive layer is that the effective strip length depends on the energy of the particle due to the electronics ignoring signals below a fixed threshold. This energy-dependent detection efficiency can complicate the analysis. To alleviate these weaknesses, the Super X3 style detector of the ANASEN array and the BB15 style detector of the SuperORRUBA array have been developed.

The ANASEN array consists of 3 rings of 12 Super X3 style position sensitive silicon-strip detectors (Figure. 3.10 (c)) [62]. An illustration of the Super X3 style

detector is shown in Figure 3.9 (d). The detector front side is divided into 4 resistive strips, which is similar to the X3 style detector. In the Super X3 style detector, however, additional mask sets were added to segment the rear (ohmic) face of the detector into four non-resistive segments oriented perpendicularly to the resistive strips on the front face of the detector. This results in two improvements. By taking the full energy from the rear face, good energy resolution ($\sim$ 30 keV in Full Width Half Maximum (FWHM)) is achieved and the full range of the effective strip length is available without sensitivity to the electronic threshold. Unfortunately, we could not use these benefits in this experiment because the signal of the back side strips could not be converted to the shaping output in the conventional shaping amplifier due to the opposite (negative) polarity to the front strip signals (positive). So, X3 and Super X3 were used in the same way. In this experiment, four Super X3s were installed in purpose of detector commissioning (two at the backward angle and two at the forward angle in laboratory system).

Finally, the SuperORRUBA array has a similar geometry to the ORRUBA array except for a small modification of the radius of the detector mounting frame and the feedthrough doughnut (Figure 3.10 (d)) [63]. However, the X3 style detector in the ORRUBA array has been replaced by a non-resistive double sided silicon detector (called BB15 style), which was divided into 64 horizontal strips of 1.2 mm width on the front side and 4 longitudinal strips on the back. Figure 3.9 (e) shows the design of the detector. These thin 64 non-resistive strips result in a good position resolution and energy resolution at the expense of large increases in the amount of required electronics channels. The energy resolution of the detector was measured to be about 30 keV FWHM for a high gain preamp (60 mV/MeV). Because conventional electronics are typically restricted to low channel count ($\sim$ 512 channels), $\sim$ 2000 channels for the SuperORRUBA array required, in turn, a new scheme for signal digitization. The ASICs system was implemented for this and is explained in Section 3.4.2.

3.3.2 Ionization counter

The ionization counter (IC) served as three purposes during the experiment. First, the IC was used to identify the atomic number of the beam particles. Although the ISOL beam production process has many steps to purify the radioactive ion beams from the fission of uranium (see Section 3.1), the beams are still contaminated with unwanted beam species due to the small mass differences between wanted and unwanted isotopes. These contaminants will induce reactions with the target material with similar reaction kinematics as the isotope of interest. Therefore, it is necessary to be able to confirm that the beams are highly purified or to distinguish the transfer reactions caused by specific nuclei.

The second purpose was to measure the intensity of the beam as well as the integrated flux. In order to determine the differential cross section, $d\sigma/d\Omega$, of the reaction of interest, the total amount of beam particles incident on target, N_{in}, must be known, as shown in Equation 2.48. By placing the counter downstream of the target, such that all beam particles and recoils are counted and the total beam amount, N_{in}, can be identified.

The third benefit of the counter was to use its signal as a timing reference to clean the spectra of interest. Since the time difference between a silicon detector hit and an IC hit for all real events should be similar, random coincidence data can be rejected by gating on the time window of interest. More details are explained in Section 4.3.

A simple schematic of an ionization counter is shown in Figure 3.11. As a particle enters the gas-filled chamber, it loses energy due to collisions with the gas, and the gas is ionized in this process. The resultant ions drift to the cathode and electrons move to the anode. As mentioned in Section 3.3.1, the electrons create a charge pulse, and its integral is proportional to the energy deposited by the particle. Since the voltage between two plates and the distance of the plates determines the drift time of the liberated charge (and thus the maximum counting rate), various geometries of many plates can increase the beam count rate limit.
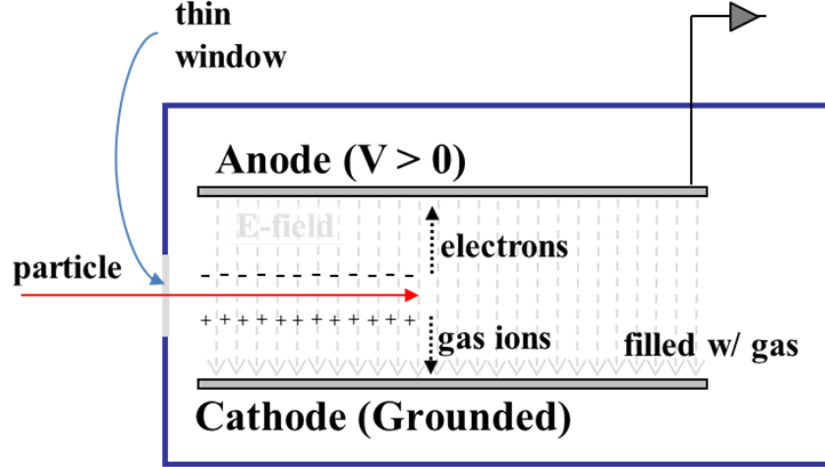
Figure 3.11: A schematic diagram of a simple ionization counter, showing drift of the ions/electrons. Electrons typically drift 1000 times faster than positive ions due to their much smaller mass. [16]

In addition, a double cathode-anode plates configuration (shown in Fig. 3.12) can be used as a ΔE-E particle telescope. As a particle passes through the first region of the capacitor, it loses some energy (ΔE) and enters a second region where the rest of the energy (E)is deposited. The energy loss (also known as stopping power) is described by the Bethe formula as

$$-\frac{dE}{dx} = \frac{4\pi e^4 z^2}{m_0 v^2} NZ \left[\ln \frac{2m_0 v^2}{I} - \ln(1 - \frac{v^2}{c^2}) - \frac{v^2}{c^2} \right] \tag{3.4}$$

where v are ze are the velocity and charge of the primary particle, N and Z are the number density and atomic number of the absorber atoms, m_0 is the electron rest mass, I is the average excitation and ionization potential of the absorber, and e is the electronic charge [70]. For nonrelativistic charged particles ($v \ll c$), the stopping power varies as z^2/v^2 since the other factors in the above expression vary slowly with particle energy or species of the incident particle. A measurement of ΔE and E, therefore, determines the value of mz^2, and different atomic species can be distinguished by this measurement.
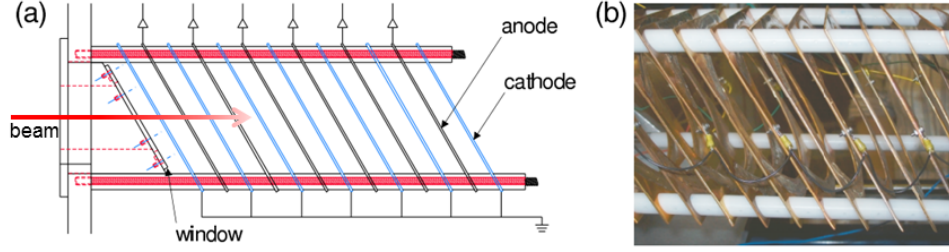
Figure 1: (Color online) (a) The cross-sectional view of the fast ionization chamber, and (b) the picture of the electrodes assembled in the chamber are shown in the figure.

Figure 3.12: Adopted figure from Reference [12]. The electrodes are made of copper and gold coated thin tungsten wires are glued to the frames in 2 mm spacing. The entrance window is also tilted with the same angle of the electrodes.

In this experiment, in order to increase the maximum counting rate, a new fast ionization counter, developed recently in ORNL, was installed (Figure 3.12) [12]. The design of the counter was based upon the tilted electrode gas ionization chamber model at RIKEN [71]. Anodes and cathodes are alternately placed in 0.72 inch steps back-to-back. Since the distance between the electrodes in this geometry is short, the drift time of electrons and ions is reduced, which allows for higher counting rates. The counter can count a beam rate up to half million particles per second as a maximum. Since beams pass through the grid, some beam particles stop at the grid resulting in small blobs in the ΔE-E spectrum. The transmission rate through one electrode is about 98%. Currently, a maximum of 8 anodes and 9 cathodes can be placed in the counter. The chamber was filled with tetrafluromethane (CF_4), which allows for a fast electron drift velocity. The pressure of the gas was ~ 90 torr of CF_4, and operating voltages were 100 ± 2 V on the anodes. The first 5 anode signals were combined and used for the ΔE signal, and the combination of the other 3 anode signals were used for the E signal for the beam identification.
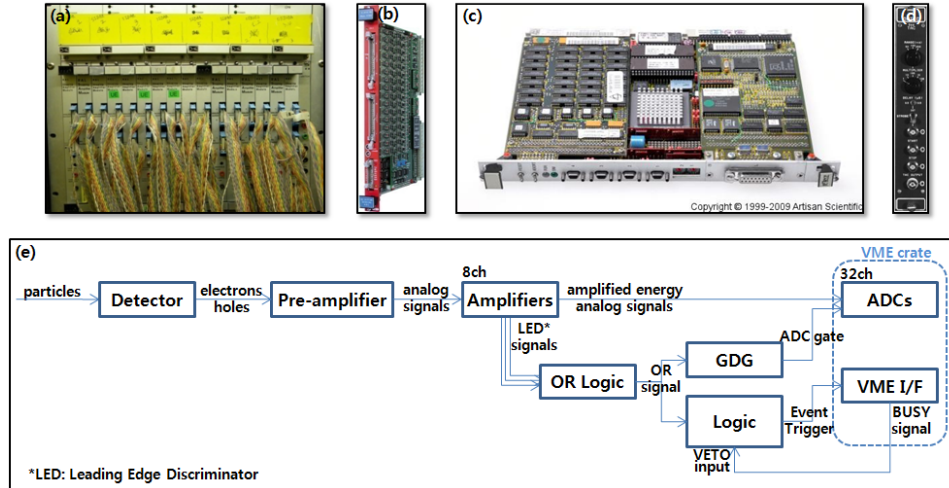
Figure 3.13: Conventional electronic modules for ORNL DAQ. (a) RAL Shaping amplifier, (b) CAEN ADC, (c) SYS-640C VME I/F, (d) ORTEC TAC. Communication map of conventional setup has been drawn in (e). The number on top of each module indicates how many channels a single module can manage.

3.4 Electronics

In order to digitize the analog signals and save this information to the computer, signal processing is required such as amplification, timing, and data acquisition (DAQ). Section 3.4.1 will describe the analog devices in detail. Signals from the MINI, the SIDAR, the X3 detectors, the Super X3 detectors and the ionization counter were analyzed and stored in the conventional electronics system, while the new ASICs electronics system was used for analog signals from the BB15 detectors and the ionization counter. The new system will be discussed in Section 3.4.2.

3.4.1 Conventional electronics setup

A communication diagram of the conventional setup is shown in Figure 3.13 (e). Analog signals from the detector are converted from current pulses to voltage pulses by charge-sensitive pre-amplifiers (CSAs). Since the voltage from the module is at most a few hundred mV, further amplification and shaping is performed using 8-channel

53

shaping amplifiers (shapers) and discriminators developed by Rutherford Appleton Laboratory (RAL, Figure 3.13 (a)). Peak sensing 32-channel VME analog-to-digital converters (ADCs, Figure 3.13 (b)) manufactured by CAEN are used to digitize peak heights of the amplified signals coming from the RAL module. Leading-edge trigger signals from the RAL modules are used to time stamp the original signal and signify the existence of an event. The trigger signals are combined in a logical OR logic unit such that one single event signal is used to trigger the ADC gate, the event trigger and the input of the time-to-amplitude converter (TAC, Figure 3.13 (d)). When the VME interface (I/F) module receives the event trigger, it reads the digitized data in the CAEN ADC and outputs a BUSY signal so no more event triggers are generated until it completes the reading.

Protons from (d,p) events are detected in the silicon detectors in coincidence with forward going recoils, which are detected by the ionization counter. The time between events in the silicon detectors and the ionization counter was measured on an event-by-event basis to determine if events were of interest as signified by having a true coincidence between the two detectors. A time-to-amplitude converter (TAC) module was used for this purpose. The TAC module has two input signals: "start" and "stop", and one output generating a pulse with an amplitude proportional to the time difference between the two inputs. The TAC output was then read by an ADC module. For time-correlated events, the TAC spectrum shows a peak corresponding to the correlated time difference. The TAC inputs in this experiment were a start signal from a silicon detector hit and a stop signal from ~ 4 μs delayed ionization counter event. More details about the TAC data will be described in Section 4.3.

3.4.2 ASICs setup

Increasing the channel count requires fundamental changes and a new signal processing method. Most of the independent functional modules in the conventional electronics have to be merged into one small chip using Application Specific Integrated
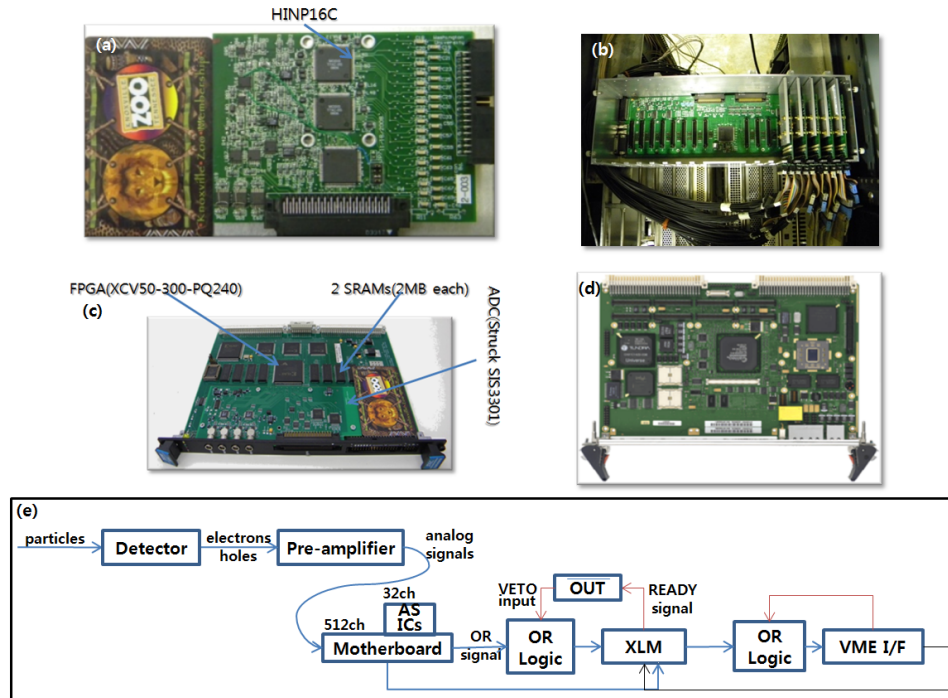
Figure 3.14: A new ORNL DAQ system using ASICs. (a) ASICs chip board next to a regular credit card to compare size of the chip board. ASICs chip, HINP16C manage 16 channels and two chips are implemented in one chip board. (b) A motherboard holding 5 chip boards. One motherboard can handle 16 chip boards corresponding to 512 channels. (c) JTEC XLMXXV includes FPGA to control motherboards and chip boards, ADC to read voltages from the ASICs chip boards, and 16 MByte of memory to store digitized data by ADC. (d) A new VME I/F module, Motorola MVME5500 to handle the XLMXXV and take data from the module. A communication map of ASICs setup has been drawn in (e). The number on top of the module indicates how many channels a single module can manage.

Circuits (ASICs). Therefore, the new ASICs device can hold a large number of channels with a great reduction of the cost and space to implement the readout electronics [72].

These ASICs chips were developed by collaborators at Washington University - St. Louis. One single chip can handle 16 channels and two chips are implemented in one ASICs board [73]. This ASICs chip includes CSAs, shapers, positive/negative peak detectors and constant fraction discriminators (CFDs) as the main functions. Events including detector ID, strip number, digitized bit of the energy and timing

Table 3.2: Differences between NSCL DAQ system and ORNL DAQ system. All applications are necessary to be developed in the new DAQ system.

Differences	NSCL DAQ	ORNL DAQ
Language	C++ and TCL	C and Fortran
Comm. Module	PCI to VME Adapter (SBS Bit3)	Single Board VME Computer (MVME5500)
Comm. Cable	Optical Fiber Cable	Ethernet Cable (RJ45)
DAQ Software	spectrodaq, nscldaq, spectcl and root	pacman, pacor, scanor and damm
ASICs Controlling Software	CHIP	Reset, LoadFPGA, InitCHIP and SetCHIP
Trigger	CAEN V262 I/O Module	ORNL Trigger (V-WRAP-A110)
Operating System	Debian Linux	Redhat Linux and RTEMS

triggers are output. The HiRA group in Michigan State University has been used this ASICs system implemented into National Superconducting Cyclotron Laboratory (NSCL) DAQ system for several years and achieved successful results for many experiments [72].

The peak of the shaped energy signal in the chip is sampled by the peak detector, converted to differential and connected to the ADCs of the XLMXXV on 110-Ω shielded twisted-pair digital audio cables with LEMO 2-contact connectors. The ADCs measure the difference of the voltages in the two pins (one for the signal peak and another for the offset) and record it in the memory.

The XLMXXV universal logic VME module (XLM) works as a control center. DAQ commands and initial setup parameters can be loaded onto the ASIC's motherboard and the ASIC board through the XLM module. By the sequence of the DAQ, the XLM module commands the ADC to save digitized data into eight 2 MByte SRAMs and triggers the computer to read these data. It is powerful because the XLM includes a field-programmable gate array (FPGA), which is flexible for modifications as needed. As shown in Figure 3.14 (d), the XLM has an ADC board on the mezzanine floor to digitize the energy and time signal peak heights from the motherboard.

Figure 3.15: Chip Commander V3.0 (Graphic User Interface to load setup parameters)

Since all of these new devices were not implemented in the ORNL DAQ system previously, it was a challenge to make them work properly in the system. The NSCL DAQ system utilized a completely different DAQ logic compared to the ORNL DAQ system. During the implementation project, therefore, the author had to understand how the devices were implemented into the NSCL DAQ system and how the data is taken with the ASICs devices. Furthermore, one had to find the best solution to accomplish the ASICs implementation in ORNL DAQ system. The table of differences between the NSCL DAQ system and the ORNL DAQ system in terms of the ASICs implementation has been listed in Table 3.2. The ASICs system in ORNL DAQ has been utilized in studies of the ^{10}Be$(p,p)^{10}$Be, ^{26}Al$(d,p)^{27}$Al [74], ^{80}Ge$(d,p)^{81}$Ge (the present work), ^{126}Sn$(d,p)^{127}$Sn, ^{128}Sn$(d,p)^{129}$Sn [75], and ^{132}Sn$(d, t)^{131}$Sn reactions in inverse kinematics at the HRIBF. The following paragraphs describe the communication of the ORNL DAQ system with the ASICs system to save data into the computer.

57
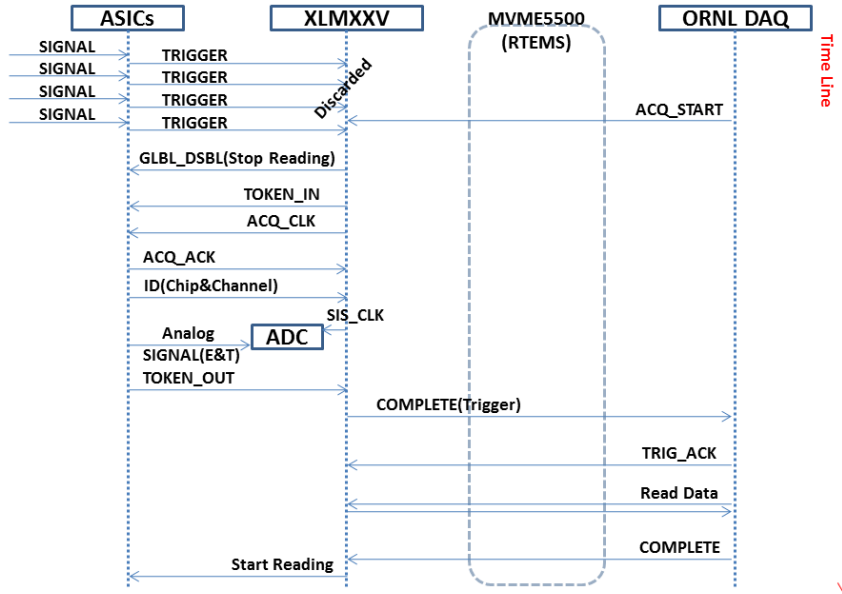
Figure 3.16: A communication flow diagram of the ASICs system connected to the ORNL DAQ.

The VME I/F module, the Motorola MVME5500, was used in the new system to support communication with the XLMXXV module. Since the VME I/F is a single board computer run by Real Time Operating System (RTEMS) based on embedded Linux, it supports the communication through UDP or TCP/IP protocols. Thus all the ASICs control software communicates with VME via Ethernet. The codes for the booting procedure of the VME I/F module and ORNL DAQ server programs were modified in order to assign the VME address of the XLMXXV module to the PCI address of the VME I/F and to initialize the XLMXXV modules. In addition, ASICs/XLMXXV control programs such as LoadFPGA, InitChip, SetChip as well as the graphic user interface for this SetChip program (Figure 3.15) were developed.

Figure 3.16 shows how to communicate among ASICs, XLMXXV and VME I/F during the data acquisition in the ORNL DAQ system. The ASICs chip, XLMXXV and VME I/F communicate to each other with many logic signals such as clock signals, acknowledge signals, trigger signals and clear signals. The VME I/F enables the XLMXXV to start recognizing OR signals from the ASICs chip, and the XLMXXV

commands the ASICs chip to send channel IDs, energies and times to the XLMXXV. The ADC digitizes signal peak heights and saves peak values into the memory. Then, the XLMXXV sends the triggers to VME I/F to read the saved data. Once a buffer in the VME I/F is filled up with the data, then all data will be sent to the computer and stored in the local file. This diagram is one cycle of one event in one channel and becomes more complicated as more events and more channels are added.

Since the ASICs system has been recently developed and in use for experiments, the ASICs system manual included in Appendix A is written to help and guide users how to setup the system (hardware and software) and how to take data with it.

Chapter 4

Data Analysis

For a particular event, the types of data obtained are the detector number, the strip number and the peak voltage obtained by the analog signal. From these pieces of information, angle of detection and kinetic energy of the particle can be determined. Several steps are required in order to calibrate the energies and angles of the detected particles, to transform experimentally observed values to the center-of-mass system, to reject unwanted contaminant events, and to determine cross section values from the observed number of counts. This chapter will describe these steps for each detector type: SIDAR, Super X3 detectors and BB15 detectors. Data from the MINI detector were not analyzed because of an excess background due to the close proximity of the detector to the beam axis and target entrance apertures. Even without this detector, statistics were high enough in the other detectors to understand and calibrate the reaction of interest.
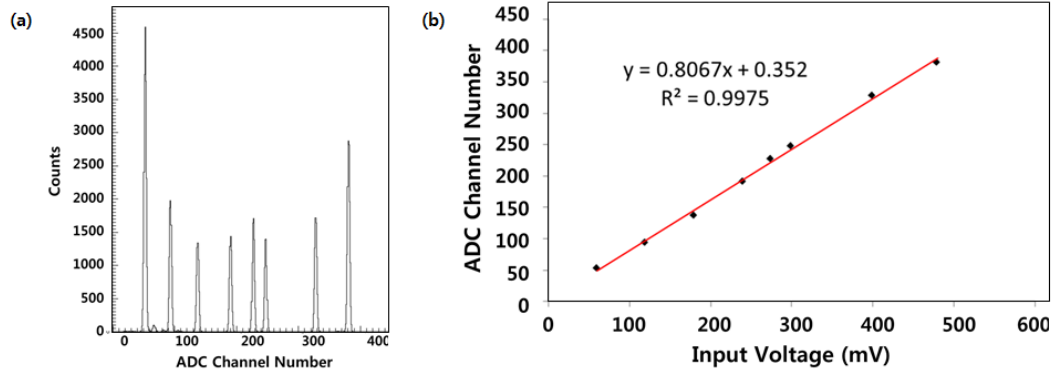
Figure 4.1: (a) "Matchstick" spectrum for one strip in SIDAR. Each peak represents a different output voltage from the pulser. (b) A fitted response function for the output channels. The measured offset in this channel was 0.352 in ADC channels. Offsets of all SIDAR channels are found close to zero using the conventional electronics setup.

4.1 Energy and Angle Calibration

4.1.1 SIDAR in conventional electronics

Pulser Calibration and Gain Matching

Most electronics such as CSAs and ADCs have their own offsets to process signals in an efficient way, so an offset calibration of each electronics channel is necessary to correct for any such offset and non-linearities inherent from the first electronics device to the last one. This can be done by applying different test signals from an electric pulser to the electronics system and then measuring the digital response. In this experiment, a pulser signal was plugged into a 'test' input of the CSAs and the output voltage was measured by the ADCs for each strip of the detector. A sample result of this measurement is shown in Figure 4.1 (a). Fitting the centroids of these peaks and plotting the measured ADC channel number against the known input voltage for each peak (Figure 4.1 (b)) enabled the response of the electronics system to be determined. No significant non-linearity was observed in all channels of SIDAR, and so the offsets could be obtained using linear least squares fits. It was found that,
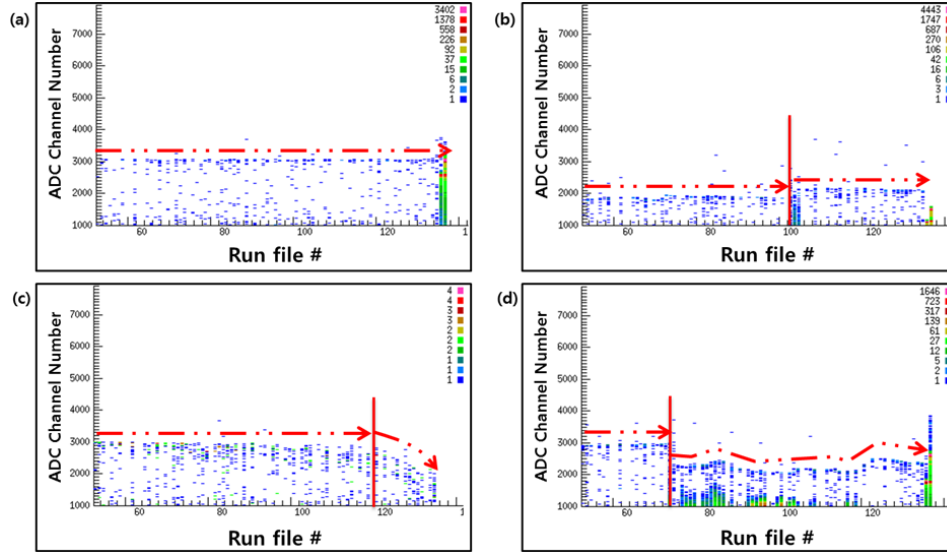
Figure 4.2: Sample 2D spectrum having electric gains changed over time. The horizontal line corresponds to the constant energy of the α-particle from ^{244}Cm. (a) No gain change in time. (b) Gains moved up at some point. (c) Gains moved down at some point. (d) Gains were bouncing over time

however, offset subtraction in the conventional electronics system was not necessary because the offsets of the channels were very close to zero and the uncertainty of the measurement was larger then the variation of the offset.

The energy calibration of the silicon strip detector is usually carried out using α particles from a radioactive source such as ^{244}Cm or ^{248}Cf. A ^{244}Cm source was used in this experiment. The energies of α particles coming from the decay of ^{244}Cm are 5.805 MeV (branching ratio of 76%) and 5.763 MeV (branching ratio of 24%). Using the previously measured electronics offset, the gain of each detector strip was extracted. The gain is simply the linear conversion from energy to ADC channel number. Once all of the strips are calibrated, there should be no position dependence on the energy measured for the alpha particles, resulting in a straight horizontal line for the energy of α particles in an energy versus strip or position spectrum.

It is best if the energy calibration data can be taken at least twice (before the experiment and after the experiment) to confirm that the energy gain has not changed
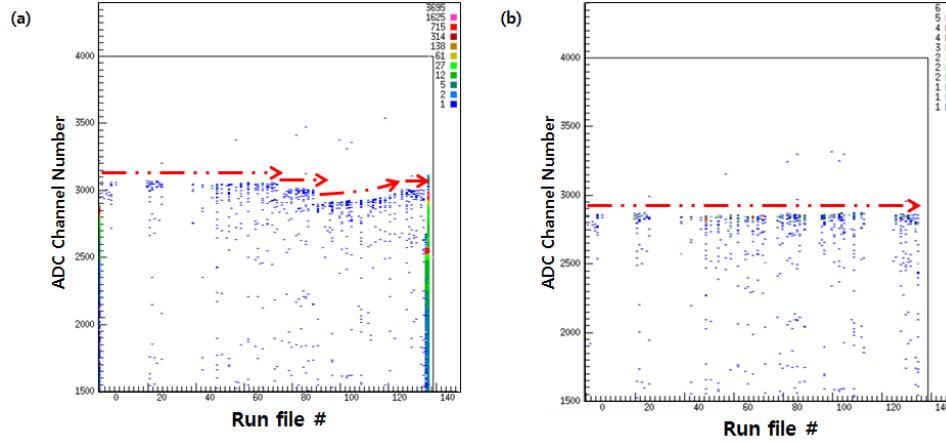
Figure 4.3: For each gain change, an individual gain coefficient was applied to the run. (a) ADC Channel Number over the run file number before the gain matching. (b) The same spectrum after the gain matching.

with time. Sometimes small amounts of ^{244}Cm contamination in the chamber are evident during the experiment without any source due to the long exposure of the source in the target chamber. This has the advantage that one can check whether the energy gains were constant over time by examining 2D spectra of ADC channel number versus run file number (corresponding to time).

Unfortunately, it was found that there were surprisingly large gain shifts in many SIDAR detector channels and the assumption of a constant gain coefficient could not be used in the experiment. The gain shift is obvious by looking at the 2D spectra shown in Figure 4.2. This behavior had not been previously observed and provided a real challenge in that all of the strips had different behaviors and each run for any strip had to be recalibrated. A possible source of this effect can be a high power consumption in the conventional electronics resulting in the gain shift in the shaping amplifiers over time. A sample corrected spectrum is shown in Figure 4.3.

After all of the energy calibration for all strips, the resolution of the α particle peak was measured to 80 keV FWHM at 5.8 MeV. This is comparable to the intrinsic resolution of the single detector which is 50 keV FWHM at 5.8 MeV but somewhat worse owing to the variability of the gain.

Table 4.1: Angular coverage for SIDAR strips (in flat mode)

Strip No.	θ_{btm} - θ_{top} (degree)	ϕ range (degree)
1	153.8 - 151.6	42.0
2	151.6 - 149.4	42.0
3	149.4 - 147.4	42.0
4	147.4 - 145.4	42.0
5	145.4 - 143.6	42.0
6	143.6 - 141.8	42.0
7	141.8 - 140.1	42.0
8	140.1 - 138.5	42.0
9	138.5 - 136.9	42.0
10	136.9 - 135.5	42.0
11	135.5 - 134.1	42.0
12	134.1 - 132.7	42.0
13	132.7 - 131.5	42.0
14	131.5 - 130.3	36.0
15	130.3 - 129.1	28.0
16	129.1 - 128.0	18.0

Angle Conversion

The laboratory angle of a given detector strip can be calculated from the geometry of the detector setup. Because the flat configuration of the SIDAR is installed perpendicular to the beam axis, the polar angle can be calculated using:

$$\theta_{btm} = 180 - \tan^{-1}\left(\frac{(n-1) \times w + y}{x}\right), \tag{4.1}$$

$$\theta_{top} = 180 - \tan^{-1}\left(\frac{n \times w + y}{x}\right), \tag{4.2}$$

where θ_{btm} is the angle for the bottom of the strip, θ_{top} is the angle of the top of the strip, n is the strip number ($n = 1$ to 16), x is the distance along the beam axis between the target and the detector, y is the distance from the beam axis to the bottom of the first strip and w is the width of the strip (strip pitch). In this experiment, x was 102±3 mm, y was 50±1 mm and w was 5±1 mm. The polar angle coverage of the SIDAR array was from 128±1° to 154±1°. For the azimuthal angle,
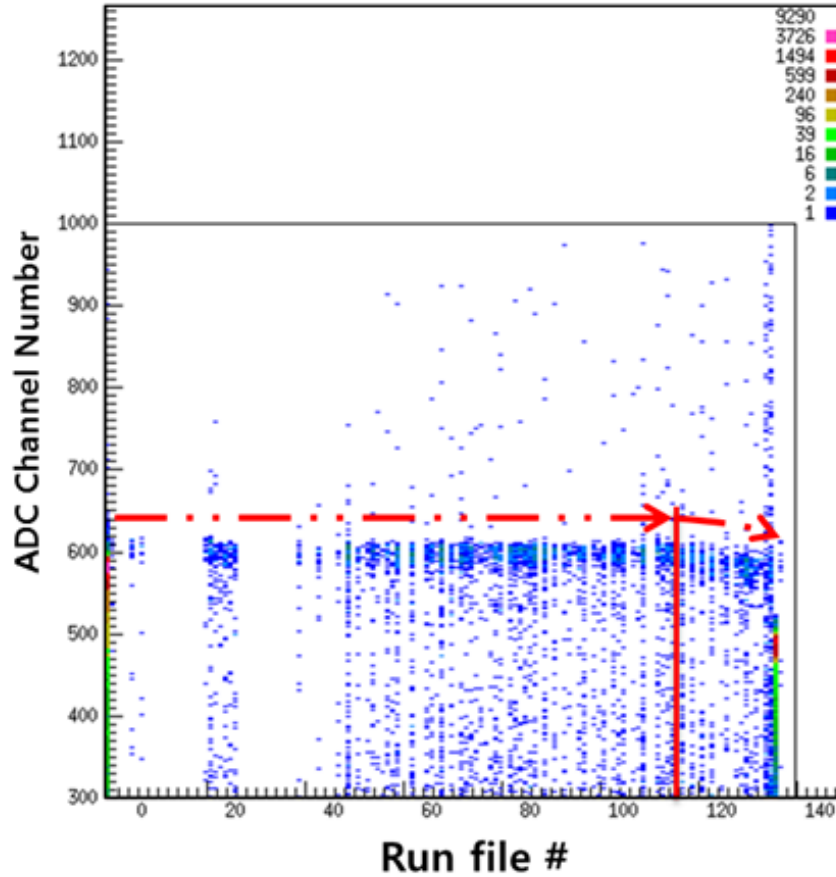
Figure 4.4: A 2D plot showing energy over the time for a sample strip. Fortunately, only a small fraction of the runs in all of the Super X3 detector channels was found that the gain changed.

the angle of the strip depends on the design of strips in the detector because the array was placed coaxially to the beam axis. Table 4.1 summarizes the angular range for each strip in the detector.

4.1.2 Super X3 detectors in conventional electronics

Pulser Calibration and Gain Matching

The offsets in Super X3 detectors were also set to zero for the reason described in Section 4.1.3. The energy gain change in the detector also existed but all strips
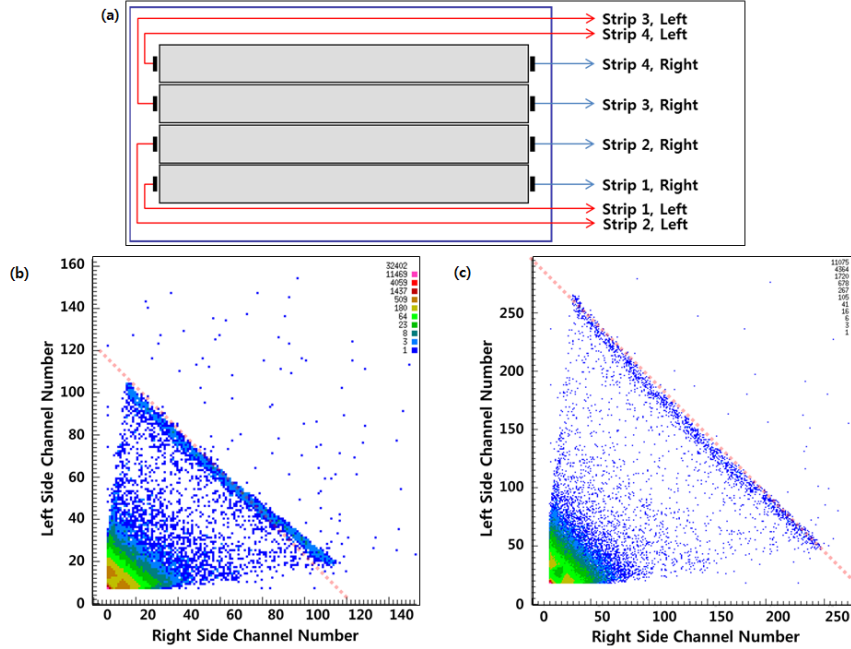
Figure 4.5: (a) A schematic diagram of the front side of Super X3 detector. A 2D spectrum of the left channel of the strip versus right channel of the strip before the energy calibration (b) and after the calibration (c). Red dotted lines in (b) and (c) are reference lines indicating that the calibration works well.

behaved similarly; the gain sagged near the end of the experiment. In order to simplify the corrections and preserve the resolution, those data exhibiting large gain shifts were rejected in the data analysis. Figure 4.4 shows the energy gain trend in a sample strip of the detector.

Because one resistive strip of the detector is connected to two electronic channels (left and right shown in Figure 4.5 (a)), the energy calibration has to be performed with two channels at the same time. A 2D spectrum of the raw left versus raw right signals can be made for each strip to show the α-line with a ^{244}Cm source. The extended line of the α-line must intercept at 5.8 MeV (or corresponding ADC channel number), which is the energy of the α particle, on x-axis and y-axis after the calibration, because the addition of left side and right side has to be 5.8 MeV. Figure 4.5 (b) and (c) shows a sample plot for one of the strips before and after the energy calibration, respectively.

66
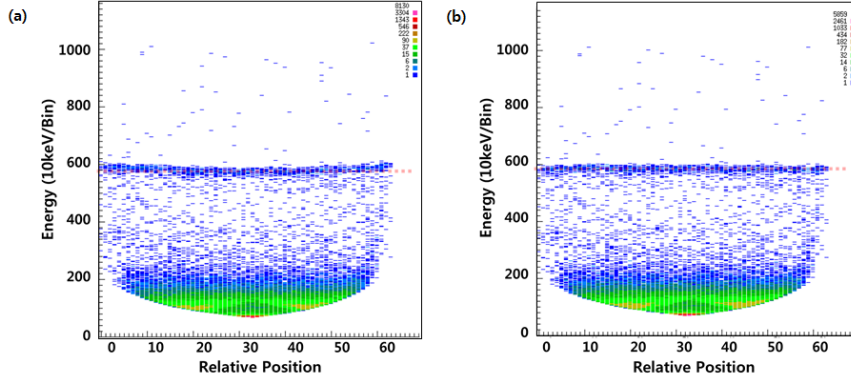
Figure 4.6: (a) A sample 2D spectrum of energy versus position in Super X3 detector. The value of relative position is scaled to 64 for convenience. The α-line shows a slight position dependence of the gain. (b) shows the same spectrum after the correction. The red dotted line is a reference line indicating that the calibration works.

Position Calibration

As mentioned in Section 3.3.1, a relative position where the particle hits in a detector strip can be calculated by Eq. 3.3. As shown in Figure 4.6 (a), the α-line in the Super X3 detector showed a parabolic shape due to the position dependence of the gain. This could be corrected when an energy function of position for the curved line was found and a ratio between the known energy of the α particle, which is 5.8 MeV in this case, and the measured energy of the particle. Figure 4.6 (b) shows the spectrum after the correction.

Once all of the calibrations and corrections were finished, the resolution of all the Super X3 detectors was measured to be 160 keV FWHM at 5.8 MeV energy which was comparable to the resolution of the single strip of the detector (100 keV FWHM at 5.8 MeV). A peak of the α particle is shown in Figure 4.7.

The Super X3 detectors were installed parallel to the beam axis. Coverage angles of Super X3 detectors are listed in Table 4.2.
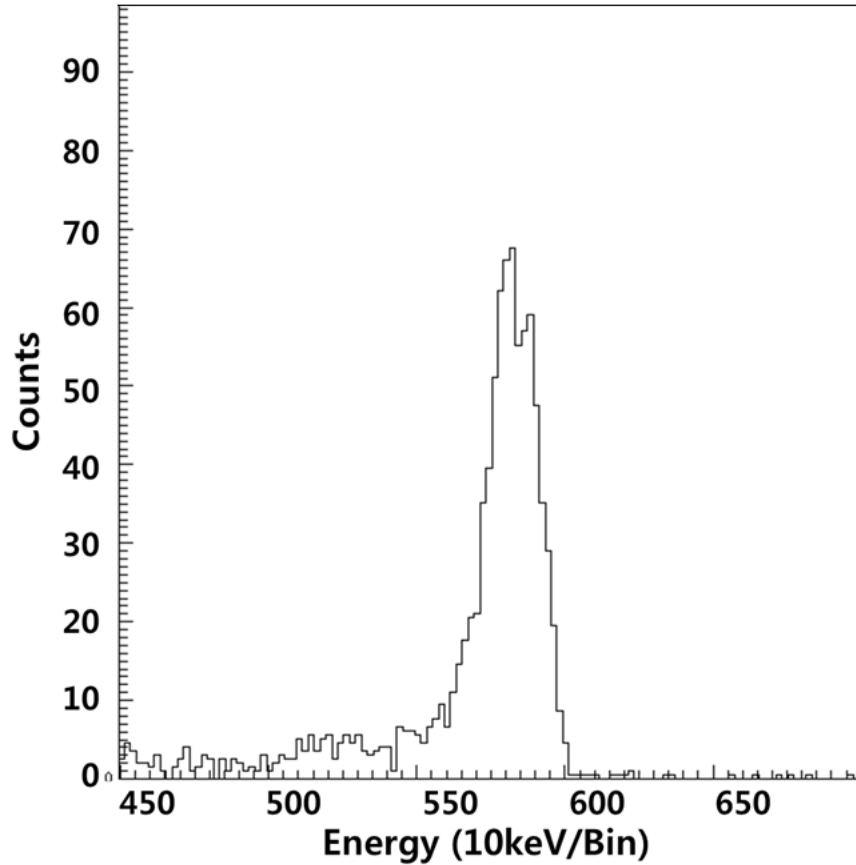
Figure 4.7: The energy calibration spectrum summed over all of Super X3 strips for 5.8 MeV α-particles.

4.1.3 BB15 detectors in ASICs electronics

Pulser Calibration and Gain Matching

The electronics offsets for the BB15 detectors were determined in a similar fashion to the SIDAR detectors described above. The offsets in the ASICs electronics channels, however, were very far from zero and they had to be taken into account; they ranged from -193 to 385 in ADC channels. The difference was due to the different type of ADC used with the ASICs system. A sample spectrum of the pulser calibration is shown in Figure 4.8.
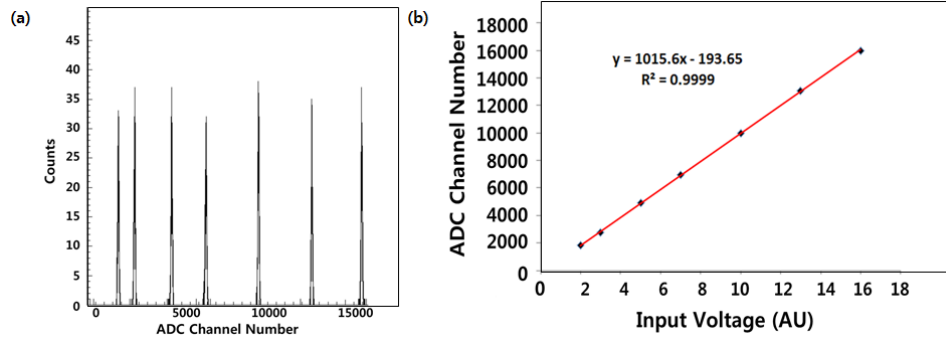
Figure 4.8: (a) "Matchstick" spectrum for one channel of a BB15 detector. Each peak represents a different output voltage from the pulser. (b) A fitted Response function for the output channels. It shows the offset of this channel was -193.65 in ADC channels. Most of the offsets were found far from zero and had to be considered for the calibration work.

None of the unexpected gain shifts with respect to time were observed with the ASICs electronics. Thus, one constant energy gain coefficient for each channel could be applied for all of the runs. Since these detectors do not use resistive charge division, a correction for gain sag near the middle of the detector was not needed. Once all of the calibrations were finished, the resolution of all of the BB15 detectors was measured to be 54 keV FWHM at 5.8 MeV energy. This resolution was comparable to the intrinsic resolution of the detector, 30 keV FWHM, and it was enough to identify states of the nucleus in the experiment.

The setup of the BB15 detectors was very similar to the Super X3 detectors. However, the design of strip orientation in the detector was changed from vertical to

Table 4.2: Angular coverage in Super X3 detector

Strip No.	Forward angle (degree)		Backward angle (degree)	
	θ range	ϕ range	θ range	ϕ range
1 and 4	50.3 - 89.3	6±1	91.8 - 124.0	5±1
2 and 3	50.0 - 89.3	6±1	91.8 - 124.2	6±1

69

horizontal and this affected to the strip-angle conversion equation. Coverage angles of BB15 detectors are listed in Table 4.3.

4.2   Energy Loss Corrections in the Target

Because of the finite thickness of the target, corrections for the energy loss of the beam in the target and for the exiting protons from the target are required. Such corrections are made under the assumption that the reactions are occurring at the center of the target. The energy loss in the target was calculated using a code called STOPIT, which is used to calculate energy loss for any solid/gaseous material for any given beam, beam energy, and thickness of the material. For particles coming out of the target, an energy loss function of the initial energy and the thickness, $f(t, E)$, was found to be:

$$f(t(\theta), E) = t(\theta) \times a \times E^b \tag{4.3}$$

where a and b are constants for a certain ion and target (e.g. a proton and CD_2 target in this case), E is the energy of the particle, $t(\theta)$ is the thickness of the target for a certain angle θ. Figure 4.9 shows a 2D spectrum of the energy versus laboratory angle after the energy loss correction for all detectors.

Table 4.3: Angular coverage for the BB15 detectors

Strip No.	Forward angle (degree)		Backward angle (degree)	
	θ range	ϕ range	θ range	ϕ range
1 - 64	50.4 - 89.2	25±1	92.1 - 124.4	20±1
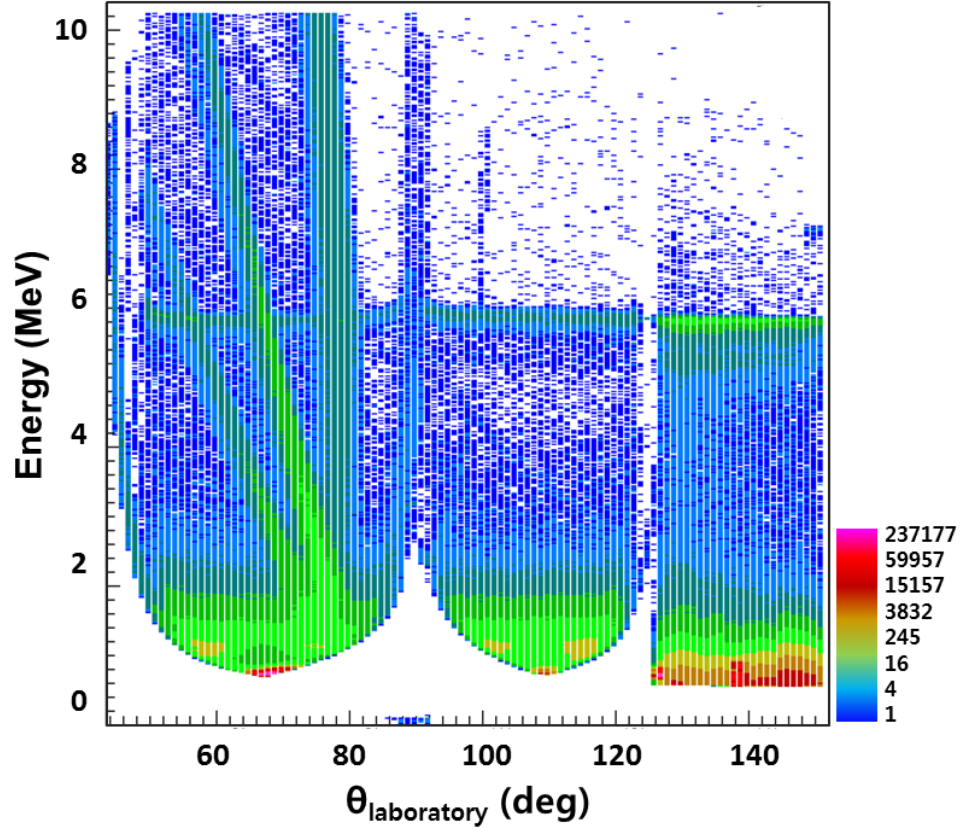
Figure 4.9: A 2D energy vs. angle spectrum for ^{80}Ge$(d,p)^{81}$Ge after the energy loss correction

4.3 Identification of Coincident Events

As mentioned in Section 3.4.1, the events of interest can be better identified by requiring a proper time coincidence. True coincident events are tightly correlated in time (Figure 4.10 (a)), and thus, for time-correlated events, the TAC spectrum will show a peak corresponding to the correlated time difference as shown in Figure 4.10 (b). A delay (~ 4 μs) was added to the stop signal to bring the TAC pulse amplitude above the detection threshold. The timing window for proton-recoil coincidences was set to be 50 μs wide. By requiring a good TAC (200 ns width), the amount of random coincidences was reduced by 1/250 (= 200 ns / 50000 ns).

71
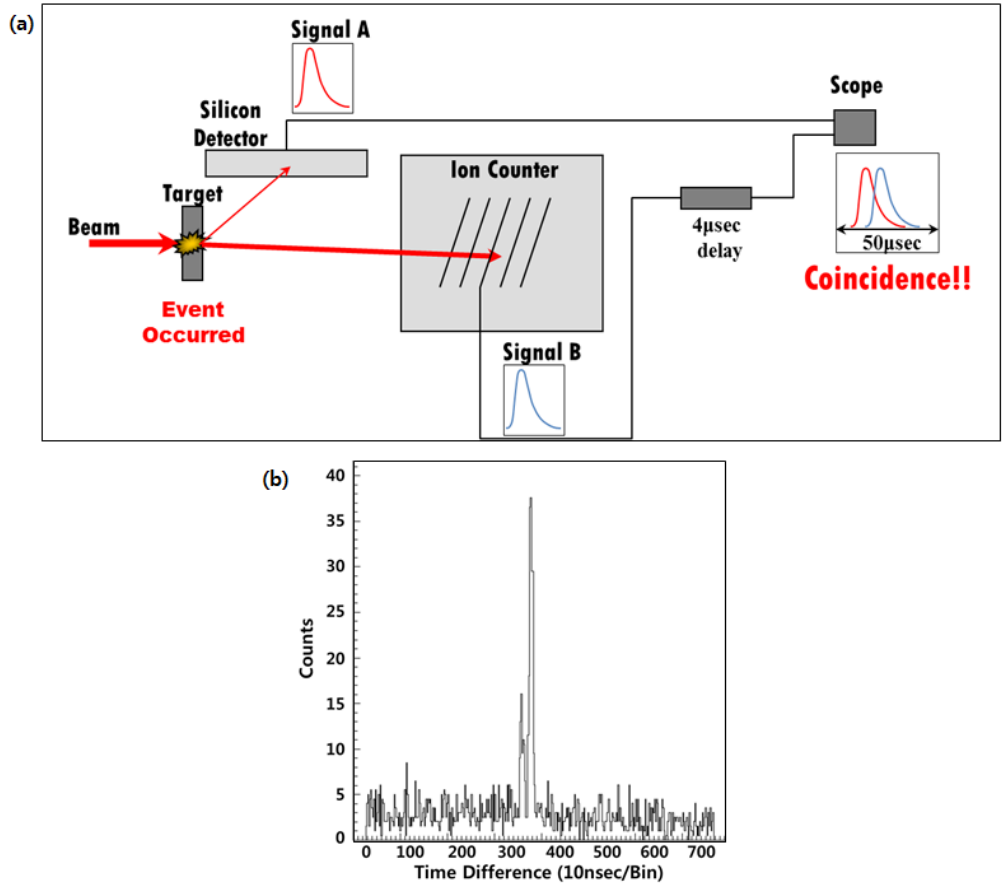
Figure 4.10: A schematic diagram showing the coincident events between silicon detectors and an ionization counter in (a). (b) shows 1D spectrum of the time difference for this experiment. A peak measured to be 3.79±0.4 μs with 87 ns FWHM resolution. There are two peaks shown because the TAC set up changed during the experiment.

A 2D spectrum of the proton energy versus laboratory angle before and after TAC gating is shown in Figure 4.11. The amount of random coincident data was greatly reduced by imposing the TAC gate, and strong proton lines from the (d,p) reaction are clearly visible in the spectrum.
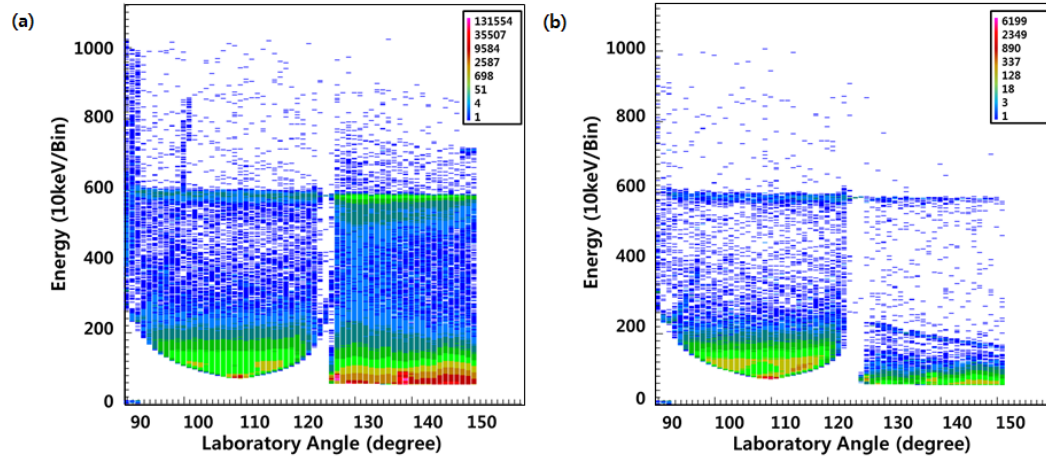
Figure 4.11: A 2D spectrum before (a) and after (b) gating on the TAC. Real events were filtered by the TAC peak and most sources of noise and contamination were removed.

4.4 Beam Particle Identification

Beam purity and beam intensity are calculated from the ionization counter data. Figure 4.12 shows the energy deposited by the $A = 80$ beam species in the first five anodes of the counter, ΔE, as a function of the total energy by the summation of the ΔE and the energy deposited in the rest of the anodes, E. The spectrum clearly shows the main components of the beam. The presented species were stable ^{80}Se (3%) and the radioactive ^{80}Ge (97%) required for the measurement. The beam intensity reached up to 1.7×10^5 pps with an average of 1.2×10^5 pps, read by the ionization counter scaler, during the experiment.

4.5 Beam Current Determination

Measuring the total flux of beam that impinged on the target is an important step towards determining the differential cross sections from the observed proton yields of each state as shown in the Eq. 2.48. The absolute differential cross section is in turn

73
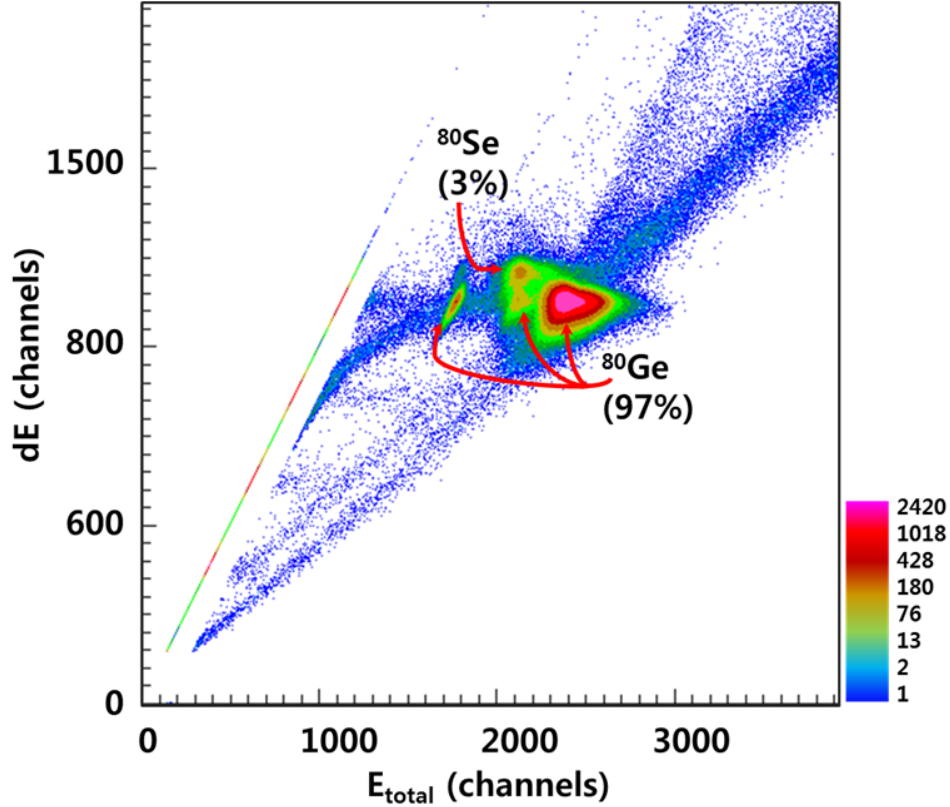
Figure 4.12: A ΔE vs. E_{total} spectrum from the ionization counter. There are small spots shown along the same ΔE value in the spectrum, corresponding to the stopped beams at the first five anodes because of the anodes geometry.

used to extract spectroscopic factors $S_A^B(lj)$ in Eq. 2.47, by comparing to theoretical differential cross sections.

In this measurement there were two independent methods of beam flux determination; one was to find the total beam flux (N_{in} in Eq. 2.48) from the ionization counter data and use the measured target thickness (corresponding to n in Eq. 2.48), and the other was to find the normalization factor N_s (= the total beam flux $\times$ the number of particles in the target; $n \times N_{in}$ in Eq. 2.48) from the elastic scattering data. In the first method, the integrated beam current could be measured in the two-dimensional gate in the ionization counter E vs. E_{total} spectrum. The large ADC window setup
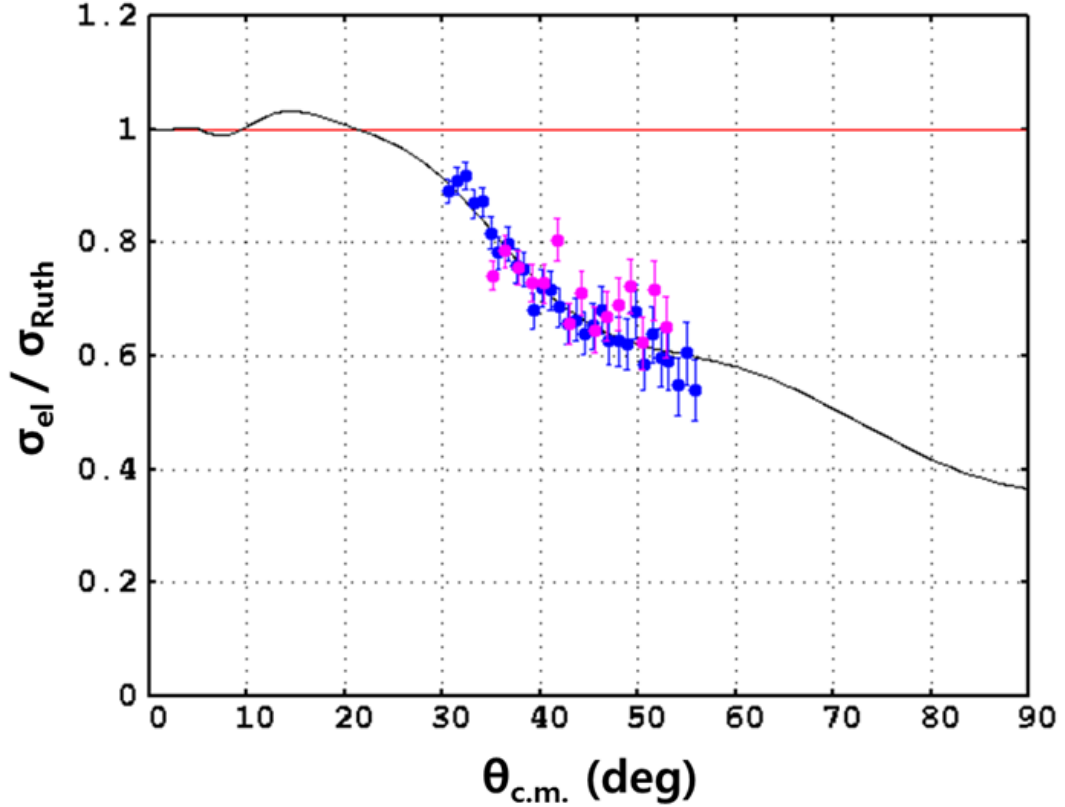
Figure 4.13: Ratio of measured data to the Rutherford differential cross section. The data are scaled to the elastic scattering calculation (black curve). Blue dots shows the data from the Super X3 detectors and purple dots are from the BB15 detector. The fit was confined to data with $\theta_{\text{c.m.}} < 54°$ as shown.

(60μs instead of 6μs), however, resulted in pile-up of recoil/unreacted beam in the spectrum, and the total count in the spectrum was not reliable.

Instead, the normalization factor, N_s was found using the elastic scattering data. Since scattering differential cross sections are reasonably well understood, the observed amount of elastically-scattered target constituents can be used to determine N_s. All of the variables in the Eq. 2.48 can be measured and calculated except the normalization factor N_s ($= n \times N_{in}$) and this factor can be found by fitting data to the calculated elastic scattering differential cross section. A similar technique was used in multiple previous cross section measurements [26, 76].

75

Deuterons from the ^{80}Ge(d,d) reaction were identified and counted as a function of center-of-mass angle. Energy loss corrections in the target were made for both the beam and the emitted particles from the reactions. Polar angular resolutions were typically better than 2 degrees. Solid angles were calculated from the geometry of the detector, and transformed to the center-of-mass reference frame. The calculation of the differential cross section was performed by the code FRESCO [77] for the elastic scattering including the nuclear potential. Optical model potentials for the deuteron incoming wave were taken from Lohr-Haeberli global potentials [52]. The data was then fitted to the calculated curve to find the normalization factor as shown in Figure 4.13. Since the differential cross section of the data fell off quickly from pure Rutherford scattering over the annular range covered, the scattering includes nuclear elastic scattering. Thus, the differential cross sections calculated with the FRESCO including nuclear scattering had to be used to fit the data. The estimated uncertainty in normalization is 10%.

4.6   Internal Calibration with ^{80}Se(d,p)^{81}Se Data

Because previous measurements of the ^{80}Se(d,p)^{81}Se reaction have been made, it was informative to compare the results using the current setup with the previous measurements to help quantify systematic uncertainties. Montestruque *et al.*, measured the ^{80}Se(d,p)^{81}Se reaction in normal kinematics and observed excitations up to 4.16 MeV [3]. In this experiment, ^{80}Se(d,p)^{81}Se reaction data were taken with the same setup by switching beams to ^{80}Se from the facility stable injector. The strong proton band in Figure 4.14 corresponds to an isolated triplet of states at E_x = 1053 keV, 1234 keV and 1303 keV with $J^\pi = \frac{5}{2}^+$, $\frac{1}{2}^+$ and $\frac{5}{2}^+$ (see Figure 4.15) [3].

It should be noted that there were more backgrounds shown in Figure 4.14 than the one of the ^{80}Ge(d,p) case. Because we wanted to perform this calibration quickly due to the limited beam time, a higher beam current was used than with the ^{80}Ge beam. This precluded us from being able to detect the beam with the IC and thus
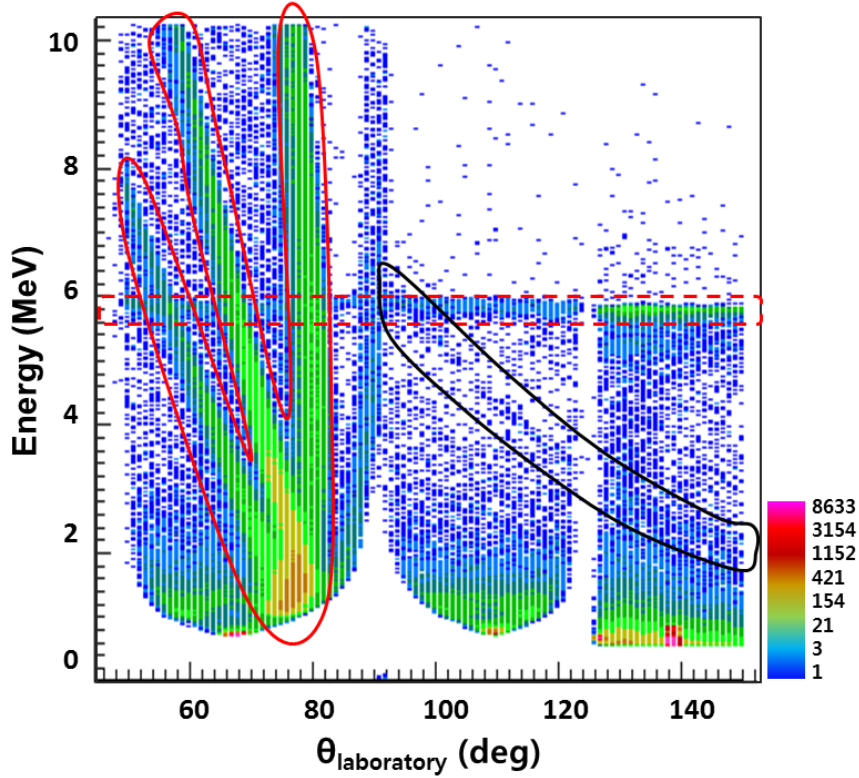
Figure 4.14: A 2D spectrum of energy versus laboratory angle for the ^{80}Se$(d,p)^{81}$Se reaction in inverse kinematics. A strong proton band in black solid line area was used for an internal calibration with the previous measurement [3]. The horizontal band (red dashed line area) at 5.8 MeV arises from a ^{244}Cm calibration source. Three fingers in the red solid line area are protons, deuterons and carbon nuclei (from left to right) from the elastic scattering.

the random coincidences could not be reduced. The backgrounds, however, were subtracted before the Q-value conversion step in order to count real events correctly.

It was not possible for these three states to be resolved in the present measurement due to the experiment resolution, so the peak was fitted by one centroid of Gaussian form. Using the well-known energies of these states, the experimental energy calibration was improved by matching the observed spectrum to these energies. Figure 4.16 shows the sum of the Q-value over all strips from the ^{80}Se$(d,p)^{81}$Se reaction in inverse kinematics, and the solid line is a Gaussian fit with a centroid at $Q = 3.26\pm0.06$ MeV and a resolution of 260 keV FWHM, corresponding to E_x
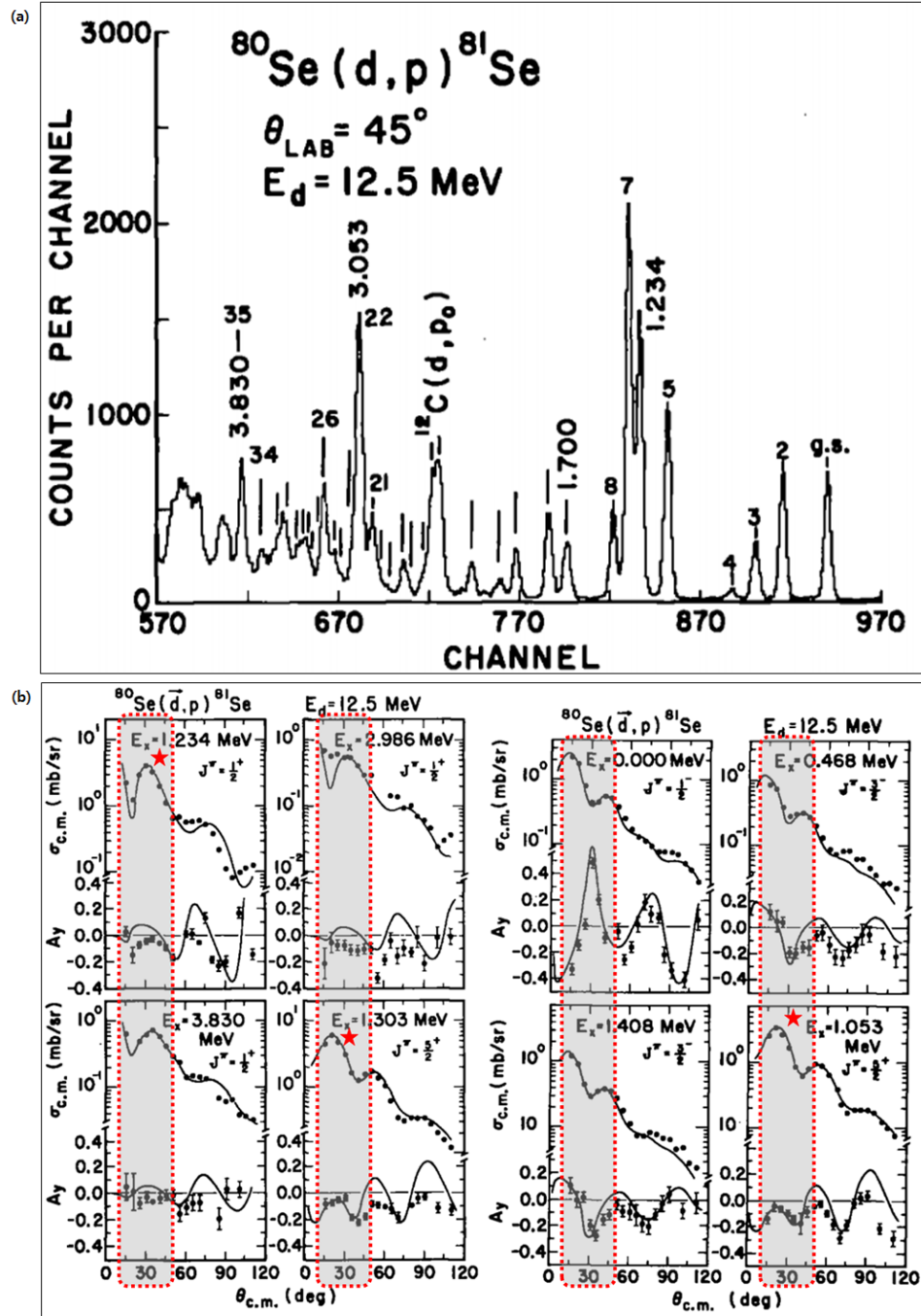
Figure 4.15: *Q*-value spectrum of ^{80}Se(*d,p*)^{81}Se reaction in normal kinematics at 45 degree laboratory angle (a) and angular distributions for each *Q*-value peak (b). The angular range shaded by red dashed rectangles in (b) is the one covered in the present measurement. It is evident that peaks labeled 5, 1.234 and 7 in (a) show strong differential cross section in the range (marked by red stars in (b)) and they are expected to be observed in the present measurement. Figure taken from Reference [3].

78
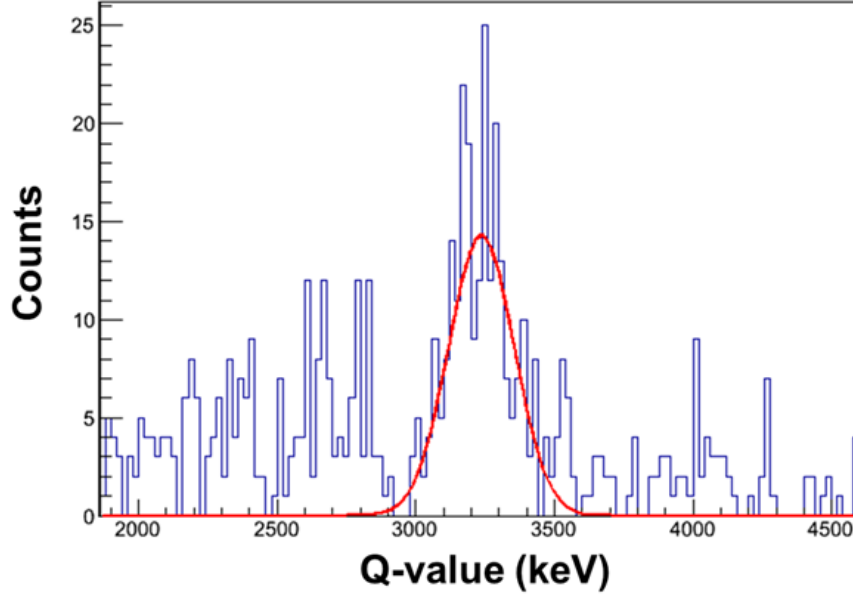
Figure 4.16: Q-value spectrum of ^{80}Se$(d,p)^{81}$Se in inverse kinematics, summed over all angles. The solid line is the fit of the three states at $E_x = 1053$ keV, 1234 keV and 1303 keV. The ground-state Q-value of the reaction is $Q = 4476$ keV [3].

$= 1.22 \pm 0.06$ MeV. This energy resolution is consistent with expectations considering target thickness and angular resolution effects.

Similar to the work mentioned in Section 4.5, the normalization factor, N_s, of the ^{80}Se beam could also be calculated using the elastic scattering data from the ^{80}Se(d,d) reaction. Figure 4.17(a) shows the ratio of measured cross sections scaled by N_s over the theoretical calculation using the code FRESCO [77]. The selected angular range for the fit was 25° - 55° for Super X3 detectors and 38° - 56° for BB15 detectors in order to optimize the fit with the calculation. Once the normalization factor was found, it was applied to Eq. 2.48 and the experimental differential cross section was calculated. Figure 4.17(b) shows the data overlaid with the DWBA calculation which is the mixed differential cross section with the one of three states weighted by the measured spectroscopic factor in the previous paper. Spectroscopic factors of these three states were $S_{lj} = 0.195, 0.45, 0.332$ for $E_x = 1054$ keV, 1234 keV and 1303 keV, respectively, from Reference [3]. The corresponding observed spectroscopic factors in
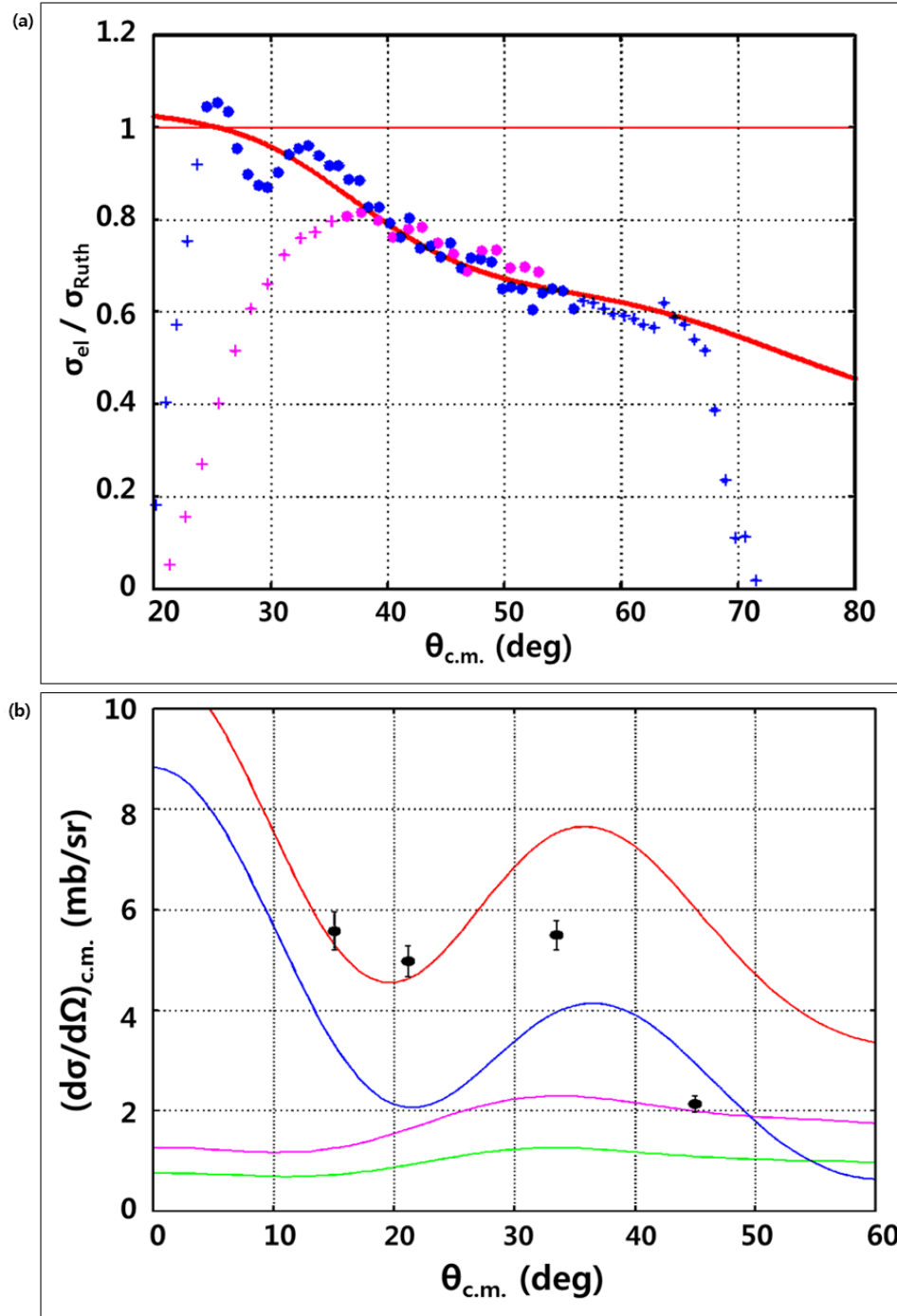
Figure 4.17: Angular distribution plots for ^{80}Se(d,d) in (a) and ^{80}Se(d,p) in (b). Blue data points in (a) are from Super X3 detectors and purple are from BB15 detector. A straight horizontal line at $\sigma_{el}/\sigma_{Ruth} = 1$ is drawn for reference and the brown curve shows the elastic calculation using the code FRESCO. The red curve in (b) represents a mixture of the three expected states ($E_x = 1054$ keV (blue), 1234 keV (purple) and 1303 keV (green)), which could not be resolved in this experiment due to the detector resolution. Agreement in the graph (b) implies the beam normalization method was reasonable.
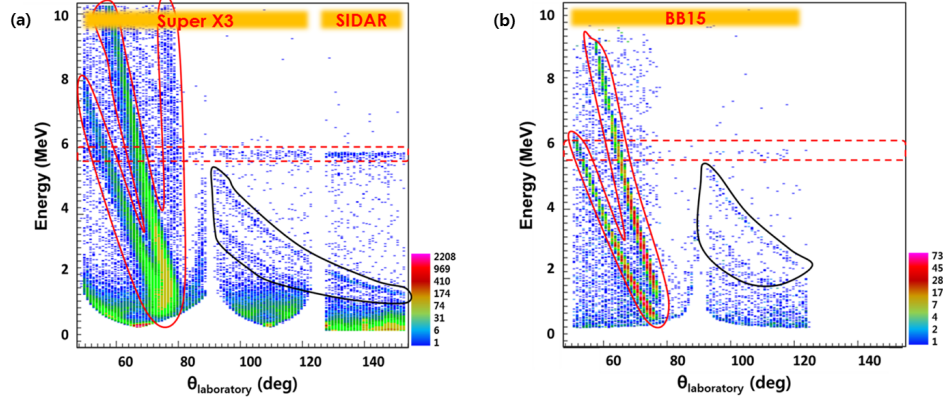
Figure 4.18: A spectrum of detected particle energy vs. laboratory angle gated on a time coincidence with a forward going recoil detected in the ion counter taken by the conventional electronics system (a) and the ASICs system (b). Two proton bands in black solid line area are clearly shown from the transfer reaction. The horizontal band (red dashed line area) at 5.8 MeV arises from a ^{244}Cm calibration source. Three fingers in red solid line area are protons, deuterons and carbons (from left to right) from the elastic scattering.

the present work are $S_{lj} = 0.27\pm0.11$, 0.45 ± 0.18 and 0.33 ± 0.13, respectively. Owing to the agreement between the calculations (with no adjustable parameters) and the observations, confidence in the procedure for calibration of the ^{80}Ge(d,p) data was obtained.

4.7 Low-lying Levels in ^{81}Ge from the ^{80}Ge(d,p)^{81}Ge Reaction

4.7.1 Q-value peaks

Figure 4.18 shows the ejectile energy versus laboratory angle spectrum as detected in the silicon detectors in coincidence with forward going germanium recoils. Two proton bands in the spectrum were clearly evident at $Q = 2.00\pm0.05$ MeV and $Q = 480\pm90$ keV (left and right peak in Figure 4.19) with a resolution of 247 keV FWHM and 429 keV FWHM, respectively, corresponding to $E_x = 634\pm50$ keV and $E_x =$
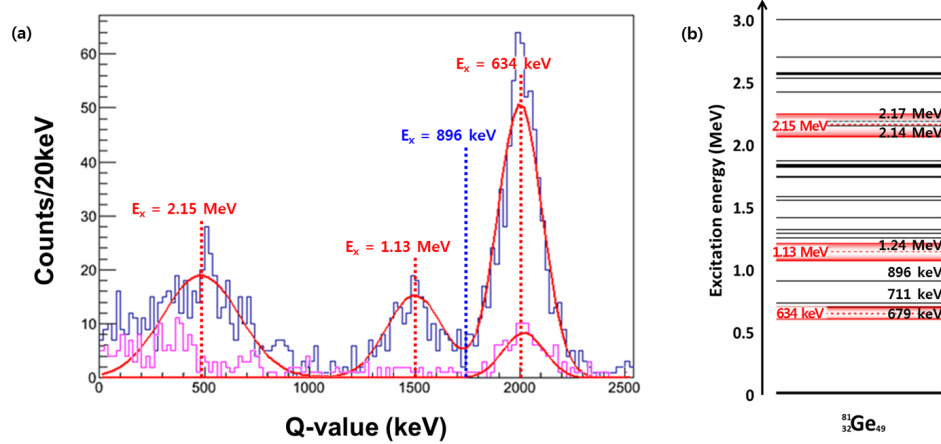
Figure 4.19: Q-value spectrum of protons from the ^{80}Ge$(d,p)^{81}$Ge reaction from the conventional electronics system (blue histograms in (a)) and from the ASICs system (purple histograms in (a)). Three peaks in data from the conventional electronics system are fitted with Gaussian shapes and their centroids were at Q = 2.00±0.05 MeV, 1.5±0.07 MeV and 480±90 keV. The corresponding energies of levels in ^{81}Ge are E_x = 634±50 keV, 1.13±0.07 MeV and 2.15±0.09 MeV, respectively. A peak in the ASICs system shows a good agreement with one of the peaks in the conventional electronics system. Two states are expected to be populated in the peak at E_x = 634±50 keV according to the measured excitation energies based on National Nuclear Data Center (NNDC) shown in (b) [18]. The ground-state Q-value of the reaction is Q = 2.635 MeV

2.15±0.09 MeV excited states, respectively. There was another peak found at Q = 1.5±0.07 MeV with 316 keV FWHM (middle peak in Figure 4.19), corresponding to E_x = 1.13±0.07 MeV. The peak at E_x = 634±50 keV implies a strong population of the previously-observed levels at 679 and 711 keV [9]. No evidence was observed for population of a level at E_x = 896 keV, which indicates the inference made in Reference [9] that this level is tentatively a hole $\frac{1}{2}^-$ state was correct. Since the population of $\frac{1}{2}^-$ in this transfer reaction requires breaking a neutron pair of the $p_{\frac{1}{2}}$ level and one of the neutrons excited to the $g_{\frac{9}{2}}$ level, it is unlikely happened and its differential cross sections are very low. Further determination of the spins and parities of the measured levels will be discussed in the following section.

4.7.2 Proton angular distribution

The angular distributions of protons emitted from the ^{80}Ge(d,p)^{81}Ge reaction were measured and compared to theoretical predictions normalized to the data. The distributions were analyzed using both DWBA and ADWA [53, 54] formalism. ADWA uses nucleonic (instead of nuclear) potentials and explicitly includes deuteron breakup. For the DWBA analysis, the optical potential for the incoming waves was the same as the one used for the elastic scattering calculation, and the potential for the outgoing wave was taken from Varner *et al.* (CH89) [5]. For the ADWA analysis, the deuteron adiabatic potential was constructed using the Johnson and Tandy optical parametrization method [54] using CH89 nucleonic potentials for the neutron and the proton. All transfer calculations in this work included finite range effects using the code FRESCO [77]. For all calculations, full complex remnant potential form in post representation was chosen. A standard radius and diffuseness of $r = 1.25$ fm and $a = 0.65$ fm were used for the bound state of the neutron. The Reid interaction [78] was used to obtain the deuteron wave function and in the transfer operator. The values of the potential parameters, derived from the global parameterizations of optical models, and including the assumed geometrical parameters of the neutron Woods-Saxon bound-state potential, are given in Table 4.4.

As shown in Figure 4.20, the angular distribution data from the peak at $E_x \sim$ 634 keV prefer the case of $l = 0$ (at $E_x = 679$ keV) transfer rather than the one of $l = 1$. The data were binned over larger angular ranges ($\theta_{c.m.} \approx 2°$ for SIDAR and $4°$ for Super X3 and BB15) than subtended by a single strip to decrease the statistical uncertainty on any point in the distribution. The plotted error bars are purely statistical.

Figure 4.21 shows that the calculation with two levels ($l = 0$ and $l = 2$) consideration produces acceptable fits to the data in the ADWA analysis. Since it is well known that the theoretical calculation accuracy is higher at small angles close to the zero degree due to the approximation [48], the curve can be fitted to the

Table 4.4: Optical model potential parameters for DWBA and ADWA calculation in ^{80}Ge(d,p)^{81}Ge reaction. The definition of the parameters are explained in Section 2.2.3. The value of r$_{Wvol}$ and a$_{Wvol}$ are the same as the one of r$_{Vvol}$ and a$_{Vvol}$. The value at * is adjusted to reproduce the binding energy of the neutron in ^{81}Ge nucleus. $d(p)$ and $d(n)$ in Channel are proton and neutron consisting deuteron, respectively.

Type	Channel	V_{vol} (MeV)	r$_{Vvol}$ (fm)	a$_{Vvol}$ (fm)	W$_{vol}$ (MeV)	W$_{sur}$ (MeV)	r$_{surf}$ (fm)	a$_{surf}$ (fm)	V_{so} (MeV)	r$_{so}$ (fm)	a$_{so}$ (fm)	r$_c$ (fm)
DWBA	d	107.47	1.05	0.86	0.0	11.74	1.43	0.74	7.00	0.75	0.5	1.3
	p	55.81	1.20	0.69	0.76	10.04	1.23	0.69	5.90	1.06	0.63	1.27
	n	*	1.25	0.65	0.00	0.00	0.00	0.00	6.00	1.25	0.65	1.3
ADWA	$d(p)$	57.41	1.20	0.69	0.55	10.31	1.23	0.69	5.90	1.06	0.63	1.27
	$d(n)$	49.14	1.20	0.69	0.97	4.51	1.23	0.69	5.90	1.06	0.63	1.27
	p	55.81	1.20	0.69	0.76	10.04	1.23	0.69	5.90	1.06	0.63	1.27
	n	*	1.25	0.65	0.00	0.00	0.00	0.00	6.00	1.25	0.65	1.3

first five data points and adjusted to the rest of data points. Figure 4.22 shows the result with the different weights, confirming the assumption of the two levels mixture is reasonable. Moreover, the shape of the differential cross section at the c.m. angles between $10°$ and $25°$ clearly shows that $l = 0$ transfer has to be included. Also, the calculation of $l = 2$ transfer clearly increased the agreement with the shape at $30° \leq \theta_{c.m.} \leq 50°$. There was a same calculation with the DWBA analysis performed and the result was in a good agreement.

Spectroscopic factors extracted from the distributions assuming this single peak containing the one level ($\frac{1}{2}^+$) or two levels ($\frac{1}{2}^+$ and $\frac{5}{2}^+$) are shown in Table 4.5. Since the data on two different detector types were independent to each other, the upper limit was set by the fit with the two data sets together and the lower limit was found by the fit with the data from SIDAR only. The uncertainties on each factor are the combination in quadrature of the statistical best-fit uncertainty (30%), the estimated uncertainty in the target thickness (13%), the systematic uncertainty (10%) due to the ambiguity of the geometrical parameters in the detector setup and the theoretical uncertainty (25%) from the sensitivity study of the calculation. This last uncertainty
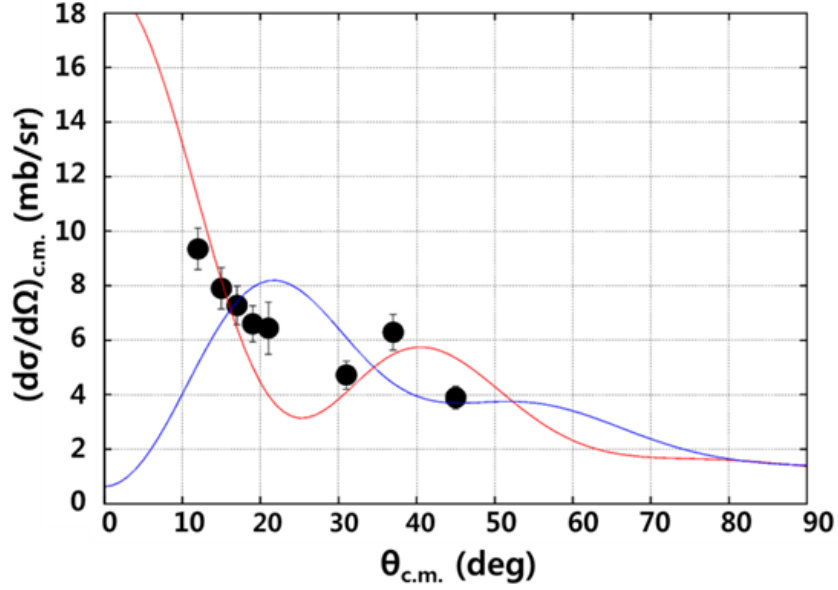
Figure 4.20: Calculated proton angular distributions from the ^{80}Ge$(d,p)^{81}$Ge reaction are compared with the data for $l = 0$ angular momentum transfer to the state at $E_x = 679$ keV (red curve). The blue curve represents the calculation for the same condition except the $l = 1$ angular momentum transfer.

was estimated by varying the bound-state potential radius parameter, r, between 1.25 to 1.35 fm and examining the effect on the extracted spectroscopic factors.

Table 4.5: Properties of low-lying states in ^{81}Ge from the measurements of the ^{80}Ge$(d,p)^{81}$Ge inverse transfer reaction.

Method	# of levels	E_x (keV)	l	J^π	S_{lj}
DWBA	1	679	0	$1/2^+$	0.58±0.26
	2	679	0	$1/2^+$	0.47±0.21
		711	2	$5/2^+$	0.18±0.08
ADWA	1	679	0	$1/2^+$	0.40 ±0.18
	2	679	0	$1/2^+$	0.32±0.14
		711	2	$5/2^+$	0.23±0.11

85
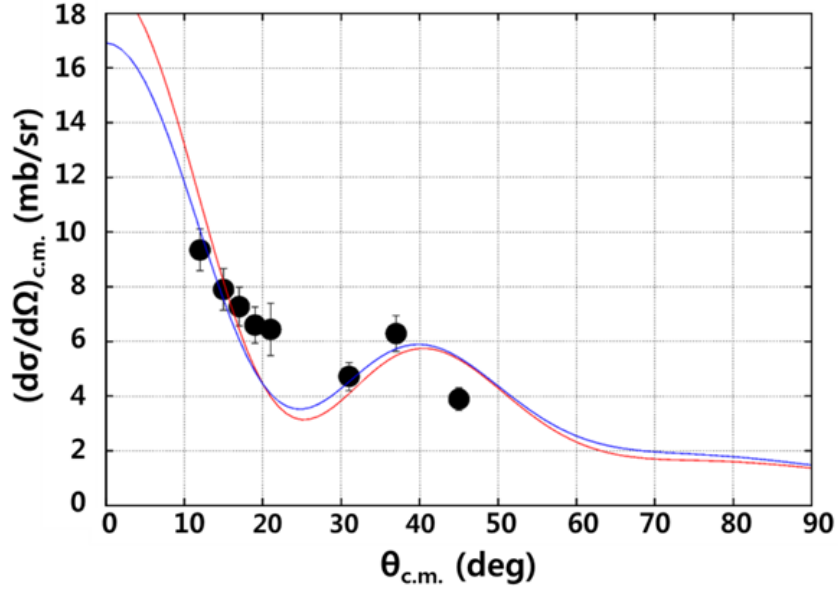
Figure 4.21: Angular distributions of protons from the ^{80}Ge$(d,p)^{81}$Ge reaction compared with calculations considering one level ($l = 0$) and two levels ($l = 0$ and $l = 2$) angular momentum transfers with ADWA analysis. The red curve shows a fit with a single level ($l = 0$) and the blue one is a fit with two levels ($l = 0$ and $l = 2$).
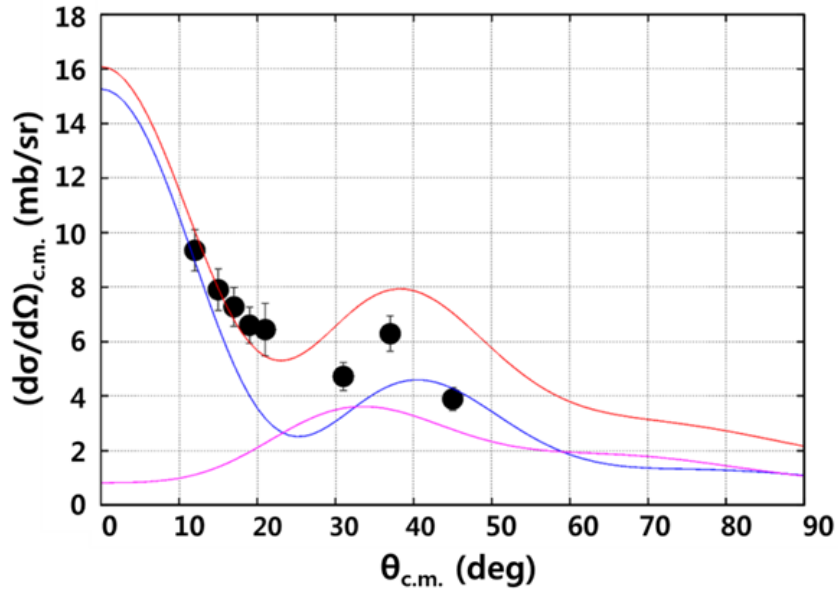
Figure 4.22: ADWA calculations of proton differential cross sections from the ^{80}Ge$(d,p)^{81}$Ge reaction for $l = 0$ and $l = 2$ angular momentum transfers with different weights on the data. The red curve is a fit with two levels ($l = 0$ and $l = 2$). The blue and purple one shows an individual contribution of $l = 0$ transfer and $l = 2$ transfer, respectively.

Chapter 5

Discussion and Conclusion

This chapter will discuss the excitation energies and spectroscopic factors obtained in this work in the context of nuclear structure and the application in astrophysics. The outlook for future studies related to this experiment will also be discussed at the end of the chapter.

5.1 Comparison with other nuclei near ^{81}Ge

The present result, in combination with Reference [9], confirms that the excitation energies of the $\frac{1}{2}^+$ and $\frac{5}{2}^+$ levels in ^{81}Ge are at $E_x = 679$ keV and 711 keV, respectively. As mentioned in Section 2.1.2, these states are intruder states with neutron 1p-2h configuration ($|\ 3s_{1/2},0^+\rangle$ and $|\ 2d_{5/2},0^+\rangle$), respectively. The nucleus ^{81}Ge has one hole in the neutron closed shell at $N = 50$ and four valence protons above the proton closed shell $Z = 28$. The ground state is expected to be a neutron single-hole state at $|\ 1g_{9/2}\rangle$ level, while excited states having a positive parity are from the population of levels above the $N = 50$ closed shell, resulting in neutron 1p-2h configurations. Since the energy of the $N = 50$ shell gap for Ge isotopes was measured to be $\Delta = S_{2n}(^{82}\text{Ge}) - S_{2n}(^{84}\text{Ge}) = 3.15$ MeV [79], the measured excitation energies of the two observed states are very low compared to the shell gap and thus a naive shell model picture is not completely adequate.
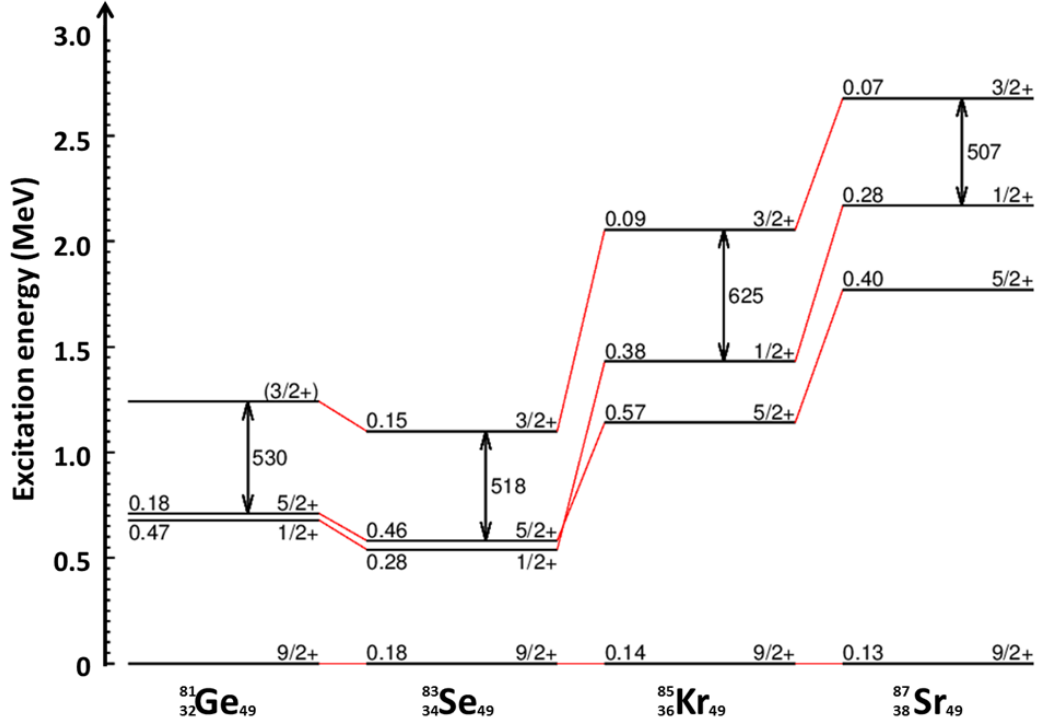
Figure 5.1: Observed intruder states ($J^{\pi} = \frac{1}{2}^{+}$, $\frac{5}{2}^{+}$ and $\frac{3}{2}^{+}$) of the even $Z < 40$, $N = 49$ isotones. Data for ^{81}Ge is from the present work and Reference [9]. Data for the other odd-mass $N = 49$ isotones: ^{87}Sr from Reference [19], ^{85}Kr from Reference [20] and ^{83}Se from Reference [3]. Spectroscopic factors extracted from transfer reactions (numbers on the left edge of the level) are also shown as well as spin and parity (right edge of the level) for each level.

As mentioned in Section 1.3, the same type of intruder states were also found in the odd-mass $N = 49$ isotones (e.g. ^{83}Se [3, 80], ^{85}Kr [20]). Fig. 5.1 shows measured energies of the intruder states on odd-mass $N = 49$ isotones. It is interesting to note that the levels at ^{81}Ge are slightly shifted up from those at ^{83}Se, and this provides the pivot point of the trend line. In order to confirm these nuclear structure implications, however, the spin (parity) and spectroscopic factor measurements of these levels in ^{79}Zn and ^{77}Ni are necessary.

The measured spectroscopic factors for ^{81}Ge are compared to the ones for ^{83}Ge ($Z = 32$, $N = 51$), ^{83}Se ($Z = 34$, $N = 49$) [3] and ^{85}Se ($Z = 34$, $N = 51$) [2] in Table 5.1. The DWBA calculation of ^{80}Ge$(d,p)^{81}$Ge reaction was performed using two OM

Table 5.1: Comparison of measured spectroscopic factors in ^{81}Ge, ^{83}Ge [2], ^{83}Se [3] and ^{85}Se [2]. BG represents the Bechetti-Greenlees OM potential [4] and CH represents that of Chapel-Hill 89 [5].

^{A}X	Z	N	OM	$S_{1/2^+}$	$S_{5/2^+}$
^{81}Ge	32	49	BG	0.47±0.21	0.21±0.09
^{81}Ge	32	49	CH	0.47±0.21	0.18±0.08
^{83}Ge	32	51	CH	0.50±0.15	0.48±0.14
^{83}Se	34	49	BG	0.28	0.46
^{85}Se	34	51	CH	0.30±0.09	0.33±0.10

potentials, Bechetti-Greenlees [4] and Chapel-Hill 89 [5] in order to keep consistency of the OM potential for the comparison. It was found that the calculations using the two potentials are in a good agreement as shown in Table 5.1. It is interesting to note that the spectroscopic factor of the $\frac{1}{2}^+$ state changes very slowly as a function of neutron number around the neutron magic number $N = 50$. In comparison, the value of the state $\frac{5}{2}^+$ changes about a factor of two in the same situation.

For the odd-mass $N = 49$ isotope chain it was found that the spectroscopic factor of the $\frac{1}{2}^+$ state in ^{81}Ge is smaller than for ^{83}Se, while the $\frac{5}{2}^+$ case is vice versa (Fig. 5.1). Nevertheless, the low value of the spectroscopic factor for both states implies the weakness of the single particle property for the structure of ^{81}Ge. It is also possible that the low spectroscopic factors indicate the structure of ^{81}Ge can be explained by the shape coexistence model as claimed in Reference [40].

5.2 Neutron Capture Cross Sections

The spectroscopic factors of ^{81}Ge in Table 4.5 were applied to the calculation of neutron capture cross sections on ^{80}Ge. As mentioned in Section 1.1, the nucleus ^{80}Ge is only one less from the magic number $N = 50$ and is also five neutrons from stability, resulting in the strong likelihood that the capture mechanism is dominated by the DSD process. DSD cross sections for ^{80}Ge were computed with the code

CUPIDO [81] performed by Goran Arbanas. The real part of the Koning-Delaroche global optical model potential [82] was used while the imaginary part of the potential was ignored by assuming the flux into other channels is very small [60]. The effect of the giant dipole resonance (GDR) and the depth of the potential for the capturing single-particle state was treated in a similar way to that used for ^{83}Ge neutron capture cross section calculation in the work by Thomas *et al.* [2].
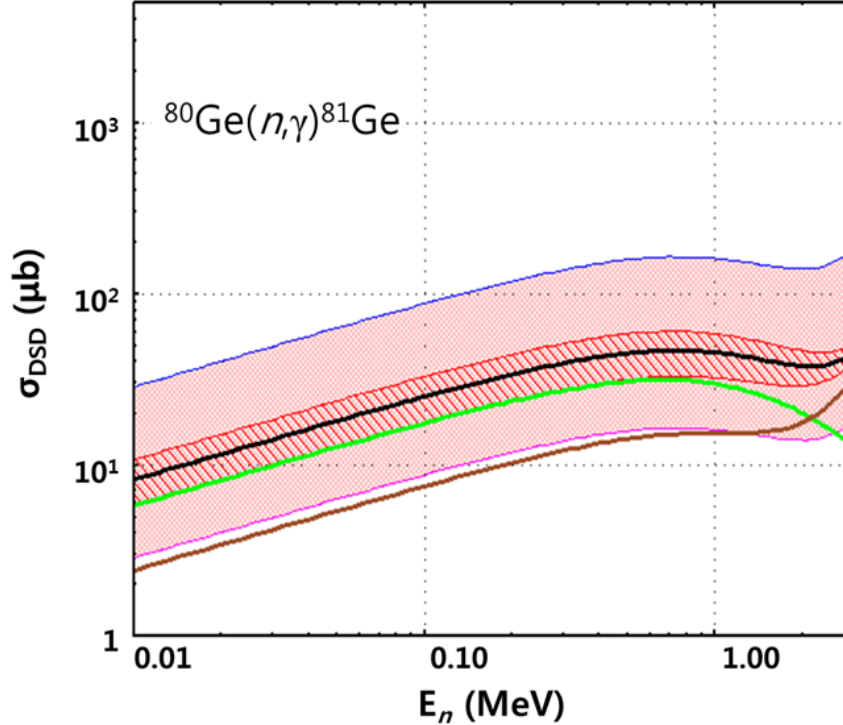
Figure 5.2: Calculated DSD cross sections (black curve) for the reactions ^{80}Ge(n, $\gamma)^{81}$Ge. Individual contributions are also plotted with green curve for the $3s_{\frac{1}{2}}$ orbital and brown curve for the $2d_{\frac{5}{2}}$ orbital. The cross sections are calculated for the $E_x = 679$ keV level using the density form of the EM operator with the semidirect (SD) contribution. The lower limit of the red hashed band shows the calculation with $S_{0\frac{1}{2}} = 0.18$ and $S_{2\frac{5}{2}} = 0.23$, and the upper limit was calculated with $S_{0\frac{1}{2}} = 0.46$ and $S_{2\frac{5}{2}} = 0.23$. A dashed light red band represents calculated cross sections for the $E_x = 679$ keV case with spectroscopic factor $S_{lj} = 1$ (top, blue) and 0.1 (bottom, purple). The uncertainty of the cross section is $\sim 30\%$ similar to the uncertainties in the measured spectroscopic factors.

The DSD capture cross sections are plotted in Fig. 5.2 as a function of neutron energy between 0.01 and 1 MeV for the computation of Maxwellian averages at

astrophysical temperatures relavant for the r-process ($E = k_B T$ where k_B is the Boltzmann constant). The spins and positive parities of the measured states in ^{81}Ge mean that the dominant direct capture contributions are expected to be through incoming p-wave neutron capture via an E1 transition into the lowest $3s$ and $2d$ states of ^{81}Ge. The energies of the excited states were set to $E_x = 679$ keV and 711 keV for $J^\pi = \frac{1}{2}^+$ and $\frac{5}{2}^+$, respectively and the spectroscopic factor was chosen as S = 0.32 for the $\frac{1}{2}^+$ state and 0.23 for the $\frac{5}{2}^+$ state. The cross section for capture to the $J^\pi = \frac{1}{2}^+$ state assuming an energy of $E_x = 896$ keV and keeping all other conditions the same was performed to find the lower limit of the cross section uncertainty affected by the energy uncertainty. The difference between $E_x = 679$ keV and 896 keV was about 10%. This tells us that the energy dependence on the cross section calculation is not strong.

Finally, using calculated cross sections, the reaction rate can be calculated by the equation written in the form:

$$\langle \sigma v \rangle = \left(\frac{8}{\pi \mu} \right)^{1/2} \frac{1}{(kT)^{3/2}} \int_0^\infty \sigma(E) E exp \left(-\frac{E}{kT} \right) dE \qquad (5.1)$$

where $\langle \sigma v \rangle$ is the reaction rate per particle pair, μ is the reduced mass of the interacting particles, k_B is the Boltzmann constant, T is the temperature, E is the kinetic energy of the neutron and $\sigma(E)$ is the nuclear cross section [21].

As a comparison, the DSD cross section was computed with spectroscopic factors ranging from 0.1 to 1 in order to estimate the uncertainty before the present measurement. As seen in Fig. 5.2, the DSD capture cross section can vary by nearly 3 orders of magnitude for ^{80}Ge, depending on the value of the spectroscopic factors. This confirms that the single particle property scaled by the spectroscopic factor plays an important role in the neutron capture process.

5.3 Conclusion

In conclusion, studying the low-lying levels of ^{81}Ge is very important because the sensitivity study pointed out that the properties of the nucleus can affect the final r-process abundance pattern, and it informs the evolution of nuclear shell structure far from stability. Spin assignments were confirmed from a study of the ^{80}Ge$(d,p)^{81}$Ge transfer reaction in inverse kinematics at the Holifield Radioactive Ion Beam Facility at Oak Ridge National Laboratory in April, 2011. The proton energy spectrum has been measured by a combination of silicon detectors including SIDAR, Super X3, and BB15. A new fast ionization counter was applied in this experiment for the beam identification and beam rate measurements. Angular distributions of low-lying levels in ^{81}Ge were measured for the first time to confirm spins and parities of the states. The spectroscopic factors, S_{lj}, extracted from the data using the ADWA analysis are 0.32 ($\pm$0.14) for the $\frac{1}{2}^+$ state and 0.23 ($\pm$0.11) for the $\frac{5}{2}^+$ state. The quoted uncertainties are the combination in quadrature of experimental and theoretical considerations.

Similar to ^{83}Se, the rather low energies observed for intruder $\frac{1}{2}^+$ and $\frac{5}{2}^+$ states in ^{81}Ge provide evidence for shape coexistence in this region of the nuclear chart. In addition, the spectroscopic factors for the first $\frac{1}{2}^+$ level near the $N = 50$ closed shell were found to change very slowly as a function of neutron number which was in stark contrast to the first $\frac{5}{2}^+$ levels.

Using these experimental results, the DSD capture cross sections for ^{80}Ge$(n,\gamma)^{81}$Ge have been calculated and the uncertainties were reduced by about an order of magnitude from previous estimates, none of which were based on experimental data. This new result which further elucidates the nuclear structure in this mass range further helps in the estimation of realistic (n,γ) reaction rate calculations for r-process nucleosynthesis for neighboring isotopes.

5.4 Outlook for Further Studies

Despite the importance of spectroscopic properties of neutron-rich nuclei far from stability, there have been relatively few nuclei studied in the laboratory [8, 31]. In particular, it is a priority to measure the properties of nuclei near doubly magic ^{78}Ni [83]. In regards to the present study on the odd-mass $N = 49$ isotones, the measurements of low-lying level properties along the odd-mass $N = 49$ isotonic chain, such as ^{79}Zn, ^{77}Ni and ^{76}Co, would be crucial to study intruder states induced by the 1p-2h correlation. They are also important for the calculation of neutron capture to help explain the observed r-process abundance pattern. These experiments can be performed by various methods, such as inverse kinematics of proton or neutron transfer reactions, β-decay measurements and β-delayed neutron measurements. In order to study ^{79}Zn, for example, the experiment of ^{78}Zn(d,p) transfer reaction in inverse kinematics was recently performed at REX-Isolde, CERN, but the data are still under analysis [84]. Comparison of low-lying levels and spectroscopic factors between ^{81}Ge and ^{79}Zn will further explain the effect of the 1p-2h correlation. The study of low-lying levels in ^{77}Ni has not been performed in the laboratory. The major difficulty in the ^{76}Ni(d,p) measurement will be the production of beams having very short lifetime and far from stability hence low production rates. Only the half life of ^{76}Ni$(t_{1/2} = 283^{+15}_{-18}$ ms) has been measured [83]. In order to perform the studies mentioned above, it will be necessary to have advanced facilities capable of producing rare isotope beams (RIB) with more intense beam rates than those available today.

Many countries including the United States, Canada, Germany, France, Switzerland, Japan, China and South Korea have invested in either upgrades to existing facilities or new facilities to make such studies possible. In the United States, for example, the Facility for Rare Isotope Beams (FRIB) [85] will deliver the highest intensity beams of rare isotopes available anywhere in the world. The projected beam intensity of ^{80}Ge in the FRIB is calculated as more than 3 orders of magnitude more than the current possible intensity [86, 87]. In the mean time, there are also

competitive on-going projects outside of the country, such as the TRIUMF Isotope Separator and Accelerator (ISAC) II facility in Canada [88], the High Intensity and Energy ISOLDE (HIE-ISOLDE) project in Europe [89], the RIKEN Accelerator Research Facility (RARF) in Japan [90], and the Rare Isotope Science Project (RISP) in South Korea [91]. All of the facilities will create many opportunities for increasing our knowledge of nuclei and the first studies of many unknown short-lived nuclei.

As the improvements in RIB production continue, the investment in the development of pure targets and improved detectors is also necessary for the future studies. Pure targets will improve the energy uncertainty of the measured particles as well as reduce the level of contaminant reactions, and better detector system will increase the energy and angle resolution as well as large solid-angle coverage and high efficiency. Locally, there are a number of projects to advance direct reaction measurements. The Jet Experiments for Nuclear Structure and Astrophysics (JENSA) gas-jet target is one of many projects currently under construction at ORNL [92]. The gas jet target will provide a high density and high purity of target nuclei within a tightly confined region, without the use of windows or backing materials. Detectors are mounted inside the jet target chamber around the jet-beam interaction point to detect outgoing charged particle reaction products. Another example is the ANASEN detector system which is an on-going project at Louisiana State University and Florida State University to provide an active gas target [62]. For charged particle detection, SuperORRUBA will provide good energy and angular resolution with high detection efficiency [63]. SuperORRUBA was recently constructed and is in routine use. A scintillator array for detecting gamma rays, called HAGRiD, will measure the energy of gamma rays with good energy resolution and high efficiency, with the advantage of a new generation scintillator material, LaBr3(Ce) [93]. The HAGRiD is currently under development. Finally, neutron detectors such as the Versatile Array of Neutron Detectors at Low Energy (VANDLE) are necessary for (d,n), (p,n) and β-delayed neutron decay measurements [94]. The VANDLE array was also recently developed

and is in use. VANDLE is made of plastic scintillator bars with low neutron detection thresholds around 100-200 keVee for neutron energy measurements via time of flight.

Bibliography

96

[1] SIDAR silicon detector array.
http://www.phy.ornl.gov/hribf/equipment/sidar/. xi, 37, 47

[2] J. S. Thomas, G. Arbanas, D. W. Bardayan, J. C. Blackmon, J. A. Cizewski, D. J. Dean, R. P. Fitzgerald, U. Greife, C. J. Gross, M. S. Johnson, K. L. Jones, R. L. Kozub, J. F. Liang, R. J. Livesay, Z. Ma, B. H. Moazen, C. D. Nesaraja, D. Shapira, M. S. Smith, and D. W. Visser. *Phys. Rev. C*, 76:044302, 2007. xi, 5, 88, 89, 90

[3] L. A. Montestruque, M. C. Cobian-Rozak, G. Szaloky, J. D. Zumbro, and S. E. Darden. *Nucl. Phys.*, A305:29, 1978. xi, xviii, xix, xxi, 9, 27, 76, 77, 78, 79, 88, 89

[4] F. D. Becchetti, Jr. and G. W. Greenlees. *Phys. Rev.*, 182:1190, 1969. xi, 27, 89

[5] R. L. Varner, W. J. Thompson, T. L. McAbee, E. J. Ludwig, and T. B. Clegg. *Phys. Rep.*, 201:57, 1991. xi, 27, 83, 89

[6] C. A. Barnes, D. D. Clayton, D. N. Schramm, and M. A. Fowler. *Essays in Nuclear Astrophysics*. Cambridge University Press, 1982. xiii, 2

[7] M. S. Smith and K. E. Rehm. *Ann. Rev. of Nucl. Part. Sci.*, 51:91, 2001. xiii, 4

[8] J. Erler, N. Birge, M. Kortelainen, W. Nazarewicz, E. Olsen, A. M. Perhac, and M. Stoitsov. *Nature*, 486:509, 2012. xiii, 6, 7, 93

[9] P. Hoff and B. Fogelberg. *Nucl. Phys. A*, 368:210, 1981. xiii, xxi, 9, 10, 82, 87, 88

[10] R. A. Surman, M. R. Mumpower, G. C. McLaughlin, R. Sinclair, W. R. Hix, and K. L. Jones. Neutron capture and the r-process. In *14th International Symposium on Capture Gamma-Ray Spectroscopy and Related Topics*, 2013. xiii, 9, 11

[11] S. M. Brown. *Neutron Shell Breaking in Neutron-Rich Neon Isotopes*. PhD thesis, Department of Physics, University of Surrey, 2010. xiv, 16

[12] K. Y. Chae, D. W. Bardayan, M. S. Smith, K. T. Schmitt, S. H. Ahn, W. A. Peters, and S. Strauss. *Bull. Amer. Phys. Soc.*, 56, No. 12, 2011. xiv, xv, 38, 52

[13] Holifield Radioactive Ion Beam Facility. http://www.phy.ornl.gov/hribf/misc/ whatishribf.shtml. xiv, 39

[14] D. W. Stracener. *Nucl. Instrum. Meth. B*, 204:42, 2003. xiv, 39, 40

[15] The Tandem Electrostatic Accelerator. https://www.phy.ornl.gov/hribf/accelerator/ tandemweb/. xiv, 41

[16] K. S. Krane. *Introductory Nuclear Physics*. Wiley, 1987. xv, 7, 13, 35, 43, 44, 51

[17] S. D. Pain. Overview of the Oak Ridge Rutgers University Barrel Array ORRUBA. An ORRUBA development review presentation, 2004. xv, 44, 45

[18] National Nuclear Data Center. http://www.nndc.bnl.gov/. xx, 82

[19] B. L. Burks, R. E. Anderson, T. B. Clegg, E. J. Ludwig, B. C. Karp, and Y. Aoki. *Nucl. Phys. A*, 457:337, 1986. xxi, 9, 88

[20] N. A. Detorie, P. L. Jalivette, C. P. Browne, and A. A. Rollefson. *Phys. Rev. C*, 18:991, 1978. xxi, 9, 88

[21] C. E. Rolfs and W. S. Rodney. *Cauldrons in the Cosmos: Nuclear Astrophysics*. University of Chicago Press, 1988. 1, 2, 3, 91

[22] A. S. Eddington. *Nature*, 106:14, 1920. 1

[23] E. M. Burbidge, G. R. Burbidge, W. A. Fowler, and F. Hoyle. *Rev. Mod. Phys.*, 29:547, 1957. 1, 2, 4

[24] A. G. W. Cameron. *Stellar evolution, nuclear astrophysics, and nucleogenesis.* Atomic Energy of Canada Limited, Chalk River Project, Research and Development, 1957. 4

[25] W. Hauser and H. Feshbach. *Phys. Rev.*, 87:366, 1952. 5

[26] K. L. Jones, F. M. Nunes, A. S. Adekola, D. W. Bardayan, J. C. Blackmon, K. Y. Chae, K. A. Chipps, J. A. Cizewski, L. Erikson, C. Harlin, R. Hatarik, R. Kapler, R. L. Kozub, J. F. Liang, R. Livesay, Z. Ma, B. Moazen, C. D Nesaraja, S. D. Pain, N. P. Patterson, D. Shapira, J. F. Shriner, Jr., M. S. Smith, T. P. Swan, and J. S. Thomas. *Phys. Rev. C*, 84:034601, 2011. 5, 75

[27] T. Rauscher, K. L. Kratz, H. 0berhummer, J. Dobaczewski, P. Möller, and M. Sharma. *Nucl. Phys.*, A 621:327c, 1997. 5

[28] W. A. Fowler. *Rev. Mod. Phys.*, 56:149, 1984. 6

[29] K.-L. Kratz, J.-P. Bitouzet, F.-K. Thielemann, P. M oller, and B. Pfeiffer. *Astrophys. J.*, 403:216, 1993. 6

[30] B. Pfeiffer, K.-L. Kratz, and F.-K. Thielemann. *Z. Phys. A*, 357:235, 1997. 6

[31] M. Thoennessen and B. Sherrill. *Nature*, 473:25, 2011. 7, 93

[32] M. G. Mayer. *Phys. Rev.*, 75:1969, 1949. 7, 14

[33] O. Haxel, J. H. D. Jensen, and H. E. Suess. *Phys. Rev.*, 75:1766, 1949. 7, 14

[34] K. Heyde, P. Van Isacker, M. Waroquier, J. L. Wood, and R. A. Meyer. *Phys. Rep.*, 102:291, 1983. 8, 19, 20

[35] J. L. Wood, K. Heyde, W. Nazarewicz, M. Huyse, and P. van Duppen. *Phys. Rep.*, 215:101, 1992. 8, 19

[36] K. Heyde and J. L. Wood. *Rev. of Mod. Phy.*, 83:1467, 2011. 8, 18

[37] H. Morinaga. *Phys. Rev.*, 101:254, 1956. 8

[38] S. L. Heller and J. N. Friedman. *Phys. Rev. C*, 10:1509, 1974. 8

[39] K. Heyde, M. Waroquier, and R. A. Meyer. *Phys. Rev. C*, 17:1219, 1978. 8

[40] R. A. Meyer, O. G. Lien, III, and E. A. Henry. *Phys. Rev. C*, 25:682, 1982. 8, 11, 19, 20, 89

[41] J. V. Katz, H. Franz, N. Kaffrel, and G. Herrmann. *Nucl. Phys. A*, 250:13, 1975. 9

[42] J. Beun, J. C. Blackmon, W. R. Hix, G. C. McLaughlin, M. S. Smith, and R. Surman. *J. Phys. G*, 36:025201, 2009. 9

[43] R. Surman, J. Beun, G. C. McLaughlin, and W. R. Hix. *Phys. Rev. C*, 79:045809, 2009. 9

[44] M. H. MacGregor, R. A. Arndt, and R. M. Wright. *Phys. Rev.*, 182:1714, 1969. 14

[45] R. D. Woods and D. S. Saxon. *Phys. Rev.*, 95:577, 1954. 14, 15

[46] M. G. Mayer and J. H. D. Jensen. *Elementary Theory of Nuclear Shell Structure*. Literary Licensing, LLC, 2013. 15

[47] A. Bohr and B. R. Mottelson. *Nuclear Structure*. Nuclear Structure Vol 1 Single Structure Motion. World Scientific, 1998. 15

[48] I. J. Thompson and F. M. Nunes. *Nuclear Reactions for Astrophysics: Principles, Calculation and Applications of Low-Energy Reactions*. Cambridge University Press, 2009. 23, 24, 83

[49] G. R. Satchler. *Direct nuclear reactions*. Clarendon Press, 1983. 23, 24

[50] N. K. Glendenning. *Direct nuclear Reactions.* Elsevier Science, 1983. 23, 24

[51] C. M. Perey and F. G. Perey. *At. Data Nucl. Data Tables*, 17:1, 1976. 26

[52] J. M. Lohr and W. Haeberli. *Nucl. Phys.*, A232:381, 1974. 27, 76

[53] R. C. Johnson and P. J. R. Soper. *Phys. Rev. C*, 1:976, 1970. 28, 83

[54] R. C. Johnson and P. C. Tandy. *Nucl. Phys.*, A 235:56, 1974. 28, 83

[55] F. M. Nunes and A. Deltuva. *Phys. Rev. C*, 84:034607, 2011. 28

[56] W. N. Catford, D. M. Pringle, D. G. Lewis, A. E. Smith, E. F. Garman, I.F. Wright, and J. Lukasiak. *Nucl. Instrum. Meth. A*, 247:367, 1986. 31

[57] Los Alamos Scientific Laboratory, N. Jarmie, R. C. Allen, and J. D. Seagrave. *Charged Particle Cross Sections.* Los Alamos Scientific Laboratory, 1957. 31, 32

[58] A. M. Baldin. *Kinematics of Nuclear Reactions.* Pergamon Press, 1961. 31, 32

[59] H. Oberhummer, J. H. Applegate, J. J. Cowan, F. Kppeler, H. V. Klapdor-Kleingrothaus, K. Langanke, R. A. Malaney, B. E. J. Pagel, C. Rolfs, G. Schatz, et al. *Nuclei in the Cosmos.* Springer London, Limited, 2012. 35

[60] E. Krausmann, W. Balogh, H. Oberhummer, T. Rauscher, K. L. Kratz, and W. Ziegert. *Phys. Rev. C*, 53:469, 1996. 35, 90

[61] K. H. Kim, M. H. Park, and B. T. Kim. *Phys. Rev. C*, 35:363, 1987. 35

[62] M. Matoš, J. C. Blackmon, H. E. Gardiner, L. E. Linhardt, K. T. Macon, L. L. Mondello, L. Baby, E. Johnson, E. Koshchy, G. Rogachev, I. Wiedenhöver, and D. W. Bardayan. The Array for Nuclear Astrophysics Studies with Exotic Nuclei (ANASEN). In *14th International Symposium on Capture Gamma-Ray Spectroscopy and Related Topics*, 2013. 37, 48, 94

[63] D. W. Bardayan, S. Ahn, J. C. Blackmon, A. J. Burkhart, K. Y. Chae, J. A. Cizewski, J. Elson, S. Hardy, R. L. Kozub, L. Linhardt, B. Manning, M. Matoš, S. D. Pain, L. G. Sobotka, and M. S. Smith. *Nucl. Instrum. Meth. A*, 711:160, 2013. 37, 49, 94, 119

[64] MINI silicon detector array. http://www.micronsemiconductor.co.uk/pdf/s.pdf. 37

[65] S. D. Pain, J. A. Cizewski, R. Hatarik, K. L. Jones, J. S. Thomas, D. W. Bardayan, J. C. Blackmon, C. D. Nesaraja, M. S. Smith, R. L. Kozub, and M. S. Johnson. *Nucl. Instrum. Meth. B*, 261:1122, 2007. 37, 47

[66] D. W. Stracener, G. D. Alton, R. L. Auble, J. R. Beene, P. E. Mueller, and J. C. Bilheux. *Nucl. Instrum. Meth. A*, 521:126, 2004. 38

[67] H. K. Carter, J. Kormicki, D. W. Stracener, J. B. Breitenbach, J. C. Blackmon, M. S. Smith, and D. W. Bardayan. *Nucl. Instrum. Meth. B*, 126:166, 1997. 38

[68] C. M. Bartle and H. O. Meyer. *Nucl. Instrum. Meth.*, 112:615, 1973. 40

[69] M. J. Berger, J. S. Coursey, M. A. Zucker, and J. Chang. *ESTAR, PSTAR, and ASTAR: Computer Programs for Calculating Stopping-Power and Range Tables for Electrons, Protons, and Helium Ions.* (version 1.2.3), (2000) Available: http://physics.nist.gov/Star [2013, June 18] National Institute of Standards and Technology, Gaithersburg, MD, 2005. 43

[70] G. F. Knoll. *Radiation Detection and Measurement.* John Wiley & Sons, 2010. 51

[71] K. Kimura, T. Izumikawa, R. Koyama, T. Ohnishi, T. Ohtsubo, A. Ozawa, W. Shinozaki, T. Suzuki, M. Takahashi, I. Tanihata, T. Yamaguchi, and Y. Yamaguchi. *Nucl. Instrum. Meth. A*, 538:608 – 614, 2005. 52

[72] M. S. Wallace, M. A. Famiano, M.-J. van Goethem, A. M. Rogers, W. G. Lynch, J. Clifford, F. Delaunay, J. Lee, S. Labostov, M. Mocko, L. Morris, A. Moroni, B. E. Nett, D. J. Oostdyk, R. Krishnasamy, M. B. Tsang, R. T. de Souza, S. Hudan, L. G. Sobotka, R. J. Charity, J. M. Elson, and G. L. Engel. *Nucl. Instrum. Meth. A*, 583:302, 2007. 55, 56

[73] G. L. Engel, M. Sadasivam, M. Nethi, J. M. Elson, L. G. Sobotka, and R. J. Charity. *Nucl. Instrum. Meth. A*, 573:418, 2007. 55, 111

[74] S. Hardy. Development of Super-ORRUBA for the Study of the ^{26}Al$(d,p)^{27}$Al Reaction. Master's thesis, Department of Physics, University of Surrey, 2012. M. Phys thesis. 57

[75] B. Manning, J. A. Cizewski, R. L. Kozub, S. H. Ahn, D. W. Bardayan, K. Y. Chae, K. A. Chipps, M. E. Howard, K. L. Jones, J. F. Liang, M. Matoš, C. D. Nesaraja, P. D. O'Malley, S. D. Pain, W. A. Peters, S. T. Pittman, A. Ratkiewicz, K. T. Schmitt, D. Shapira, and M. S. Smith. *Bull. Amer. Phys. Soc.*, 57, No. 9:85, 2012. 57

[76] K. T. Schmitt, K. L. Jones, S. H. Ahn A. Bey, D.W. Bardayan, J. C. Blackmon, S.M. Brown, K. Y. Chae, K. A. Chipps, J. A. Cizewski, K. I. Hahn, J. J. Kolata, R. L. Kozub, J. F. Liang, C. Matei, M. Matoš, D. Matyas, B. Moazen, C. Nesaraja, F.M. Nunes, P. D. OMalley, S. D. Pain, W. A. Peters, S. T. Pittman, A. Roberts, D. Shapira, J. F. Shriner, Jr., M. S. Smith, I. Spassova, D. W. Stracener, A. N. Villano, and G. L. Wilson. *Phys. Rev. Lett.*, 108:192701, 2012. 75

[77] I. J. Thompson. *Comput. Phys. Rep.*, 7:167, 1988. 76, 79, 83

[78] R. V. Reid, Jr. *Ann. Phys.*, 50:411, 1968. 83

[79] J. Hakala, S. Rahaman, V. V. Elomaa, T. Eronen, U. Hager, A. Jokinen, A. Kankainen, I. D. Moore, H. Penttilä, S. Rinta-Antila, J. Rissanen,

A. Saastamoinen, T. Sonoda, C. Weber, and J. Äystö. *Phy. Rev. Lett.*, 101:052502, 2008. 87

[80] E. K. Lin. *Phys. Rev. B*, 139:340, 1965. 88

[81] W. E. Parker, M. B. Chadwick, F. S. Dietrich, J. E. Kammeraad, S. J. Luke, K. E. Sale, R. M. Chasteler, M. A. Godwin, L. H. Kramer, G. J. Schmid, H. R. Weller, and A. K. Kerman. *Phys. Rev. C*, 52:252, 1995. 90

[82] A. J. Koning and J. P. Delaroche. *Nucl. Phys.*, A 713:231, 2003. 90

[83] P. T. Hosmer, H. Schatz, A. Aprahamian, O. Arndt, R. R. C. Clement, A. Estrade, K. L. Kratz, S. N. Liddick, P. F. Mantica, W. F. Mueller, F. Montes, A. C. Morton, M. Ouellette, E. Pellegrini, B. Pfeiffer, P. Reeder, P. Santi, M. Steiner, A. Stolz, B. E. Tomlin, W. B. Walters, and A. Wöhr. *Phys. Rev. Lett.*, 94:112501, 2005. 93

[84] R. Orlandi. Single-particle state in 79Zn. A neutron-transfer experiment at REX-ISOLDE. A seminar at Laboratori Nazionali di Legnaro, 2012. 93

[85] Facility for Rare Isotope Beams. http://www.frib.msu.edu/. 93

[86] Projected FRIB rates. https://groups.nscl.msu.edu/frib/rates/fribrates.html. 93

[87] Estimate Rare Isotope Yields in NSCL. http://www.nscl.msu.edu/exp/propexp/ yields. 93

[88] ISAC Facilities for Rare-Isotope Beams. http://www.triumf.ca/research-program/research-facilities/isac-facilities. 94

[89] The HIE-ISOLDE Project. http://hie-isolde.web.cern.ch/. 94

[90] RIKEN Accelerator Research Facility. http://www.rarf.riken.go.jp/rarf/. 94

[91] Rare Isotope Science Project. http://www.risp.re.kr/eng/pmainpage.do. 94

[92] K. A. Chipps, D. W. Bardayan, J. C. Blackmon, J. Browne, M. Couder, L. E. Erikson, U. Greife, U. Hager, A. Kontos, A. Lemut, L. E. Linhardt, Z. Meisel, F. Montes, S. D. Pain, D. Robertson, F. Sarazin, H. Schatz, K. T. Schmitt, M. S. Smith, P. Vetter, , and M. Wiescher. A gas jet target for radioactive ion beam experiments. In *Application of Accelerators in Research and Industry Twenty-Second International Conference*, page 625, 2013. 94

[93] K. L. Jones. private communication, 2013. 94

[94] C. Matei, D. W. Bardayan, J. C. Blackmon, J. A. Cizewski, R. K. Grzywacz, S. N. Liddick, W. A. Peters, and F. Sarazin. Development of a Versatile Array of Neutron Detectors at Low Energy. In *Application of Accelerators in Research and Industry Twentieth International Conference*, page 790, 2009. 94

[95] HRIBF Data Acquisition Software. http://www.phy.ornl.gov/computing/daqsupport.html. 108

[96] UPAK Analysis Software. http://www.phy.ornl.gov/computing/daqsupport.html. 108

[97] ORNL DAQ ASICs system Blog. http://asics.tonian.org/. 137

Appendix

Appendix A

ORNL DAQ ASICs Documentation

A.1   Introduction

This manual is intended to provide detailed documentation for the ASICs device
implemented in the ORNL DAQ system. The implementation was performed for
use of ASICs with an array of silicon strip detectors such as SuperORRUBA.
Section A.2 will describe hardware and software requirements in order to run the
ORNL DAQ system in general. A brief guide how to setup hardware will be
explained in Section A.3. Finally, Section A.4 will explain how to install ASICs
software. The section will also explain how to initialize devices and how to set up
parameters as well as how to take data with them.

A.2   System Requirements

A.2.1   Hardware requirements

The ORNL DAQ computer requires two network interface cards supporting
Ethernet for communication with VME I/F module and for sharing data with other
computers, respectively. In addition, the ASICs motherboard communicates with
XLMXXV Universal Logic Module (XLMXXV) via a Versa Module Eurocard Bus

(VMEbus) crate. VMEbus is a computer bus standard and has a high interoperability with multiple modules. ASICs software and ORNL DAQ system are developed to communicate with a VME I/F module in the VMEbus crate to control the ASICs devices. A Nuclear Instrumentation Module (NIM) crate is also required for NIM modules to handle various analog signals.

A.2.2   Software requirements

The ASICs software package version 4.0 has been designed to run on the Linux 32-bit x86 system (Redhat RHEL5 or newer). It is important to be sure that all compiling dependencies are met before installing the package. The user must first verify that each of these dependencies are installed on the target system.

- GCC 4.2 with GFORTRAN
- HRIBF Data Acquisition Software [95]
- UPAK Analysis Software [96]
- Java SE Runtime Environment 7
- Trivial File Transfer Protocol (TFTP) Server

Installation guide of the software packages will be briefly described in Section A.4. Since the ORNL DAQ system uses special network ports, one has to add the ports in the list of firewall by inserting the below code in the end of a file named "iptables":

```
#45080 - event data
#45081 - request boot
#45082 - force boot
#45083 - code download
#45084 - fastbus command
#45085 - camac command
#45086 - control command
#45087 - message to workstation
#45088 - testing protocol
#45089 - messages to/from applications
#45090 - traces from Gretina
#45091 - control of Gretina modules
#45092 - WU ASICS XLM control
#45093 - VME commands
```
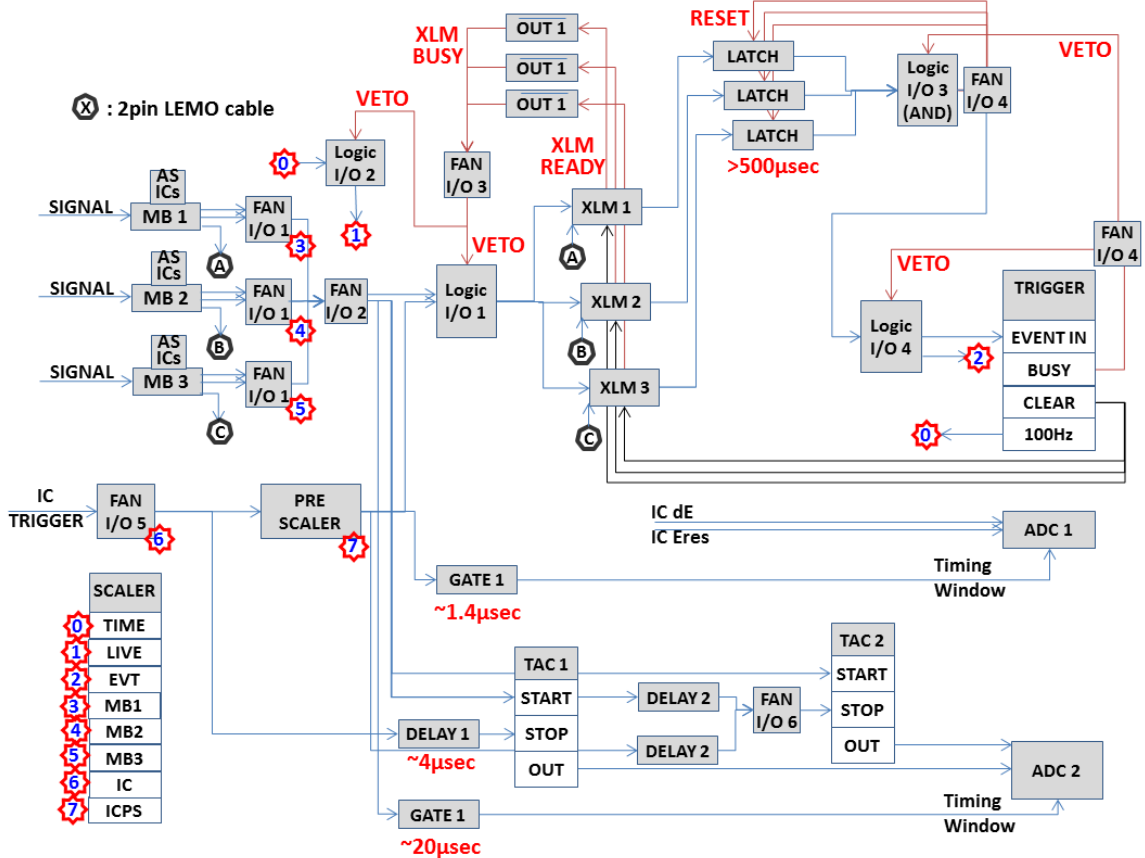
Figure A.1: A schematic diagram of a hardware setup for data acquisition using ASICs System. In the setup, 3 ASICs motherboards, two ADCs and one scaler are included.

```
#45094 - LN filling system commands
#45095 - RMS/DRS control systems
-A INPUT -m state --state NEW -m udp -p udp --dport 45080:45096 -j ACCEPT
```

The file "iptables" is the configuration file for the firewall setup in the Linux system and is usually located in the directory "/etc/sysconfig/".

A.3 Hardware Setup

Figure A.1 shows an overall diagram of hardware setup using 3 ASICs motherboards, 3 XLMXXVs, two ADCs (one for Ionization counter signals and

another for TAC signals). A signal from the preamplifier goes into the ASICs chipboard, then a trigger and a shaped energy signal are produced by ASICs chips and transfered to the motherboard. Trigger signals from all of chipboards within a predefined time window are combined in the motherboard. They come out from the output of the motherboard and are combined again with other trigger signals from other motherboards ("FAN I/O 2" in Figure A.1). They are duplicated by a fan-out module and used as a "start" signal of TAC module and trigger signals, called "XLM trigger", for the XLMXXV module. When the XLMXXV is triggered by them, it communicates with the motherboard to receive the shaped energy signals read by the ADC of the XLMXXV and to save the digitized value of the energy signal in it internal memory. Once it completes, it generates a trigger signal, called "VME trigger", which lets the VME I/F start reading the memory of XLMXXV and record them in an event buffer. Each of the "VME trigger"s is latched and waits to be delivered to the VME I/F, until all of XLMXXVs produce the trigger. This prevents the VME I/F to read data before all XLMXXVs complete recording. There are "XLM busy" signals and "VME busy" signals used for veto signals to prevent triggering XLMXXV or VME, respectively.

During an experiment, a beam intensity is usually more than 10^5 particles per second (pps). Since the ionization counter (IC) is used to measure the beam intensity, the frequency of the IC triggers is close to the beam intensity. Thus, a prescaler is required to reduce the frequency because the DAQ system will be busy all the time to analyze the IC signals resulting in missing signals from other detectors. Since the ASICs system doesn't have a function of prescaler and its deadtime increases to $\sim 30\%$ with data rates on the order of 1 kHz,a external prescaler and the CAEN V785 ADC modules can be used to handle IC signals. The original IC trigger signals can be used as a "stop" signal of the TAC to find the coincident event with other detectors generating "start" signals. These TAC signals are digitized by the CAEN V785 ADC module (ADC2 in Figure A.1). The following detailed descriptions will refer to each part of the diagram.
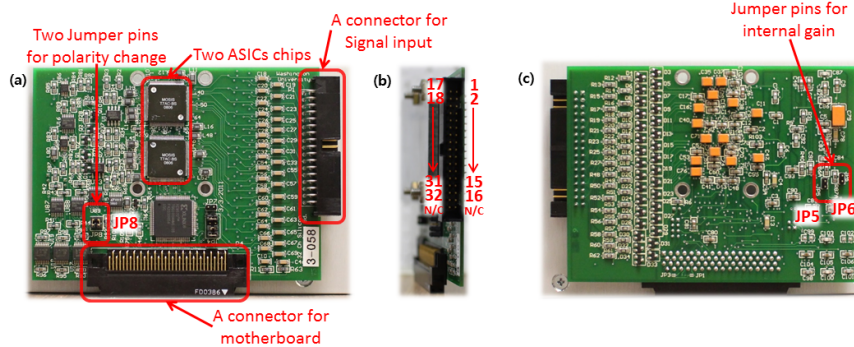
Figure A.2: (a) ASICs chipboard front. (b) A signal input connector with the order of channels. (c) ASICs chipboard back. Jumper pins for gain selection are on JP5 and JP6. And jumpers on JP8 are for polarity change.

A.3.1 ASICs chipboards and motherboards

Figure A.2 shows front side and backside of an ASICs chipboard including two ASICs chips (HINP16C [73]). Both positive and negative polarity signals can be analyzed by the ASICs chip. Here, the polarity is defined as the one before the CSA (or preamplifier). This is explained in Table A.4. It should be noted that the lowest ADC channel number in the ASICs system is zero in case of the positive polarity setup and 16383 in case of negative polarity setup, while the highest ADC channel number is 16383 in case of the positive polarity setup and zero in case of negative polarity setup. In order to remove this confusion, a new chipboard, labeled with 3-XXX, is released with jumpers on the front side of the board, JP8, to allow the polarity of the differential energy output to be reversed, so that the ADC channel numbers for both signal polarities are increased to the same direction. With the horizontal setup of jumpers in terms of the letters "JP8", the lowest ADC channel number is zero for negative polarity setup as well as the highest ADC channel number is 16383 for the same polarity setup.

There are also a pair of jumpers on the back side of the board, JP5 and JP6 to provide the gain selection of the differential analog output. When all jumpers are removed, the gain is increased by the differential amplifier switched on. The

111
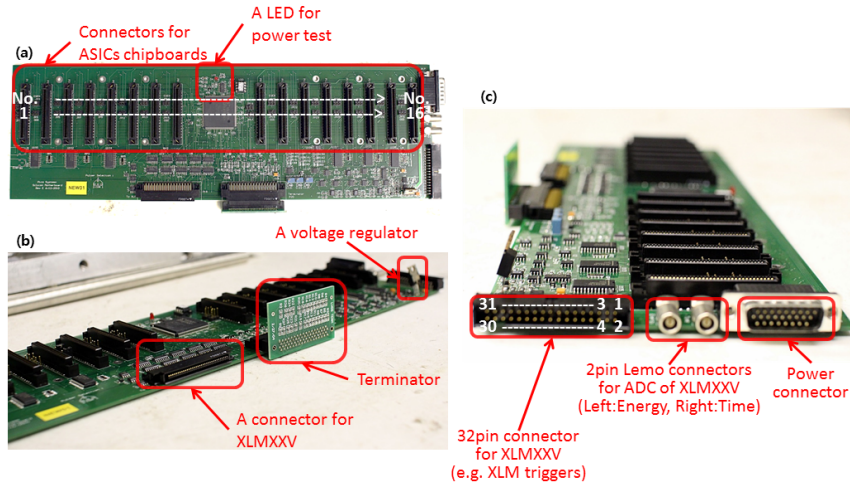
Figure A.3: The ASICs motherboard is shown as top view (a), front view (b) and right side view (c). The ASICs chipboards are plugged in an order from left (furthest to the power connector) to right. Numbers on the 34pin connector are pin number related to Table A.1.

jumpers should always both be in, or both be out to keep the differential circuit balanced. There will be a different zero position at each gain, so the offset has to be changed in the software. The differential amplifier expands around electrical zero, which will be channel 8192 on a 14-bit ADC. So, a good zero on one gain setting will either be off-scale if the gain is increased, or toward the middle of the scale if it is decreased. It has no effect on the threshold, except that it could take more signal to reach the same ADC channel if the gain is changed. The estimated gain of the high gain (both jumpers out) is 5 times higher than the one of the low gain (both jumpers in). The linearity of the gain was verified up to 1.5 V for both the high gain and the low gain. Because the high gain usually has better resolution of the energy, all of chipboards in ORNL DAQ ASICs have the gain jumpers removed. The ASICs motherboard is designed to hold up to 16 ASICs chipboards. Typical chipboard counts were somewhat lower (up to 10), however, because of the desire to control and stabilize the operating temperature of the electronics system. Figure A.3 shows details of important parts in the motherboard. The XLM triggers

and shaping test output come out of the 34pin connector, and energy shaped signals are from one of two-pin LEMO connectors. Table A.1 shows output signals for each pin of the 34pin connector. The chipboards and motherboard are powered by a

Table A.1: Output list of 34pin connector on the ASICs motherboard

Pin No.	Signal Name	Description
1	COM_STOP	Stop all TVC integrators
3	CFD_test	Test output of selected channel discriminator signal
5	OR A	Triggers from selected chip boards (OR A in ASICs setup file)
7	OR B	Triggers from selected chip boards (OR B in ASICs setup file)
9	OR C	Triggers from selected chip boards (OR C in ASICs setup file)
11	CSA_test	Test output of selected channel CSA signal
13	SHAPER_test	Test output of selected channel shaper signal
15	SUM A	Sum of Multiplicity outputs from selected chip boards
17	SUM B	Sum of Multiplicity outputs from selected chip boards
19	SUM C	Sum of Multiplicity outputs from selected chip boards
21	Pulser 1 Even	Test Pulser No. 1 to Even channels CSA Inputs
23	Pulser 1 Odd	Test Pulser No. 1 to Odd channels CSA Inputs
25	Pulser 2 Even	Test Pulser No. 2 to Even channels CSA Inputs
27	Pulser 2 Odd	Test Pulser No. 2 to Odd channels CSA Inputs
29	Pulser 3 Even	Test Pulser No. 3 to Even channels CSA Inputs
31	Pulser 3 Odd	Test Pulser No. 3 to Odd channels CSA Inputs

regulated +5 V by a voltage regulator IRLZ34N (Q9 on the motherboard) with external +6 V power. The regulator can overheat and thus, cooling the regulator is important to prevent malfunction of the motherboard. The pin map of the power connector can be found in Table A.2.

Table A.2: Pin map of power connector on the ASICs motherboard

Signal Name	Pin No.	Function
+6 V	1,10	+6 V power to motherboard and chips
−6 V	2	−6 V power to motherboard for SHAPE_test
+12 V	20	+12 V power to motherboard for a regulator
GND	11,12,19,22,24,26	Ground pins
N/A	3,4,5,6,7,8,9,13	Detector bias, not used in the system
N/A	14,15,16,17,18,21,23,25	Detector bias, not used in the system

Figure A.4 guides how to connect cables between XLMXXV and the ASICs motherboard. As mentioned in Section 3.4.2, an ADC board is embedded in the XLMXXV to digitize the energy and time signal peak heights from the
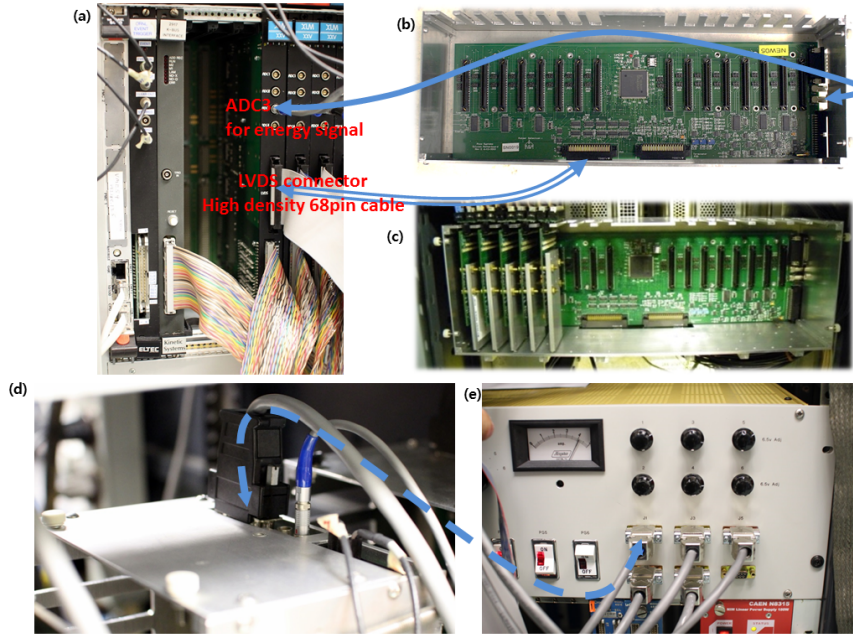
Figure A.4: Cable connection between XLMXXV and ASICs motherboard with the power supply. (a) XLMXXV in VMEbus crate. (b) ASICs motherboard without chipboards. (c) ASICs motherboard with chipboards. (d) A power cable and two-pin LEMO cable plugged in the ASICs motherboard. (e) ASICs power supply supporting 6 motherboards. Blue solid both-heads line represents two-pin LEMO cable for the energy shaped signals from the motherboard to ADC3 of the XLMXXV front panel. Blue double-lined both-heads line shows how to connect LVDS 68pin cable between XLMXXV and the ASICs motherboard. Blue dash both-heads line represents the power cable from the power supply to the motherboard.

motherboard, transferred through two-pin LEMO cables. Because the cable has the orientation, red marks on the male and female connectors have to be aligned and plugged. In order to initialize the devices and set up internal parameters, a LVDS high density 68pin cable has been connected between the XLMXXV and the ASICs motherboard. Also, the FPGA in the XLMXXV communicates with the ASICs chips through this cable during the data acquisition. The ASICs power supply is designed to support 6 motherboards and it has a voltage meter and a current meter as well as an adjustable knob to change the +6 V output for each motherboard. It is possible that the +6 V drops on the cable and the voltage has to be adjusted in

order to give enough power to the motherboard. It is recommended to set 6.5 V to keep the voltage above 6 V on the motherboard. If the voltage is too high ($\sim$ 7 V), then the voltage regulator IRLZ34N may overheat and a caution is required.

A.3.2 Cable setup for XLM trigger signals

As shown in Figure A.1, triggers from all motherboards have to be combined appropriately to fire all XLMXXV to read and store energy shaped signals in their memories. Figure A.5 shows a detail cable setup for the XLM trigger signal. Trigger signals from pin No. 3 of the 34pin connector in the XLMXXV are duplicated by FAN I/O NIM module ("FAN I/O 1" in the figure). One output is used to combine trigger signals of all motherboards while another is used as a scaler input. Another FAN I/O module combines all of trigger signals ("FAN I/O 2" in the figure). In the meantime, XLMXXVs produce a "XLM ready signal", which indicates the module is not busy and available to be fired. One can invert the signals ("$\overline{\text{OUT 1}}$" in the figure) and use them to veto the combined trigger signals in order to prevent firing XLMXXV when the module is working ("LOGIC I/O 1" in the figure). A test shaping signal for a selected channel by ASICs software, SetCHIP, can be diagnosed from pin No. 7 of the 34pin connector ("SHAPE test" in the figure). This output, however, must be turned off during the data acquisition. Table A.3 shows a list of signals in ECL 34pin connector on the XLMXXV. A XLM Always true signal on ECL No. 8 is a constant -1 V signal, which can be produced by $\overline{\text{OUT}}$ output with no input signals in any FAN I/O module.

A.3.3 Cable setup for VME trigger signals

After the XLMXXV finishes the signal processing, it generates a new trigger, called "VME trigger", for the DAQ system to read the data and send it to the computer. Again, the VME trigger signal of each XLMXXV has to be combined altogether and fire the VME I/F module when the module is not busy. Figure A.6 (a) shows the
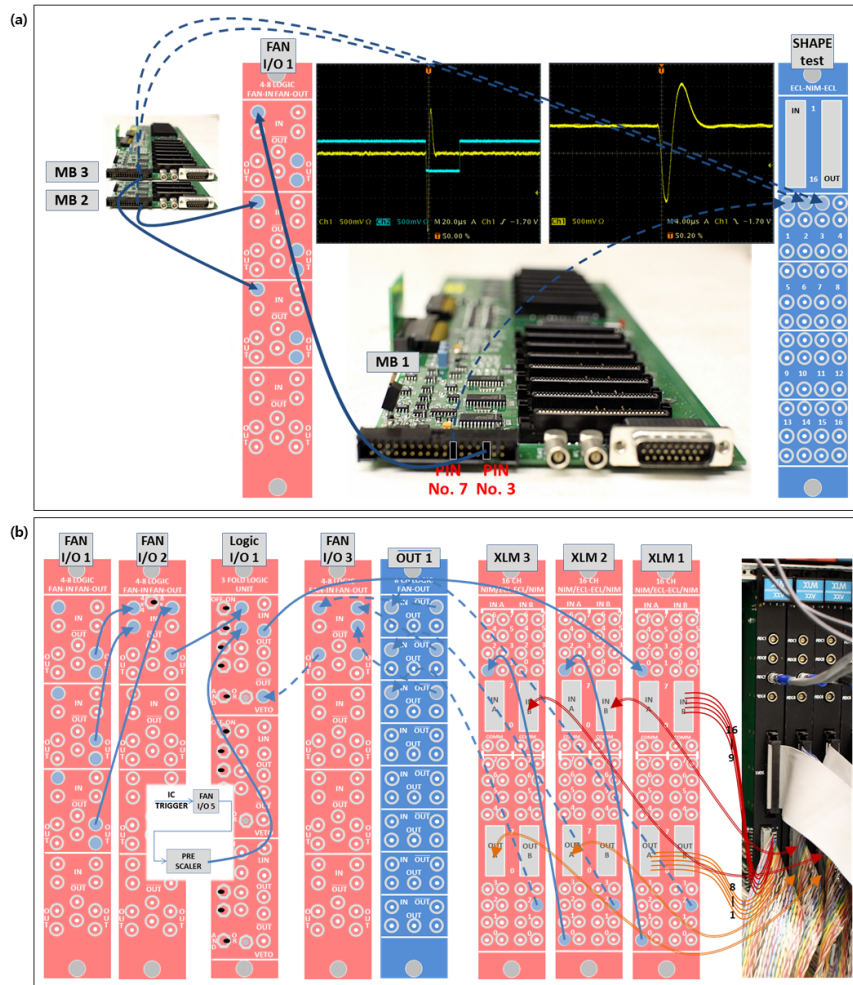
Figure A.5: Cable setup for XLM trigger signal. (a) Triggers and test shaping signals from 34pin connector of each motherboard. Blue solid lines represent trigger signals and blue dash lines show test shaping signals. The trigger signals are -1 V logic signals (blue waveform in the left oscilloscope screen) while the test shaping signals have bipolar Gaussian shapes (yellow waveform in the right oscilloscope screen). (b) XLM trigger signals are produced by combined triggers in FAN I/O 2 with a veto of XLM busy signals. Labels on top of modules are the same as one used in Figure A.1.
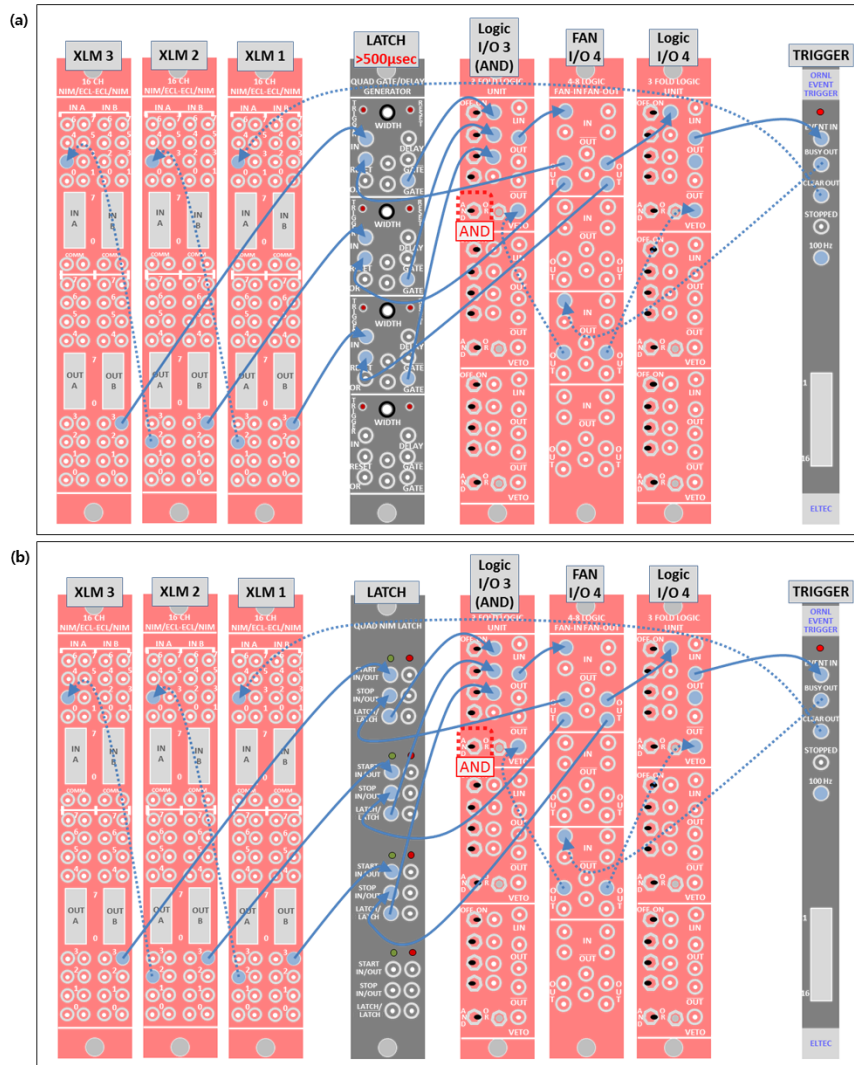
Figure A.6: Cable setup for VME trigger signal using the Gate and Delay Generator module (a) or using the LATCH module (b).

Table A.3: Output list of ECL 34pin connector on the XLMXXV

ECL No.	NIM/ECL No.	From	To	Description
1	IN 0	MB	XLM	XLM trigger signal
2	IN 1	N/A	N/A	N/A for XLMXXV
3	IN 2	VME	XLM	VME Complete signal
4	IN 3	N/A	N/A	N/A for XLMXXV
5	IN 4	N/A	N/A	N/A for XLMXXV
6	IN 5	N/A	N/A	N/A for XLMXXV
7	IN 6	N/A	N/A	N/A for XLMXXV
8	IN 7	FAN $\overline{\text{OUT}}$	XLM	XLM Always true signal
9	OUT 0	XLM	FAN I/O	SIS Clock signal
10	OUT 1	N/A	N/A	N/A for XLMXXV
11	OUT 2	XLM	FAN I/O	XLM ready signal
12	OUT 3	XLM	VME	XLM complete signal

cable setup for the VME trigger signal. A XLM complete signal (ECL No. 12) from the XLMXXV is latched by the Gate and Delay Generator (GDG) NIM module (LATCH in the figure), until all XLMXXVs produce the XLM complete signals. A latch signal has to be -1 V logic signal. The width of the gate has to be long enough (> 500 μsec) as the latch signal. Once all of trigger signals are fired, a VME trigger signal selected by AND gate and a reset signal are produced by a LOGIC I/O NIM module ("Logic I/O 3 (AND)" in the figure) to turn off all latch signals. A NSCL NIM latch module can be used to make the trigger signals to the latch signals instead of the GDG NIM module as shown in Figure A.6 (b). The module produces a real latch signal with a "Start IN" from each VME trigger signal and turns off the latch signal by "Stop IN" from the reset signal.

A.3.4   Cable setup for scaler signals

Counting the number of various trigger types in the system is useful to estimate system deadtime, the total number of events, and beam rates, and so on. This task can be performed by a scaler counting the number of input signals. The CAMAC Model 2551 scaler provides 12 identical 24-bit scalers. 100 Hz Clock signals form the ORNL EVENT Trigger module give a time reference for other scaler inputs, and
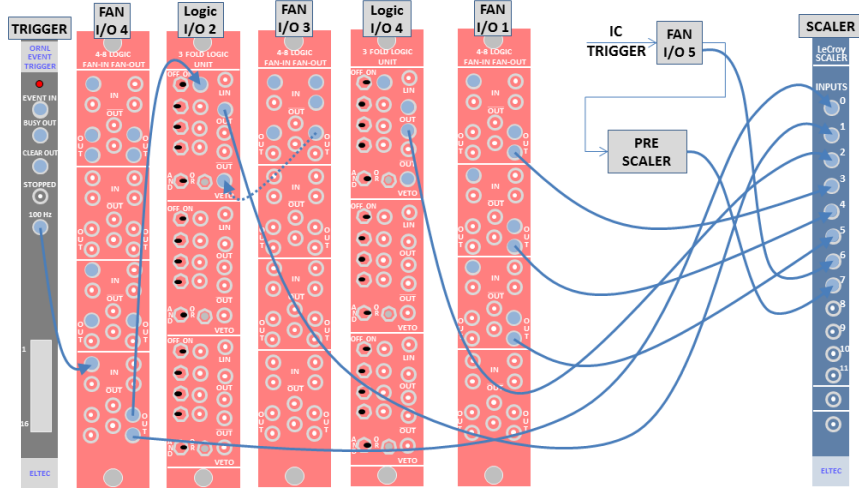
Figure A.7: Cable setup for Scaler signal. The 100 Hz Clock signals are counted in INPUT 0 of the scaler and used to scale counts of other input signals. The number of INPUT on the front panel of the scaler is the same as the one in Figure A.1.

then the clock signals vetoed by the system busy are counted for the lifetime of the system as shown in Figure A.7. Counts of event trigger signals, XLM trigger signals for each motherboard and ionization counter (IC) trigger signals are scaled by the 100 Hz Clock signals to provide their values in the unit of time.

A.3.5   Cable setup for a detector and preamplifier box

As mentioned in Section 3.3.1 and 3.4.2, the ORNL DAQ ASICs system is developed for the signal processing of ∼ 2000 channels for the SuperORRUBA array. Due to the high density of channels, the connection between the detector and the electronics system is also complex and the order of channels can easily be misread, so some figures of the cable setup between them is helpful. Figure A.8 shows how to connect cable between the detector and the preamplifier box. 40pin high-density flat ribbon cables are used to transfer signals and biases for the detector. A detail pin map of the connectors is shown in Figure A.9. A description of the preamplifier box can be found in Reference [63]. It should be noted that the cable connected to the bottom side of the preamplifier box (labeled as "Preamp Bottom" in the figure)

119
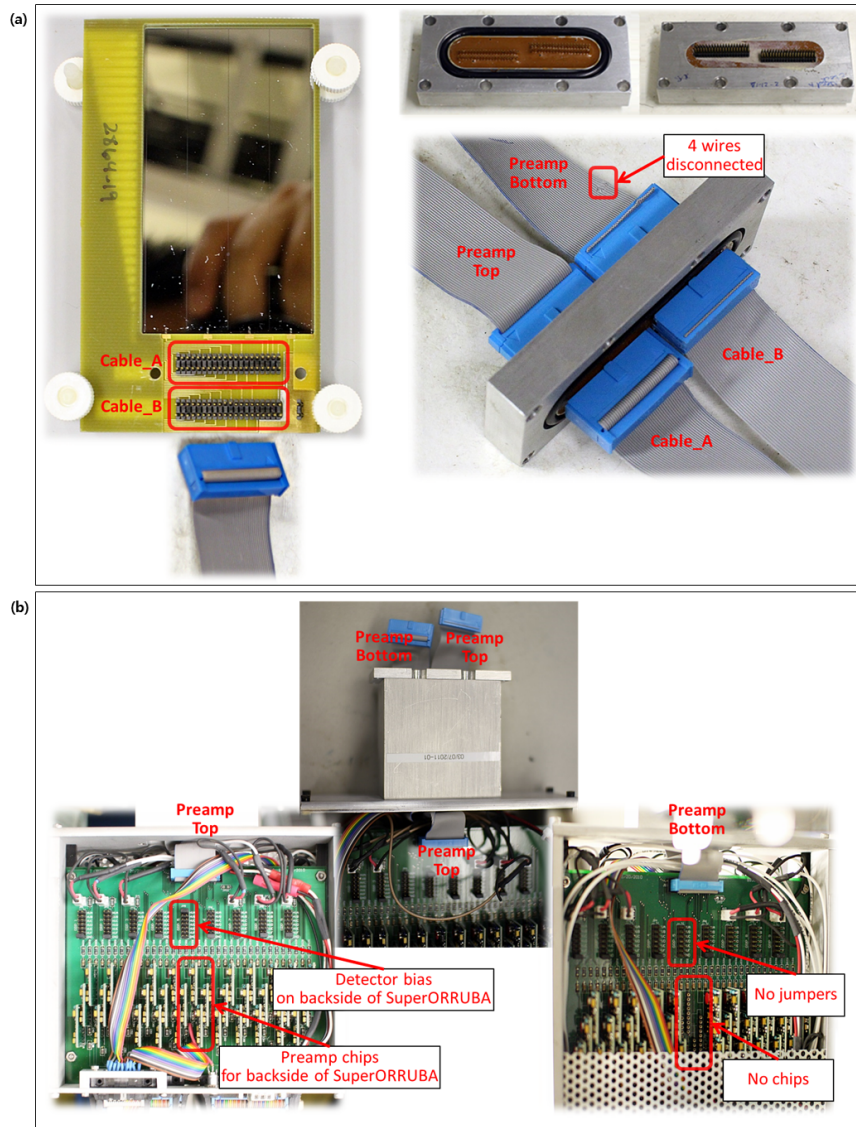
Figure A.8: Cable setup for SuperORRUBA detector and preamplifier box. (a) A SuperORRUBA detector (left) has two 40pin high-density connectors on the backside. A feedthrough (top right) also includes two sets of 40 jumper pins to interconnect inside and outside the vacuum chamber. The channel number order will be swapped at the feedthrough. (b) Top (left) and bottom (right) of the preamplifier box can be identified by bias jumper pin JP5 and preamp chips on slot 17-20 (middle 4 slots).

must have the last four wires disconnected to disable connection of preamp channels to the guard rings in the detector. Also, it is recommended to connect the backside channels of the detector to the top side of the preamplifier box in order to use a short cable transferring amplified signals to the output connector and to avoid cross talk between the cable and preamp chips placed near the cable.

Assuming cable connections are conducted as recommended above, Figure A.10 (a) shows the order of the channel number, corresponding to the detector strip number, on output connectors. Since each ASICs chipboard covers 32 channels, two chipboards are required to process signals from 64 frontside strips of the detector as shown in Figure A.10 (b). It should be noted that the order of channels on the Cable_F2 and the Cable_F4 are inverted as the order on the ASICs input connector shown in Figure A.2. Thus, this has to be corrected in the data analysis software, called SCANOR. For example, the user can insert such a below statements in the SCANOR file:

```
! this should be inserted after reading buffer as:
!        id = evbuf(1,i)      ! parameter
!        ix = evbuf(2,i)      ! channel (energy)
! Variables such as det, strip and maxid has to be defined as integer data
   type.
! The variable maxid has to be changed to the last id.
        maxid = 1865
        if (id.lt.maxid) then
          det = INT(id/100) + 1
          strip = id - (det-1)*100
          if(strip.ge.17.and.strip.le.32) then
            strip = 49-strip
          elseif(strip.ge.49.and.strip.le.64) then
            strip = 113-strip
          endif
          id = (det-1)*100+strip
        endif
```

For a backside connector, four pins are only used because the SuperORRUBA has four backside strips. A special cable has been made to combine channels of 4 detectors into one 34pin flat ribbon cable, and two of the cables are plugged in one
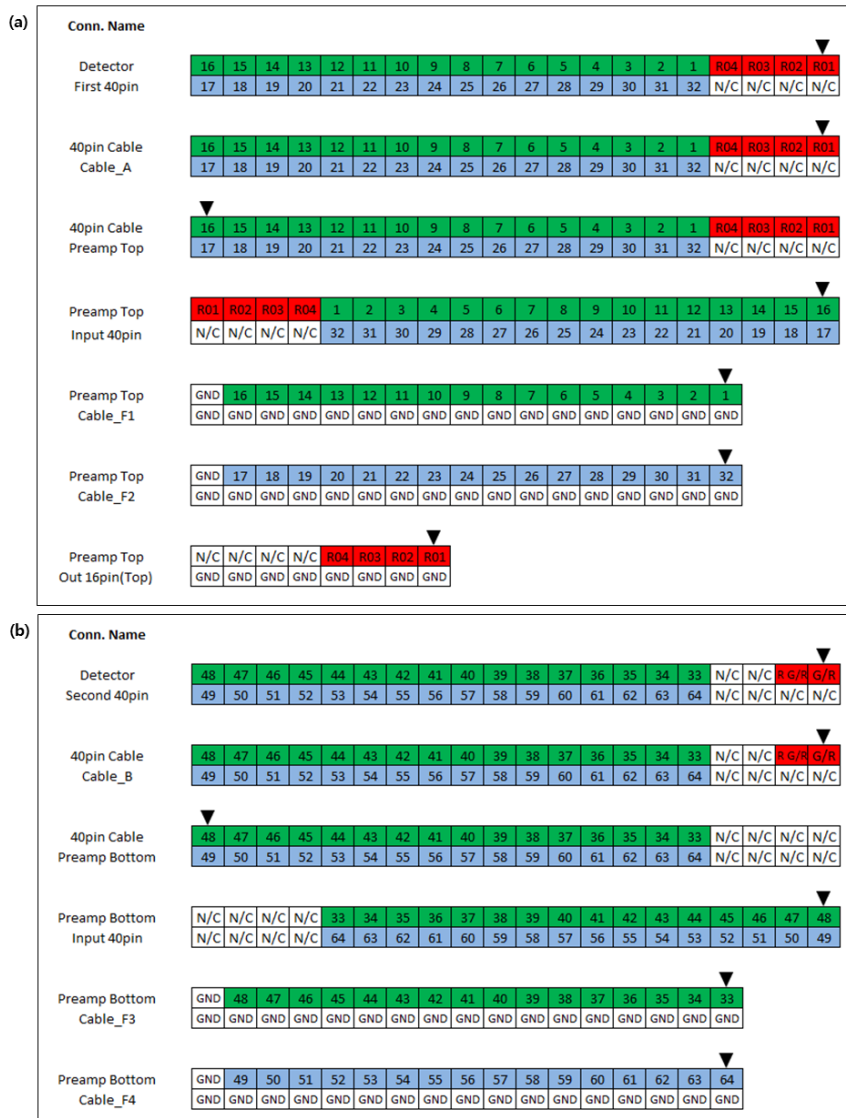
Figure A.9: A detail pin map of connectors on the detector and the preamplifier box. (a) First 40pin connector, Cable_A, Preamp Top, Cable_F1, Cable_F2 and 16pin connector. (b) Second 40pin connector, Cable_B, Preamp Bottom, Cable_F3 and Cable_F4. A number in the square box represents frontside strip number of the detector. R01, R02, R03 and R04 are backside strip number of the detector. G/R and R G/R are frontside guard ring and backside guard ring, respectively. Green boxes and blue boxes represents a group of 16 frontside strips corresponding to the output of the preamplifier box. A pin number of the connector or cable starts with a key mark (reversed triangle).
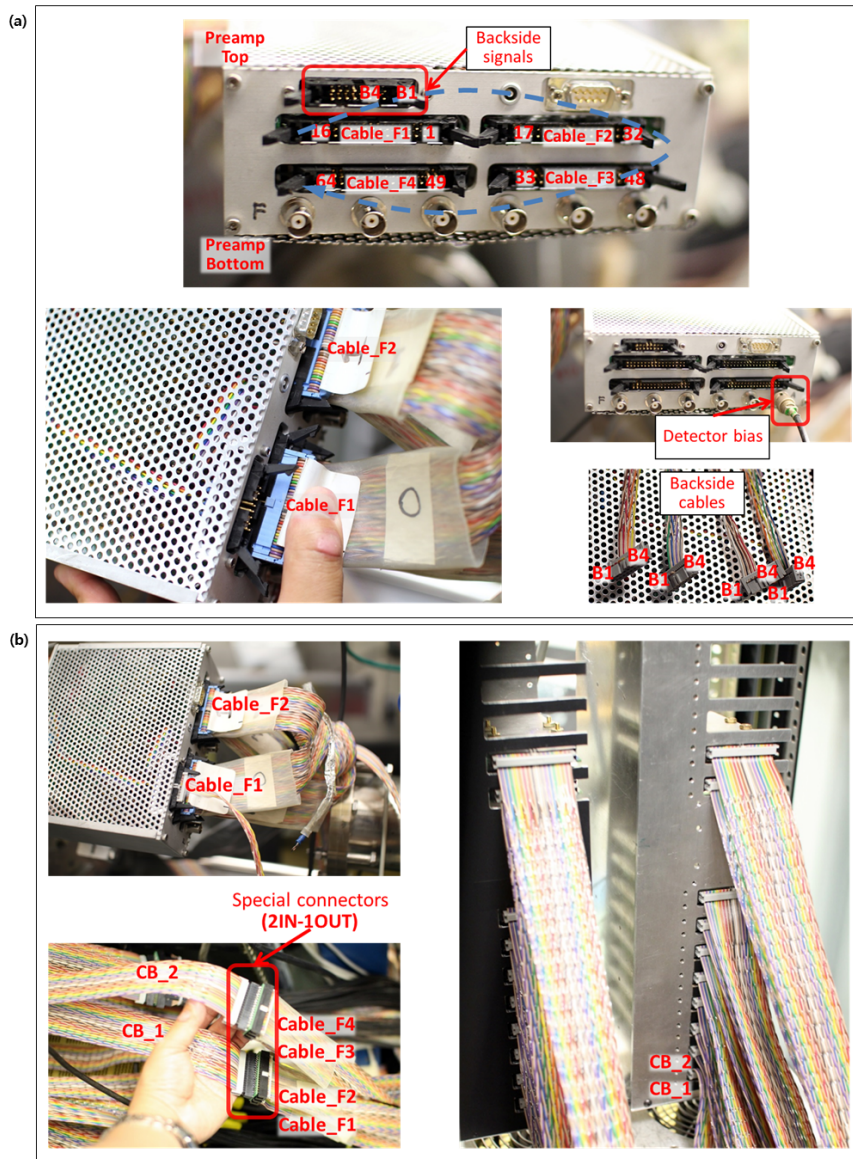
Figure A.10: Cable setup for SuperORRUBA preamplifier box and ASICs motherboard (a) shows the order of cables to match order of the detector strips and the picture of special cable for backside strips. (b) shows how to connect two 34pin flat ribbon cables to the ASICs chipboard. There is a special connector, called 2IN-1OUT, applied to combine signal pins of two 34pin connectors into pins of one 34pin connectors.

ASICs chipboard resulting in backside signals from 8 total detectors handled in one chipboard.

As mentioned in Section A.3.1, there is an ADC channel number inversion between negative polarity setup and positive polarity setup. While the new chipboard provides the energy output reversed with jumpers, confusion can still exist due to the use of a mixture of old chipboards and new chipboards with the difficulty that the user has to remember the rule. Alternatively, this can be corrected in the SCANOR file:

```
! this should be inserted after reading buffer as:
!        id = evbuf(1,i)     ! parameter
!        ix = evbuf(2,i)     ! channel (energy)
! Variables such as det, strip and maxid has to be defined as integer data
   type.
! The variable maxid has to be changed to the last id.
        if (id.lt.maxid) then
          det = INT(id/100) + 1
          strip = id - (det-1)*100
          if(strip.ge.65.and.strip.le.68) then
            ix = 16384-ix
          endif
        endif
```

In order to supply a large amount of power ($\sim$ 30 A) for 19 preamplifier boxes designed for the full SuperORRUBA array, a tower of preamp power supplies was developed (Figure A.11 (a)). The tower consists of four preamp power supplies having 10 output ports with $\pm$12 Vdc and 8.5 A max shown in Figure A.11 (b). In practice, a maximum of 5 preamplifier boxes can be plugged to one preamp power supplier due to the large power load of each preamplifier box.
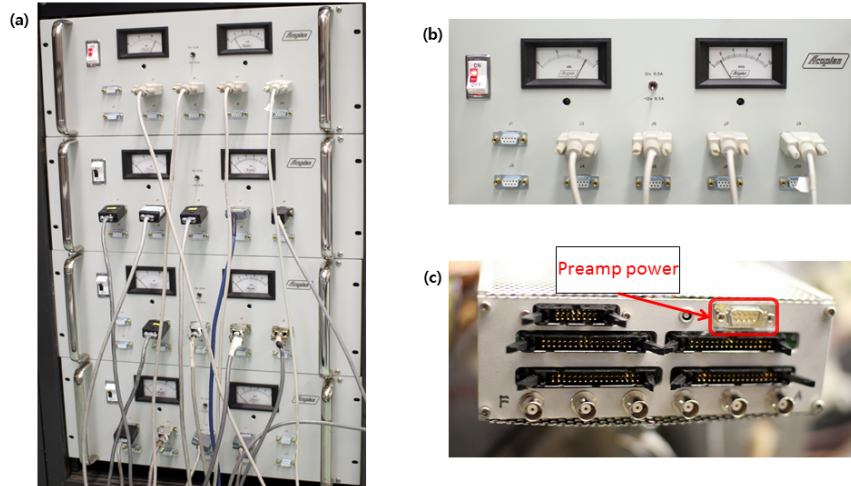
Figure A.11: Power cable setup for SuperORRUBA preamplifier box (a) A preamp power supply tower. (b) A front panel of each preamp power supplier. (c) the preamplifier box power connector.

A.4 Software Setup

As mentioned in Section 3.4.2, the ASICs software package are developed to initialize and set up parameters on the ASICs devices. Preparation steps before the data acquisition are as follows:

1. To turn on the VMEbus crate having the MVME5500 VME I/F module.

2. The MVME5500 connects to the TFTP server, downloads a firmware and boots up the RTEMS system (see Section 3.4.2).

3. To reset all of bus control in the XLMXXV by the Reset command.

4. To load a firmware and boot the FPGA in the XLMXXV by the LoadFPGA command.

5. To initialize the ASICs motherboard and the ASICs chipboards by the InitCHIP command.

6. To set up parameters for the ASICs motherboard and the ASICs chipboard by the SetCHIP command.

7. The ASICs system is ready to take data.

The current release of the ASICs software distribution package is version 4.0 and it includes:

1. A firmware for the MVME5500 (vmeacq_v4.0)
2. A modified HRIBF DAQ software working with the ASICs system
3. ASICs softwares (Reset, LoadFPGA, InitCHIP and SetCHIP)
4. ChipCommander V3.0
5. A firmware for the FPGA in XLMXXV (xlmxxv_rev273.bit)
6. Example setup files and scanor files

A firmware for the MVME5500 has to be copied to TFTP server home directory before the module is powered on. Source codes for the listed programs are also provided in the package and it is recommended to compile the source codes and install executables for their correct operations.

A.4.1   Installation

The HRIBF DAQ software has been modified to include functions of the ASICs system, and the modified codes are distributed with the ASICs software source files. In order to use the ASICs system, therefore, an installation of the customized HRIBF DAQ software is necessary.

Assuming the source file "ornl-asics-4.0.tgz" is provided, the programs can be installed by commands:

```
[drs1@asics ~]$ tar -xvzf ornl-asics-4.0.tgz
[drs1@asics ~]$ cd v4.0/
[drs1@asics v4.0]$ ./asicssetup.sh
[drs1@asics v4.0]$ # Below commands will copy a MVME5500 boot image to
    /home/tftpboot/
[drs1@asics v4.0]$ cd ./server/rtems/vmeacq/
[drs1@asics vmeacq]$ make install
[drs1@asics vmeacq]$
[drs1@asics vmeacq]$ # Below commands will compile the modified HRIBF DAQ
    software
[drs1@asics vmeacq]$ cd ../../acqlib/
[drs1@asics acqlib]$ make clean;make;make install
```

```
[drs1@asics acqlib]$ cd ../ipclib/
[drs1@asics ipclib]$ make;make install
[drs1@asics ipclib]$ cd ../vmelib/
[drs1@asics vmelib]$ make clean;make;make install
[drs1@asics vmelib]$ cd ../vmexxlib/
[drs1@asics vmexxlib]$ make clean;make;make install
[drs1@asics vmexxlib]$ cd ../Dacq/
[drs1@asics Dacq]$ ./makeall
[drs1@asics Dacq]$ cd pacor/
[drs1@asics pacor]$ make;make install
[drs1@asics pacor]$ cd ../../pacman/
[drs1@asics pacman]$ make;make install
[drs1@asics pacman]$ cd ../scad/
[drs1@asics scad]$ make clean;make;make install
[drs1@asics scad]$ cd ../scop/
[drs1@asics scop]$ make clean;make;make install
[drs1@asics scop]$ cd ../tape/
[drs1@asics tape]$ make clean;make;make install
[drs1@asics tape]$ cd ../utptoipc/
[drs1@asics utptoipc]$ make clean;make;make install
[drs1@asics utptoipc]$ cd ../vmereset/
[drs1@asics vmereset]$ make clean;make;make install
[drs1@asics vmereset]$ cd ../vmeterm/
[drs1@asics vmeterm]$ make clean;make;make install
[drs1@asics vmeterm]$ # You must be a sudoer to run a below command.
[drs1@asics vmeterm]$ sudo ln -sf $HOME/asics /usr/acq2
[drs1@asics vmeterm]$
[drs1@asics vmeterm]$ # Below commands will compile ASICs softwares
[drs1@asics vmeterm]$ cd ../../client/
[drs1@asics client]$ make clean
[drs1@asics client]$ make
[drs1@asics client]$ make install
```

If no errors are produced, the programs will be installed in the directory $(HOME)/bin/asics. If any errors occured, the Makefile has to be reviewed to make sure all of compiling information are correct. Installed programs are Reset, LoadFPGA, InitCHIP and SetCHIP. All of the programs are used to control the XLMXXV, the ASICs motherboard and the ASICs chipboard before the data acquision. The HRIBF DAQ softwares such as PACMAN, PACOR, SCANOR, SCAD and TAPE are installed and used to run the data acquisition. How to run the data acquition will be discussed in Section A.5.

The Graphic User Interface version of the SetCHIP program, called
ChipCommander, can be excuted by commands:

```
[drs1@asics ~]$ cp v4.0/client/ChipCommander_3.0/ChipCommander.jar .
[drs1@asics ~]$ java -jar ChipCommander.jar
```

, or simply:

```
[drs1@asics ~]$ goasics
```

The ChipCommander provides easy controls of setup parameters and explicit names
of most parameters. The current release of the ChipCommander is the version 3.0.

A.4.2   Preparation of necessary files

Before the ASICs system runs, it is recommended to create a new directory and
copy necessary files from the distribution package to start up the system. This can
be done with commands:

```
[drs1@asics ~]$ mkdir /nfs_data/drs1/asicsmanual
[drs1@asics ~]$ cd /nfs_data/drs1/asicsmanual
[drs1@asics asicsmanual]$ cp ~/v4.0/client/xlmxxv_rev273.bit .
[drs1@asics asicsmanual]$ cp ~/v4.0/client/setup_files/mb01.setup .
[drs1@asics asicsmanual]$ cp ~/v4.0/client/setup_files/mb02.setup .
[drs1@asics asicsmanual]$ cp ~/v4.0/client/setup_files/mb03.setup .
```

The file "xlmxxv_ref273.bit" is a boot image for the FPGA in the XLMXXV. The
FPGA works as a commander to control all of ASICs devices all the time.
The file with an extension of "setup" includes all of parameters for the ASICs
motherboard and ASICs chipboards. The user mostly keeps the value of parameters
except some frequently varying parameters marked by * in Table A.4. While the
user can change the offset of each chip boards by the EOffset parameter, it was
found that offsets of each channels in one chip boards are varied but they were net
adjustable individually.

Table A.4: List of setup parameters. The parameter names with * are the one being frequently varied for each experiment. Values are recommended ones for a reference.

Device	Param. Name	Function	Polarity	Value
MB	Routing_MB*	Selection of XLM trigger output (0=Off, 1=OR_A, 2=OR_B, 3=OR_C, see Table A.1)		1
	SumOffA	Offset for Sum of Multiplicity outputs from selected chipboards (see Table A.1)		0
	SumOffB	Offset for Sum of Multiplicity outputs from selected chipboards (see Table A.1)		0
	SumOffC	Offset for Sum of Multiplicity outputs from selected chipboards (see Table A.1)		0
	SISDelay	Time between ACQ_ACK and SIS_CLK		3360 ns
	AcqDelay	Time between GLBL_DSBL and ACQ_CLK		120 ns
	PauseDelay	Time between Data Write on XLMXXV and Next ACQ_CLK		160 ns
	CycleTimeout	Time to receive a signal after the ACQ_CLK		25520 ns
	GlobalTimeout	Total time to read data from the motherboard		25520 ns
	TriggerDelay	Time between XLM trigger and GLBL_DSBL		3000 ns
	CoincidenceWindow	Time of the discriminators staying alive after the first channel triggers		1728 ns
	ForceTrackDelay	Time between ACQ Start and FORCE_TRACK		0 ns
	AcqAllDelay	Delay time for ACQ_ALL itself		0 ns
	GlobDisDelay	Delay time for GLBL_DSBL itself		0 ns
Chip	Gain	Internal CSA gain ("e" for external setting)		e
	TVCRange	Time range to stop the TVC circuit. 500 ns (s) and 2 μs (l)		l
	Shaper	Shaper Internal/External (for shaping inspection output only)		i
	CSARef	Voltage for the input device of the CSA		900
	ResetCV	The autoveto time		256 ns
	EOffset*	Offsets to the Time signals to bring into range of the ADC	Pos	445
			Pos	566
	TOffset	Offsets to the time signals to bring into range of the ADC		755
	CFDCap	CFD Capacitance for the time constant in the fast shaper		12 μF
	CSAOffset	Offset for the inspection outputs for the CSA		444
	Polarity*	Signal polarity before the CSA	Pos	p
			Neg	n
	DiscMode	Discriminator mode ("a" for all, "s" for selected channel and "m" for masked channels only)		a
	DiscMask	Discriminator mask bits (32bit with the first MSB taken by sign flag)		256
	ARef	Voltage offset for Analog reference circuit		512
	ZC2	Midpoint voltage for the zero crossing detection of the CFD		420
	DACRef	Midpoint voltage for the threshold DAC		430
	CFDRef	Voltage offset of the CFD		432
	ShapOffset	Offset for the inspection outputs for the Shaper		404
	Threshold*	Threshold of Discriminator	Pos	−32
			Neg	+32

Once all of parameters are corrected, the setup file is ready to be sent out to the ASICs devices and all devices are in normal mode.

For the HRIBF DAQ software, the files are the same as the conventional electronics system except a PAC file. The PAC file (*.pac) is required to assign VME modules such as XLMXXV and CAEN V785 ADC and map the channel number of the

device to the global channel number, called PAC ID. The SCAD file (*.sca) is necessary to use a SCALER module scaling inputs with a reference clock. In order to analyze event data and make desired histograms, the SCANOR file (*.f, usually called SCAN code) is also required. The detail description how to use the file is mentioned in Section A.5.

Here are some examples of necessary files. It should be noted that statements for the XLMXXV module must be written before statements of the CAEN V785 ADC module in the PAC file.

[In PAC file] - assuming a file name is asicsmanual.pac,

```
;Time between VME trigger and start reading modules
$dla uncondit  20

;[ASICs Setup]
;SuperORRUBA
;The first two chipboards used for frontside strips.
;The third chipboard connected used for backside strips.
;fronts
$vme xlm01 a01-32 id1,1 mt=XLM-XXV
$vme xlm01 a33-64 id33,1 mt=XLM-XXV
$vme xlm01 a65-96 id101,1 mt=XLM-XXV
$vme xlm01 a97-128 id133,1 mt=XLM-XXV
;backs
$vme xlm01 a129-132 id65,1 mt=XLM-XXV
$vme xlm01 a133-136 id165,1 mt=XLM-XXV

;[CAEN V785 ADC Setup]
;Ionization Counter
$vme adc1 a01-01 id600,1 mt=CAEN-785
$vme adc1 a02-02 id601,1 mt=CAEN-785
;TAC
$vme adc1 a03-03 id602,1 mt=CAEN-785

;32bit time stamp for events
$cid 701 702
```

[In SCAD file] - assuming a file name is asicsmanual.sca,

```
;Name <Crate No.> <Slot No.> <Channel No.>
Time 6 20 0 ; NOR 100
```

```
Live 6 20 1
EVENT 6 20 8
SORRUBA 6 20 2
IC 6 20 7
IC_PS 6 20 9
$END
```

A.5　How to Run the System

As mentioned in Section A.4, there are several commands need to be done after the MVME5500 is booted up. For example, motherboard No. 1 and XLMXXV No. 1 are loaded by:

```
[drs1@asics asicsmanual]$ # Reset <XLMXXV No.>
[drs1@asics asicsmanual]$ Reset 1
[drs1@asics asicsmanual]$ # LoadFPGA xlmxxv_ref273.bit <XLMXXV No.>
[drs1@asics asicsmanual]$ LoadFPGA xlmxxv_ref273.bit 1
[drs1@asics asicsmanual]$ # InitCHIP <motherboard No.>
[drs1@asics asicsmanual]$ InitCHIP 1
[drs1@asics asicsmanual]$ SetCHIP <setup file> <motherboard No.>
   [<selected chipboard No.> <selected channel No.> <Switch for test
   output> <switch for force-read>]
[drs1@asics asicsmanual]$ SetCHIP mb01.setup 1 1 0 n
```

The brackets [ ] indicates optional arguments and default values are "1 0 n n". The above commands have to be done for the first setup, while the last command SetCHIP can be executed for the change of the parameter values. Once the ASICs power is reset, the commands InitCHIP and SetCHIP has to be conducted.

It is recommended to use ChipCommander V3.0 to change values of parameters as shown in Figure A.12.

It is important to make sure the ASICs system is working correctly before the user starts taking data. This can be done by checking XLM trigger signals or shaping test outputs. The ASICs chipboards fire XLM triggers for any input signals above the threshold. And, by turning on the switch for test output in SetCHIP command

Figure A.12: ChipCommander V3.0 includes functions of open setup file (a), send the file to the XLMXXV and motherboard (b), save the current parameter values (c) and find help on the website (d).

or in Basic Tab of the ChipCommander program, the user can examine if the input signals are processed correctly.

After all of inspections are completed, the user can take data using the HRIBF DAQ programs. When the user run PACMAN by the command "pacman", additional TERMINAL windows are automatically created as shown in Figure A.13. Below are shown examples of the steps to take data. It should be noted that a last command in the PACMAN such as "startvme", "trun bon" and "trun boff" are the ones to start the data acquisition process, so other previous steps have to be done before the user execute the command.

[In PACMAN window] - assuming asicsmanual.pac file exists,

```
[drs1@asics asicsmanual]$ #export VME=<vme No. of VME I/F>
[drs1@asics asicsmanual]$ export VME=vme54
[drs1@asics asicsmanual]$ export EXPT=TEST
[drs1@asics asicsmanual]$ pacman
....................................
```
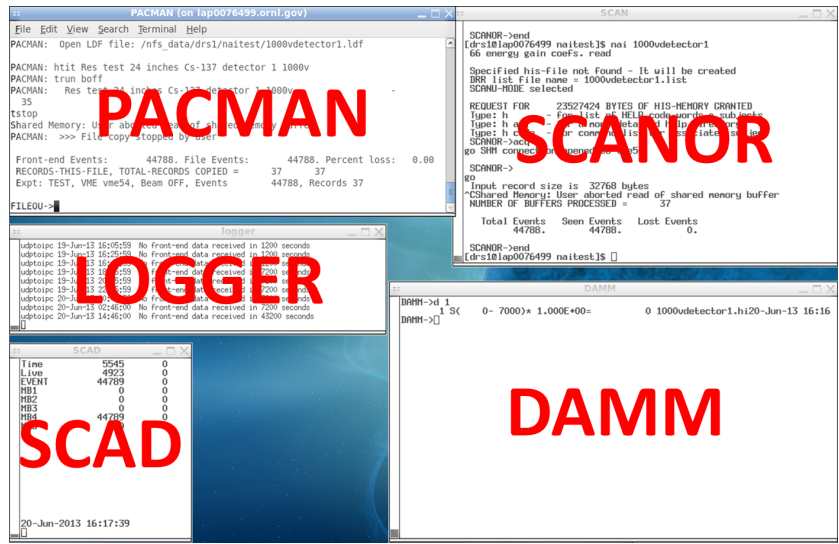
Figure A.13: TERMINAL windows created by the PACMAN program. These five windows are necessary to take data in the ORNL DAQ system.

```
.....................................
Type: H SCAT - For Scaler-to-File related commands
Type: H VME - For commands to control and get status of Front-End
Type: H ACQ - Commands related to data acquisition
Type: H FILE - For File control commands
Type: H DISP - For commands which display Data-records
Type: H STAT - Commands to display system status and test VME system
Type: H MISC - Miscellaneous Commands
Type: H EXIT - How to STOP the acquisition system
Type: H CMDS - Command list
Type: H NEW - How to update Help messages
Pacman: pacor asicsmanual l
 #BYTES OBJECT CODE GENERATED = 26808
 CONSIDER YOURSELF LOADED WITH 26808 BYTES
 NO ERRORS
Pacman: zbuf
Pacman: zeroclk
Pacman: scat asicsmanual.sca
Pacman: FILEOU->scat on
#When other programs are ready.
Pacman: startvme
#In order to stop taking data.
Pacman: stopvme
```

[In SCAD window] - assuming asicsmanual.sca exists,

```
[drs1@asics asicsmanual]$ #export VME=<vme No. of VME I/F>
[drs1@asics asicsmanual]$ export VME=vme54
[drs1@asics asicsmanual]$ scad
Enter snit-filename for tabular display->asicsmanual.sca
 Type: h      - for list of HELP code-words & subjects
 Type: h all  - for a more detailed help directory
 Type: h code - for command list for associated subject
SCAD->zero
SCAD->sec 1
SCAD->run
Time          4054  100.00
Live          3903  98.0392
EVENT        11730  289.22
SORRUBA          0       0
IC               0       0
IC_PS            0       0
```

[In SCAN window] - assuming Makefile and asicsmanual.f exist,

```
[drs1@asics asicsmanual]$ #export VME=<vme No. of VME I/F>
[drs1@asics asicsmanual]$ export VME=vme54
[drs1@asics asicsmanual]$ more Makefile
...................................
...................................
asicsmanual: $(DIRA)scanor.o $(LIBSC) asicsmanual.f
        g77 -O2 -o asicsmanual asicsmanual.f $(DIRA)scanor.o $(LIBSC) $(LDF)

[drs1@asics asicsmanual]$ make asicsmanual
g77 -O2 -o asicsmanual asicsmanual.f /usr/hhirf/scanor.o
   /usr/hhirf/scanorlib.a /usr/acq2/lib/acqlib.a /usr/hhirf/orphlib.a
   /usr/acq2/lib/ipclib.a

[drs1@asics asicsmanual]$ asicsmanual histo001
...................................
...................................
 Specified his-file not found - It will be created
 DRR list file name = histo001.list
 SCANU-MODE selected

 REQUEST FOR   45481984 BYTES OF HIS-MEMORY GRANTED
 Type: h      - for list of HELP code-words & subjects
 Type: h all  - for a more detailed help directory
 Type: h code - for command list for associated subject
 SCANOR->acq
```

```
SHM connection opened to vme54
SCANOR->go
```

[In DAMM window] - assuming cmapr.dat exists,

```
[drs1@asics asicsmanual]$ damm
Type: h      - for list of HELP code-words & subjects
Type: h all  - for a more detailed help directory
Type: h code - for command list for associated subject
DAMM->cmap cmapr.dat
DAMM->revv
DAMM->fig 17
DAMM->in histo001.his
Memory Map the HIS file Segment:histo001.his
DAMM->d 1
DAMM->d 1
    1 S(    0- 2047)* 1.000E+00=        0 histo001.his   17-Jun-13 18:02
DAMM->dd 100
MIN=          0
MAX=          2
SUM=          0
 ID=        100
DAMM->
```

The user can store events in a file (*.LDF) by:

[In PACMAN window]

```
Pacman: zbuf
Pacman: zeroclk
Pacman: scat asicsmanual.sca
Pacman: scat on
Pacman: ouf /nfs_data/drs1/asicsmanual/datafile001.ldf
Pacman: Open LDF file: /nfs_data/drs1/ge80dpasics/datafile001.ldf

Pacman: htit "Example Event data with ASICs system"
# hnum <run No.>
Pacman: FILEOU->hnum 1
#When other programs are ready.
# ''boff'' with no beam and ''bon'' with beams
Pacman: trun boff
FILEOU->Pacman: PAC file: /nfs_data/drs1/ge80dpasics/asicsmanual.pac  -
         999001
  "Example Event data with ASICs system"                   -           1
```

```
#In order to stop storing events in the file
Pacman: tstop
```

At the end of the day, the user can exit the PACMAN program by the command "KILL ALL". Then, all related programs are automatically terminated and the cursor goes back to the terminal console mode.

A.6   Trouble Shooting

As seen Section A.3, A.4 and A.5, troubleshooting the ASICs system is not always easy, since there are many pieces involved in running the system. If any of them aren't right, the system can fail. Also, one cannot trace all of the signals step by step, so it is difficult to find out where the problem is. They are from, for example, the power on the motherboard, the buscontrol failure in the XLMXXV, the physical connection to the devices, the firmware on the XLMXXV, and more. Here are some specific suggestions for troubleshooting each of the pieces.

Before any inspection begins, the quick and easy way is a system restart. Restarting devices can resolve issues like a frozen system.

1. Turn off switches on the ASICs power supply and turn them back on after waiting ~10 seconds.
2. Make sure a LED on the motherboard blink one second as the power turned on
3. Turn off switches on the VMEbus crate and turn them back on after waiting ~10 seconds.
4. Wait ~1 minute for the VME I/F to boot up with a firmware.
5. Reload all necessary files.

A.6.1   No LED blinking on the motherboard

This is possible when the proper voltage is not loaded on the motherboard. If it is the case, then some parts are not working correctly. Call the manufacturer.

A.6.2   No XLM triggers from the motherboard

Two possibilities are threshold is too high and fast shaper in the chip is broken.

1. Check signals on input cable and make sure the signal polarity is correct.

2. Turn on test output using SetCHIP command and look at shaping test output if it looks okay (see Figure A.5).

3. Minimize the value of the discriminator threshold (Threshold in the setup file) to $+32$ for pos. polarity and -32 for neg. polarity. And find the proper value if the triggers are shown.

4. Adjust offset voltage parameters for CFD circuit (ZC2, DACRef and CFDRef). It is recommended to record the original values before they are changed.

There are more solutions about troubleshootings in the ASICs blog [97], and it will keep updating as more problems and solutions are found. Also, the author (Tony Ahn) of this manual is always welcome to help any troubles related to the ASICs system by email (saint@nuclearemail.org).

Vita

Sunghoon Ahn was born in Yesan, Korea (Republic of) on June 15, 1978. After completing high school at Hanil high school in 1997, he attended Hanyang University in Korea (March 1997 - February 2004), where he received his Bachelor of Science (B. S.) degree in Physics. During that period, he served in the 122nd Signal Battalion of the US Army for 24 months as a Korean Augmented To US Army (KATUSA). After the B. S. degree, he worked in Samsung Electronics Corporation from December, 2003 to June, 2008. He began his studies at the University of Tennessee at Knoxville in the fall of 2008. He successfully defended his thesis on July 18, 2013, and will graduate with his Ph.D. in Physics in August 2013.